Scientific
Research
Publishing

Open Journal of Biophysics

BIOPHYSICS

9 772164 538002   01

www.scirp.org/journal/ojbiphy

Journal Editorial Board

Scientific
Research
Publishing

Table of Contents

Volume 9   Number 1   January 2019

Open Journal of Biophysics (OJBIPHY)
Journal Information

SUBSCRIPTIONS

SERVICES

COPYRIGHT

PRODUCTION INFORMATION

Nasal Cycle Dilemma: Nasal Cycle Is Associated to Brain Wake/REM States or Is Associated to Conscious State in Them?

Atanas Todorov Atanasov

Department of Physics and Biophysics, Medical Faculty, Trakia University, Stara Zagora, Bulgaria
Email: atanastod@abv.bg

Abstract

Experimental and theoretical arguments have been described in favor of the hypothesis that the nasal cycle reversals of the nostril's airflow occurs only in the consciousness states of the brain (during awake/wake state, REM state and during dreams in St.1, 2 of the non-REM sleep). This finding gives possibility to use nasal cycle as "marker for consciousness states". An idea for clinical application of the hypothesis is proposed.

1. Introduction

The nasal cycle defines as switch of dominate nostril airflow from left to right side and reverse is well studied during diurnal period of the day over healthy persons in awake (wakefulness) consciousness state [1] [2]. During diurnal time, the periods of the nasal cycle may have duration between 1.0 and 5.0 hours with mean duration during wakefulness about 1.5 hours [3]. The diurnal nasal cycle has random pattern under influence of various psychophysical factors [4] [5] [6]. During the night sleep, the switch of the nostrils occurred nearly in the same interval with periodicity multiplies by one sleep cycle ~1.5 h. In this case, the mean duration of the nasal cycle is about 3 h with dominance of the 3 h nasal cycles (60%), 1.5 h nasal cycles (30%) and 1.5 h nasal cycles (10% from all cases) [7] [8]. The experimental studies of Atanasov *et al.* [7] [8] and Kimura *et al.* [9] have shown the nasal cycle during night sleep is mutually connected to REM stages of the sleep. The experimental results have shown the change of dominate nostril airflow occurs during one of the stages of REM sleep and never not happening

during slow-wave sleep. The principal situation of the nasal cycle reversals (NCR) during diurnal and night (sleep) time is shown in **Figure 1**.

The modern concept for wakefulness (awake/wake) and REM stage of the sleep is both to be considered as consciousness states [11] (see **Figure 2**). The consciousness is ambiguous concept, which is focused on multi-disciplinant debates concerning the cells sensation [12] and the animals psych functions [13]. However, up to now, there is no universal definition for consciousness covering all its essential characters.

Recently, the awake/wake consciousness regard as "primary consciousness state", wireless the REM stage of the sleep regard as "secondary consciousness state" or "proto-consciousness" state [11] [14]. The clinically defined consciousness is characterized by two main components-awareness and arousal [15].

The presence of one or both of these consciousness components gives reason to believe that the given person is in a consciousness or is near to consciousness state. During diurnal period of the day the healthy person normally is in waking consciousness. In this state of consciousness, the sensation and perception are
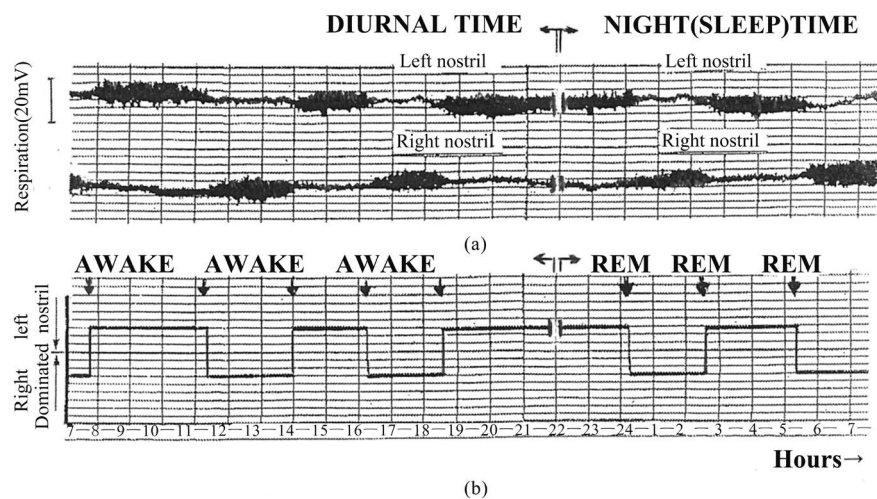
Figure 1. Principal scheme of the nasal cycle reversal during wakefulness and REM stages of the sleep (unpublished data by Atanasov [7] [10]). (a) Record of the breathing streams through the left and right nostrils during diurnal (wakefulness) time and night (sleep) time. (b) Nasal cycle periodicity (arrows shows the moments of the nasal cycle reversals).

Figure 2. The principal scheme of consciousness states of the brain. Legend: awake and REM consciousness refers to daytime and to sleep (dream) time, respectively. Sleep stages 1 and 2, which are neighboring to awake and REM stages are taken as consciousness states during dream.

vivid and externally generated. The thought is logical and progressive. The movement is continuous and voluntary. The characteristics of consciousness during night sleep are poorly studied. The sleep is divided to non-REM and REM stages, which alternate in a certain sequence forming about 1.5 hours periods [16]. It is established that in REM "proto-consciousness" stage of the sleep there is reason to consider that there is "minimum threshold" of consciousness [11] [14]. In "REM proto-consciousness" the sensation and perceptions are vivid and internally generated, and the thought is illogical and bizarre. The movement is command but inhibited. Whatever, just in REM stages of the sleep, it becomes about 84% NCR between the nostrils [7] [8] [9]. During the non-REM stages of the sleep the sensation and perception are absent. If the sleeper is awakened from REM sleep, dream recall rates are very high, between 80 and 90 percent of the awakenings yield some kind of dream report [17]. Even after non-REM awakenings (in stage 2), some mental content has been reported quite often [18]. Some researchers [17] [18] advocate the hypothesis that the mind never sleeps, that is, dreaming of some kind is present during the entire sleep process.

According to other authors [19], sleep that contains dream is considered as conscious state, while dreamless sleep is unconscious. Lucid dreams are reported far more often in REM sleep too [19] [20] [21]. In fact, the lucid dreams could be considered a hybrid state combining essential elements of REM sleep and waking consciousness. Therefore, dreams are the event that defines the consciousness. The studies of Foulkes [22] and others researches [23] [24] [25] showed that dream-like mentation may occur during non-REM stage of sleep and more precisely in the neighborhood of the awake state St.1 and St.2 of sleep [25]. "Light sleepers" can experience dreaming during stage 2 non-REM sleep, whereas "deep sleepers", upon awakening in the same stage, are more likely to report "thinking" but not "dreaming". Despite this wealth of descriptive information about the stages of sleep, the functional purposes of the various sleep states are not known. Whereas most sleep researchers accept the idea that the purpose of non-REM sleep is at least in part restorative, the function of REM sleep remains a matter of considerable controversy. The main difference between REM and non-REM dream is the mental content of activity. However, the dreams in REM and non-REM sleep differ by many characteristics, and mean only 40% of volunteers-sleepers associated dreaming with non-REM sleep [14] [17] [26] in comparison to mean 80% of sleepers associated dreaming with REM sleep [17] [26] [27]. Thus, the non-REM sleep can present some consciousness state in St.1, 2 of the sleep [27]. Figure 3 shows a principal scheme of connection between the consciousness states and NCR in humans.

Recently, there is enough experimental evidence for association between the conscious states and NCR. Indeed, the association between the nasal cycle reversals and awake/wake state and REM stages is well documented [7] [8] [9], while the connection between the NCR and St.1, 2 is under consideration. In the study of Atanasov et al. [7] 75% of the NCR are associated to REM sleep and
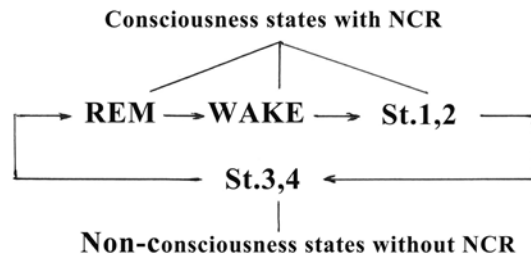
Figure 3. Cycle of the human consciousness. The wake stage is taken to be basic. The newborn to basic wake stages (REM and St.1, 2) are considered as "conscious states".

25% are associated to other body factors. In the study of Kimura *et al.* [9] 68.8% of the NCR tended to be associated with REM sleep and 18.8% tended to be associated to postural change in St.1, 2. The half of these 18.8% NCR are made in "left-right" body position and the other half of NCR are made in "supine" body position. But, it is documented [3] [9] [28] that the "supine" body position does not itself cause nasal cycle reversal, unlike "left" or "right" body position. From these results leads that the NCR can associate not only with postural changes, but also with St.1, 2 of the sleep and "dream-like mentation" in these stages.

On **Figure 3**, the wake state of consciousness is taken to be "basic", but in infants the REM stage appears "basic" state of the brain. In the premature neonates and normal newborns the REM stage can occupy from 50% to 80% of the day and constitutes the main state of the brain. In this case a wake and St.1, 2 are adjacent to the major REM stage. For mature peoples the basic brain stage appears an awake, while the REM stage constitutes about 25% of the sleep [29].

2. Hypothesis

The experiments showed that NCR can observe in awake/wake stage, in St.1, 2 and REM stage of the sleep. Just in these EEG stages certain characteristics of consciousness are retained during wake and dream. Therefore, registration the NCR during awake/wake, St.1, 2 and REM stage can associate to presence of primary and secondary consciousness in these EEG states. **Table 1** gives the connection between the brain EEG stages, mental consciousness states and NCR as a confirmation of the hypothesis. From **Table 1**, it can be seen that the NCR can associate both, with EEG brain stages (wake, REM and 1, 2 stages of sleep) and with conscious states of the brain in these EEG states. Such connection between the EEG stages and corresponding conscious states in them leads to the nasal cycle dilemma. Accordingly to this dilemma the nasal cycle reversals occur only in awake state, REM-dreams and in St.1, 2-dreams of the sleep. If there are no dreams in REM or in St.1, 2 stage of sleep, than there should be no nasal cycle reversals in them.

The transition from awake to sleep can regard as consecutive cycles of progressive awareness and arousal, followed by period of reducing and lack of consciousness and a period of gradually increasing consciousness. On **Figure 4** the transition from awake to St.1, 2 is accompanied by a reduction of consciousness

Table 1. EEG states, mental consciousness states and presence (+) or absence (0) of the NCR

EEG state	Mental state	Presence of NCR
Awake	Normal conscious state	(+)
REM	Dream conscious state	(+)
Stage 1	Non-REM dream (conscious state)	(+)
Stage2	Non-REM dream (conscious state)	(+)
Stage 3	Non-REM (non-conscious state)	(0)
Stage 4	Non-REM (non-conscious state)	(0)
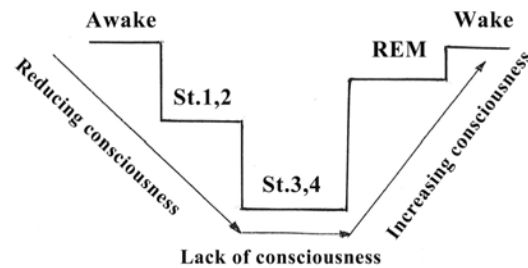
Figure 4. Presentation of "one consciousness cycle". The transition from "awake to St.1, 2 and to St.3, 4" is accompanied of reducing consciousness. The transition from "REM to wake" is accompanied of increasing consciousness.

characteristics. In St.3, 4 it is observed lack of consciousness. In reverse transition from St.3, 4 to REM and to wake states there is a gradual increase of consciousness characteristics.

The "consciousness cycle" presented on Figure 4 repeat some times during night sleep. Whatever, it is possible the similar "daytime conscious cycle" to persist in diurnal time, because the mean duration of the nasal cycle during daytime is about 1.5 hours. This duration correspond to mean length of the sleep cycle [3] [29]. The daytime conscious cycle will only represent a periodic increase and decrease of consciousness characteristics without being present lack of consciousness.

3. Possible Application of the Hypothesis in Clinical Medicine

The evidence that the NCR becomes in consciousness states of the brain gives possibility the NCR to be used as "marker" for consciousness *i.e.* as a peculiar "marker" for consciousness. Exactly, around the moment of NCR the brain is in a conscious state or as close as possible to the conscious state. From the above presentation it can assume that the pattern of nasal cycle can present a new method for detection of consciousness.

Until 2003 year, when REM and NCR association and synchronization was registered for first time by Atanasov *et al.* [7] [8], there was no assumed relationship between the two cycles. So far, the similar is situation in relation to dynamics of the nasal cycle during brain diseases, including disorders of consciousness, coma and related states [30] [31]. The recent methods for detection

of consciousness consist mainly of three groups: neuro-imaging technics, electroencephalography technics and behavior assessment [19] [32]. In addition to these well-established techniques the presence or absence of nasal cycle reversals in patients with brain diseases can be new method for detection of consciousness. One issue of fundamental importance is whether there is a nasal cycle (NCR) in the absence of consciousness, what we have in the states of coma. Another fundamental issue is the relationship between the parameters of the nasal cycle and the tendency of recovering the patients from coma and related states. Figure 5 gives the scheme of cerebral metabolism in norm and coma states and presence or absence of nasal cycle reversals in them.

From Figure 5, it can be seen that cerebral metabolism decreases to 60% from normal consciousness to deep sleep. In coma and related states (minimally consciousness states and vegetative state) the cerebral metabolism is less than 50%. Only in "locked in syndrome" the cerebral metabolism is near to REM stage of sleep. The nasal cycle reversals are detected only in "Normal Conscious State" with 100% cerebral metabolism and in "REM Conscious State" with 90% cerebral metabolism. In "Deep Sleep" with 60% cerebral metabolism there is no nasal cycle reversals. Thus, the presence or absence of nasal cycle reversals during coma and related states will give an opportunity to understand how much nasal cycle reversals is related to the level of cerebral metabolism and consciousness in norm and pathology. If such a link exists, the time for the transition of nasal airflow from left to right nostril and reverse (during NCR) may use patients to be derived from some coma states. As a support of this idea can be quoted the correlation patterns of the brain hemispheric dominance and the nasal cycle dynamics, reported by Werntz *et al.* [33] and Shannahoff-Khalsa [34]. The alternation of the nasal cycle rhythms can present also an index of the diseased [35].
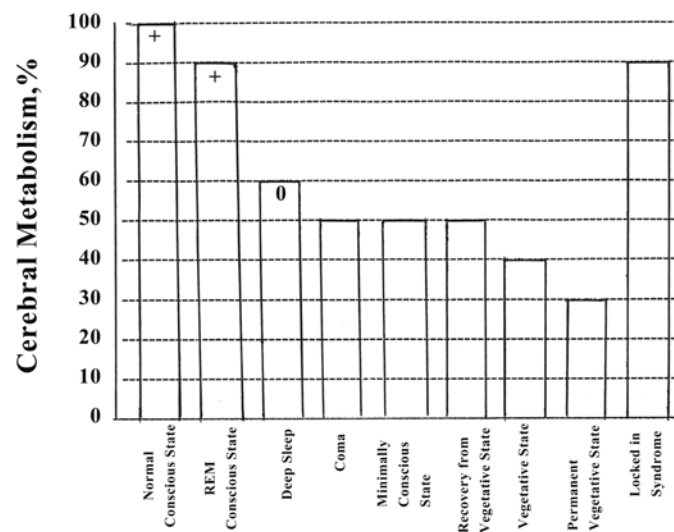
Figure 5. Cerebral metabolism during normal conscious, coma and related states (by Laureys *et al.* [31] modified by Atanasov). *Legend*-with "+" is signed presence of NCR, and with "0" is signed absence of NCR.

4. Conclusion

The novelty in this research consists of some new ideas: Firstly, for possible connection between the NCR and consciousness states of the brain during wakefulness and dreams; Secondly, the possibility NCR to be used as markers for consciousness in some brain diseases. Up to now there is no data for nasal cycle measurement during coma and related states. The possible link between consciousness and the nasal cycle reversals can give a new methodology to awaken people in coma.

Conflicts of Interest

The authors declare no conflicts of interest regarding the publication of this paper.

References

[1] Lenz, H., Theelen, W. and Eichler, J. (1985) Nasal Cycle Using Rhinomanometric Measurements. *HNO*, **33**, 58-61. (In German)

[2] Winkler, M., Combs, A. and Daley, C. (1994) A Chaotic Systems Analysis of the Nasal Cycle. *Behavioral Science*, **39**, 285-292. https://doi.org/10.1002/bs.3830390404

[3] Rohrmeier, Ch., Schittek, S., Ettle, T., Herzog, M. and Kuehnel, T.S. (2014) The Nasal Cycle during Wakefulness and Sleep and Its Relation to Body Position. *The Laryngoscope*, **124**, 1492-1497. https://doi.org/10.1002/lary.24546

[4] Mirza, N., Kroger, H. and Doty, R.L. (1997) Influence of Age on the "Nasal Cycle". *Laryngoscope*, **107**, 62-66. https://www.ncbi.nlm.nih.gov/pubmed/9001267 https://doi.org/10.1097/00005537-199701000-00014

[5] Gilbert, A.N. (1989) Reciprocity versus Rhythmicity in Spontaneous Alternations of Nasal Airflow. *Chronobiology International*, **6**, 251-257. https://www.tandfonline.com/doi/abs/10.3109/07420528909056926 https://doi.org/10.3109/07420528909056926

[6] Kahana-Zweig, R., Geva-sagiv, M., Weissbrod, A., Secundo, L., Soroker, N. and Sobel, N. (2016) Measurring and Characterizing the Human Nasal Cycle. *PLOS ONE*, **11**, e0162918. https://www.ncbi.nlm.nih.gov/pubmed/27711189 https://doi.org/10.1371/journal.pone.0162918

[7] Atanasov, A.T., Dimov, P.D. and Dimitrov, B.D. (2003) Time Periods in the Nasal Cycle during Night Sleep. *Biological Rhythm Research*, **34**, 355-366. https://doi.org/10.1076/brhm.34.4.355.26226

[8] Atanasov, A.T., Dimov, P.D. (2003) Nasal and Sleep Cycle-Possible Synchronization during Night Sleep. *Medical Hypotheses*, **61**, 275-277. https://doi.org/10.1016/S0306-9877(03)00169-5

[9] Kimura, A., Chiba, S., Capasso, R., Yagi, T., Ando, Y., Watanabe, S. and Moriyama, H. (2013) Phase of Nasal Cycle during Sleep Tends to Be Associated with Sleep Stage. *The Laryngoscope*, **123**, 2050-2055. https://www.ncbi.nlm.nih.gov/pubmed/23576311 https://doi.org/10.1002/lary.23986

[10] Atanasov A.T. (2014) Length of Periods in the Nasal Cycle during 24-Hours Registration. *Open Journal of Biophysics*, **4**, 93-96. https://file.scirp.org/pdf/OJBIPHY_2014071716523330.pdf

https://doi.org/10.4236/ojbiphy.2014.43010

[11] Hobson, J.A. and Friston, K.J. (2012) Waking and Dreaming Consciousness: Neurobiological and Functional Considerations. *Progress in Neurobiology*, **98**, 82-98.
https://www.ncbi.nlm.nih.gov/pubmed/22609044
https://doi.org/10.1016/j.pneurobio.2012.05.003

[12] Atanasov, A.T. (2014) Possible Role of Centrioles as Sensor Center in Cells. *Trakia Journal of Sciences*, **12**, 74-78. http://tru.uni-sz.bg/tsj/Vol.%2012%20S1/16.pdf

[13] Hameroff S. and Penrose R. (2014) Consciousness in the Universe: A Review of the "Orch OR" Theory. *Physics of Life Reviews*, **11**, 39-78.
https://www.sciencedirect.com/science/article/pii/S1571064513001188
https://doi.org/10.1016/j.plrev.2013.08.002

[14] Simon, C.W. and Emmons, W.H. (1956) EEG, Consciousness, and Sleep. *Science*, **124**, 1066-1069. https://doi.org/10.1126/science.124.3231.1066

[15] Cologan, V., Schabus, M., Ledoux, D., Moonen, G., Maquet, P. and Laureys, S. (2010) Sleep in Disorders of Consciousness. *Sleep Medicine Reviews*, **14**, 97-105.
https://www.ncbi.nlm.nih.gov/pubmed/19524464
https://doi.org/10.1016/j.smrv.2009.04.003

[16] Fuller, P.M., Gooley, J.J. and Saper, C.B. (2006) Neurobiology of the Sleep-Wake Cycle: Sleep Architecture, Circadian Regulation, and Regulatory Feedback. *JBR*, **21**, 482-493. https://www.ncbi.nlm.nih.gov/pubmed/17107938
https://doi.org/10.1177/0748730406294627

[17] Nielsen, T.A. (2000) A Review of Mentation in REM and NREM Sleep: "Covert" REM Sleep as a Possible Reconciliation of Two Opposing Models. *Behavioral and Brain Sciences*, **23**, 793-1121. https://www.ncbi.nlm.nih.gov/pubmed/11515145
https://doi.org/10.1017/S0140525X0000399X

[18] Foulkes, W.D. (1962) Dream Reports from Different Stages of Sleep. *The Journal of Abnormal and Social Psychology*, **65**, 14-25.
http://psycnet.apa.org/record/1964-03615-001
https://doi.org/10.1037/h0040431

[19] Tononi, G. and Koch, Ch. (2008) Neural Correlates of Consciousness. *Annals of the New York Academy of Sciences*, **1124**, 239-261.
https://www.ncbi.nlm.nih.gov/pubmed/18400934
https://doi.org/10.1196/annals.1440.004

[20] LaBerge, S. (1980) Lucid Dreaming: An Exploratory Study of Consciousness during Sleep. PhD Thesis, Stanford University (University Microfilms No. 80-24), 691.

[21] La Berge, S. (1992) The Neuropsychology of Sleep and Dreaming. In: Antrobus and Bertini, Eds., *Physiological Studies of Lucid Dreaming*, Lawrence Erlbaum Associated, Hillsdate, Hove and London.

[22] Foulkes, D. and Vogel, G. (1956) Mental Activity of Sleep Onset. *Journal of Abnormal Psychology*, **70**, 231-243. https://doi.org/10.1037/h0022217

[23] Rechtschaffen, A., Verdone, P. and Wheaton, J. (1963) Reports of Mental Activity during Sleep. *Canadian Psychiatric Association Journal*, **8**, 409-414.
https://doi.org/10.1177/070674376300800612

[24] Cavallero, C., Cicogna, P., Natale, V., Occhionero, M. and Zito, A. (1992) Slow Waves Sleep Dreaming. *Sleep*, **15**, 562-566. https://doi.org/10.1093/sleep/15.6.562

[25] Oudiette, D., Dealberto, M.-J., Uguccioni, G., Goldman, J.L., Merino-Andreu, M., Tafti, M., Garma, L., Schwartz, S. and Arnulf, S.I. (2012) Dreaming without REM Sleep. *Consciousness and Cognition*, **21**, 1129-1140.

https://medweb4.unige.ch/labnic/papers/Oudiette-et-al_Sleep2012.pdf
https://doi.org/10.1016/j.concog.2012.04.010

[26] Pace-Schott, E.F. and Hobson, J.A. (1988) The Neuropsychology of Dreams: A Clinic-Anatomical Study. *Trends in Cognitive Sciences*, **2**, 199-200.
https://www.ncbi.nlm.nih.gov/pubmed/21227155
https://doi.org/10.1016/S1364-6613(98)01166-8

[27] Solms, M. (2000) Dreaming and REM Sleep Are Controlled by Different Brain Mechanisms. *Behavioral and Brain Sciences*, **23**, 793-1121.
https://pdfs.semanticscholar.org/1146/7e7414c35094ea2262dc659da26bd6b1b11f.pdf
https://doi.org/10.1017/S0140525X00003988

[28] Riechelmann, H. and Krause, W. (1994) Autonomic Regulation of Nasal Vessels during Changes in Body Position. *European Archives of Oto-Rhino-Laryngology*, **251**, 210-213. https://link.springer.com/article/10.1007/BF00628425
https://doi.org/10.1007/BF00628425

[29] Ganong, W.F. (1995) Review of Medical Physiology. Seventeenth Edition, Prentice Hall, Upper Saddle River.

[30] Di Perri, C., Annen, J., Antonopoulos, G., Amico, E., Cavaliere, C. and Laureys, S. (2016) Measuring Consciousness through Imaging. In: *Brain Function and Responsiveness in Disorders of Consciousness*, Springer, Berlin, 51-65.

[31] Laureys, S., Owen, A.M. and Schiff, N.D. (2004) Brain Function in Brain Death, Coma, Vegetative State, Minimally Conscious State and Locked-In Syndrome. *The Lancet Neurology*, **3**, 537-546. https://doi.org/10.1016/S1474-4422(04)00852-X
http://www.coma.ulg.ac.be/papers/vs/PVS_MCS_LIS_LancetN04.pdf

[32] Seth, A.K., Dienes, Z., Cleeremans, A., Overgaard, M. and Pessoa, L. (2008) Measuring Consciousness: Related Behavior and Neurophysiological Approaches. *TiCS*, **30**, 1-8. https://www.ncbi.nlm.nih.gov/pubmed/18606562

[33] Werntz, D.A., Bickford, R.J., Bloom, F.E. and Shannahoff-Khalsa, D.S. (1983) Alternating Cerebral Hemispheric Activity and Lateralization of Autonomic Nervous Function. *Human Neurobiology*, **2**, 39-43.
https://www.ncbi.nlm.nih.gov/pubmed/6874437

[34] Shannahoff-Khalsa, D.S. (1993) The Ultradian Rhythm of Alternating Cerebral Hemispheric Activity. *International Journal of Neuroscience*, **70**, 285-298.
https://www.ncbi.nlm.nih.gov/pubmed/8063547
https://doi.org/10.3109/00207459309000583

[35] Kumaran, E.M. (2018). Alternation in Nasal Cycle Rhythm as an Index of the Diseases Condition. IntechOpen.

Role of Self-Loop in Cell-Cycle Network of Budding Yeast

Shu-ichi Kinoshita[1,2], Hiroaki Yamada[3]

[1]Department of Mathematical Engineering, Faculty of Engeneering at Musashino University, Tokyo, Japan
[2]Institute for Advanced Study of Mathematical Sciences (MIMS), Meiji University, Tokyo, Japan
[3]Yamada Physics Research Labolatory (YPRL), Niigata, Japan
Email: kinop0124@gmail.com, hyamada111@gmail.com

Abstract

Study of network dynamics is very active area in biological and social sciences. However, the relationship between the network structure and the attractors of the dynamics has not been fully understood yet. In this study, we numerically investigated the role of degenerate self-loops on the attractors and its basin size using the budding yeast cell-cycle network model. In the network, all self-loops negatively suppress the node (self-inhibition loops) and the attractors are only fixed points, *i.e.* point attractors. It is found that there is a simple division rule of the state space by removing the self-loops when the attractors consist only of point attractors. The point attractor with largest basin size is robust against the change of the self-inhibition loop. Furthermore, some limit cycles of period 2 appear as new attractor when a self-activation loop is added to the original network. It is also shown that even in that case, the point attractor with largest basin size is robust.

Keywords

Gene Regulatory Network, Attractors, Budding Yeast, Degenerate Self-Loop

1. Introduction

Recently, some networks representing metabolic reactions in the cell and gene regulatory responses through transcription factors have been elucidated along with progress of experimental systems and accumulation technology in the database [1]. In addition, researches on characterizing the state of the cells as a complex network utilizing these databases have been actively investigated [2] [3] [4] [5].

Moreover, the deterministic discrete-time dynamics for discrete-state model

with such network structures have been widely studied on the properties of the attractors that represent cellular activity states. This is because the state space is finite, so it is easy to search the fixed points and the periodic solutions using computer power. For example, Kauffman *et al.* modeled the early cells before differentiation with the dynamics of the network, and made the type of the attractors correspond to the type of cells after the differentiation [6] [7] [8] [9]. On the other hand, Li *et al.* discovered that in the model of the gene regulatory network related to the cell-cycle, there is a fixed point with a very large basin size, and the transition process to the fixed point corresponds to the expression pattern of the gene in each process of the cell-cycle [10]. It should be noticed that in the network of the Kauffman *et al.*, there is no self-regulating factor (self-loop), but in the model of Li *et al.* the existence of the self-loops has influence on the attractors. Very recently, in other systems such as fission yeast cell cycle and mammalian cell cycle, the Boolean network models for the regulation have also been studied [11] [12] [13].

In this study, using the same gene regulatory network as Li *et al.* for the budding yeast, we clarify the relationship between the fixed points (point attractors) with large basin size and the presence of the self-loops in the network. It is found that there is a simple division rule of the state space by removing the self-loops, and the point attractors with largest basin size (BS) is robust against the changing the self-loops. The similar results are obtained for *C. elegans* early embryonic cell cycles as well [14].

2. Model

Here, we give some basic properties of the Boolean network model of the cell-cycle regulation for the budding yeast. Let us take the binary value $\{0,1\}$ as the state S_i of each node i corresponding to the numbered genes as given in Table 1. The states 1 and 0 correspond to expressed and unexpressed genes, respectively and the attractors of the dynamics are associated to cell differentiation. The effect on the node i from the other node $j(\neq i)$ is defined as

$$B_i = \sum_{j(\neq i)}^{N} a_{ij} S_j, \tag{1}$$

where N is the total number of the nodes, and a_{ij} denotes matrix element of the weighted adjacency matrix A representing the interaction between the genes. We take $a_{ij} = +1$ when the node j positively regulates the node i (positive interaction), and $a_{ij} = -1$ when the node j negatively suppresses the node i (negative interaction).

The node without the self-loop, *i.e.* $a_{ii} = 0$, follows a threshold dynamics from discrete time t to $t+1$ ($t \in \mathbf{N}$) by using the parallel updating scheme as follows:

$$S_i(t+1) = \begin{cases} 0 & (B_i(t) < \theta_i) \\ 1 & (B_i(t) > \theta_i) \\ S_i(t) & (B_i(t) = \theta_i) \end{cases} \tag{2}$$

Table 1. Seven attractors in the original gene regulatory network. (All are point attractors.) The third line shows that there is a degenerate self-loop when mark ○ is present in the node. In the decimal notation, each attractor is displayed as, $A_1^{(0)} = 68$, $A_2^{(0)} = 384$, $A_3^{(0)} = 580$, $A_4^{(0)} = 4$, $A_5^{(0)} = 0$, $A_6^{(0)} = 516$, $A_7^{(0)} = 64$. The last column (BS) represents the basin size of the attractors. Note that Cln 1 represents Cln 1, 2, Clb 5 represents Clb 5, 6, and Clb 1 represents Clb 1, 2.

	Cln3	MBF	SBF	Cln1	Cdh1	Swi5	Cdc20	Clb5	Sic1	Clb1	Mcm1	
No.	1	2	3	4	5	6	7	8	9	10	11	BS
	○			○		○	○				○	
$A_1^{(0)}$	0	0	0	0	1	0	0	0	1	0	0	1764
$A_2^{(0)}$	0	0	1	1	0	0	0	0	0	0	0	151
$A_3^{(0)}$	0	1	0	0	1	0	0	0	1	0	0	109
$A_4^{(0)}$	0	0	0	0	0	0	0	0	1	0	0	9
$A_5^{(0)}$	0	0	0	0	0	0	0	0	0	0	0	7
$A_6^{(0)}$	0	1	0	0	0	0	0	0	1	0	0	7
$A_7^{(0)}$	0	0	0	0	1	0	0	0	0	0	0	1

where θ_i denotes the threshold value of the node i. Also, if the self-loop acts inactively when $B_i(t) = \theta_i$, the effect of the protein degradation called "degeneration", which is distinguished from a simple inhibition effect, is given as follows;

$$S_i(t+1) = \begin{cases} 0 & (B_i(t) = \theta_i, a_{ii} = -1) \\ 1 & (B_i(t) = \theta_i, a_{ii} = +1) \end{cases} \tag{3}$$

The budding yeast cell-cycle network model (denoted by $G^{(0)}$) by Li *et al.* is a special one in a sense that all nodes of the existing self-loops are given as $a_{ii} = -1$. The network is shown in **Figure 1**. We take the values $\theta_i = 0$ for all i in this report. Each regulatory factor is represented by each numbered node ($i = 1, 2, \cdots, 11$), and the activation effect ($a_{ij} = +1$) and suppression effect ($a_{ij} = -1$) are indicated by solid and dashed arrows between the nodes. There are self-degeneration loops on the 5 nodes, Cln3, Cln1-2, Swi5, Cbe/Cdc14, Mcm1/SFF. Note that this rule is the same as that of Refs. [5] and [10], but it differs from that of [15]. In this network, the total state number is $W = 2^{11} = 2048$, and all steady states are seven point attractors by numbering as

$$\mathbf{A}^{(0)} = \left\{ A_1^{(0)}, A_2^{(0)}, A_3^{(0)}, A_4^{(0)}, A_5^{(0)}, A_6^{(0)}, A_7^{(0)} \right\}.$$

The state of the point attractor with the largest basin size among these is $A_1^{(0)} = 00001000100 = 68$, where the last number is in decimal. According to the study of Li *et al.* the following facts are known. 1) The attractor with the largest basin $A_1^{(0)} = 68$ corresponds to the stationary G_1 state in the cell-cycle of the budding yeast. 2) When creating the random network model of the same system size $N = 11$, there is no attractor that corresponds to $A_1^{(0)}$ with a very large
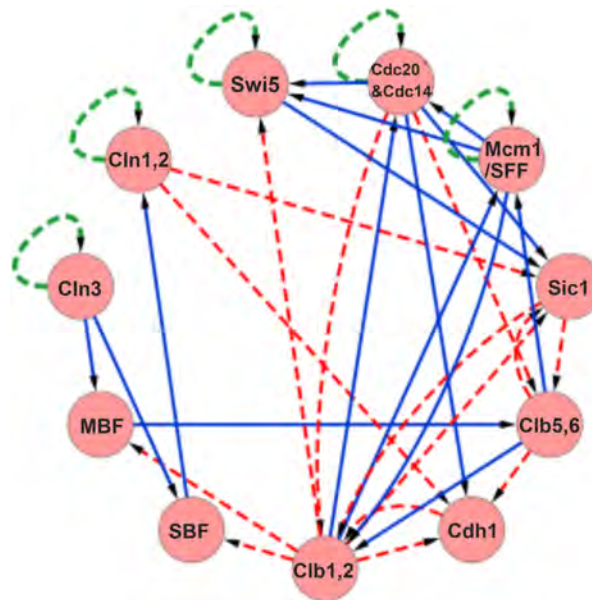
Figure 1. (Color online) Gene regulatory network of the cell-cycle of budding yeast [10]. Each circle represents a protein (cyclin or transcription factor) involved in the gene regulation. For the links connecting the respective proteins, the blue-solid lines represent the effect of the activation control, and the red-dashed lines represent the effect of the suppression control. In addition, the self-loops by green-dotted lines represent the effect (ubiquitin-proteasome system) of protein degradation in the absence of external input.

basin size. 3) One of the trajectories to reach the attractor $A_1^{(0)}$ coincides with the trajectory of the actual biological cell-cycle. 4) The trajectory corresponding to the biological cell-cycle leading to $A_1^{(0)}$ is stable against external perturbation.

In addition, the result for the basin size of the attractors in the similar random networks with same conditions of the structure as the $G^{(0)}$ is given in **Appendix A**. We confirmed that the occurrence probability of the point attractors with the large basin size ($\geq$1700) is less than 20 percent. This result is consistent with those in Ref. [4].

These results may be due to all self-loops being degenerate and threshold values being zero, and all the attractors are point attractors only. Generally, the threshold values are related to adding the active self-loops at each node. Note that for fission yeast cell-cycle model with similar network structure some limit cycles of period two appear as the attractor because some of the threshold value are not zero [15] [16]. Further, notice that when an active self-loop is attached to the node the state update rule becomes different from those of Tran *et al.* due to the existence of rule (3).

3. Numerical Result

In this section, we investigate the effect of the degenerate self-loops on the attractors of the original network $G^{(0)}$. Therefore, we write the network from which the degenerate self-loop of the kth node is removed from $G^{(0)}$ as $G^{(-k)}$, and the network with self-activating loop is added to the mth node of $G^{(0)}$ as

$G^{(+m)}$. Here, k selects from the nodes with the self-loop, and m selects from the nodes without the self-loop. The attractor sets are indicated as

$$\mathbf{A}^{(-k)} = \left\{ A_1^{(-k)}, A_2^{(-k)}, \cdots, A_{n_{-k}}^{(-k)} \right\}, \quad \mathbf{A}^{(+m)} = \left\{ A_1^{(+m)}, A_2^{(+m)}, \cdots, A_{n_{+m}}^{(+m)} \right\},$$

and so on, respectively, where n_{-k} and n_{+m} means the number of attractors in the networks $G^{(-k)}$ and $G^{(+m)}$, respectively. We can numerically decide the all attractors and the basin size because the network has a state space of $2^{11} = 2048$ states.

3.1. Case of Removing Degenerate Self-Loop

In Figure 1 of the original network, degenerate self-loops are included in five control factors of Cln3, Cln1-2, Swi5, Cbc20/Cdc14, Mcm1/SFF, and Table 1 shows the 7 attractors. We show in Table 2 the 11 attractors of the gene regulatory network $G^{(-1)}$ which removed the degenerate self-loop of Cln3 (the first node).

We compare the attractors of the network $G^{(-1)}$ with those of $G^{(0)}$. It is found that $A_2^{(-1)} = A_1^{(0)}$, $A_3^{(-1)} = A_2^{(0)}$, $A_5^{(-1)} = A_3^{(0)}$, $A_8^{(-1)} = A_4^{(0)}$, $A_9^{(-1)} = A_5^{(0)}$, $A_{10}^{(-1)} = A_6^{(0)}$, $A_{11}^{(-1)} = A_7^{(0)}$. That is, all of the attractor sets $\mathbf{A}^{(0)}$ of the original network $G^{(0)}$ is included the attractor set of $\mathbf{A}^{(-1)}$ of the network $G^{(-1)}$.

Next, we focus on the change of the basin size. It follows that the basin size of the attractor $A_1^{(0)}$ with the largest basin size is reduced by the elimination of the degenerate self-loop. Also, the basin size of the other attractors are also reduced from those of $\mathbf{A}^{(0)}$. Figure 2 shows the basin structure of the 2048 initial states

Table 2. Eleven attractors in the gene regulatory network $G^{(-1)}$ which removed the degenerate self-loop of Cln3 (the first node). (All are point attractors.) The last column (BS) represents the basin size of the attractors. In the decimal notation, each attractor is displayed as, $A_1^{(-1)} = 1979$, $A_2^{(-1)} = 68$, $A_3^{(-1)} = 384$, $A_4^{(-1)} = 1459$, $A_5^{(-1)} = 580$, $A_6^{(-1)} = 1595$, $A_7^{(-1)} = 1971$, $A_8^{(-1)} = 4$, $A_9^{(-1)} = 0$, $A_{10}^{(-1)} = 516$, $A_{11}^{(-1)} = 64$.

No.	1	2	3	4	5	6	7	8	9	10	11	BS
				○		○	○				○	
$A_1^{(-1)}$	1	1	1	1	0	1	1	1	0	1	1	888
$A_2^{(-1)}$	0	0	0	0	1	0	0	0	1	0	0	856
$A_3^{(-1)}$	0	0	1	1	0	0	0	0	0	0	0	87
$A_4^{(-1)}$	1	0	1	1	0	1	1	0	0	1	1	61
$A_5^{(-1)}$	0	1	0	0	1	0	0	0	1	0	0	57
$A_6^{(-1)}$	1	1	0	0	0	1	1	1	0	1	1	52
$A_7^{(-1)}$	1	1	1	1	0	1	1	0	0	1	1	23
$A_8^{(-1)}$	0	0	0	0	0	0	0	0	1	0	0	9
$A_9^{(-1)}$	0	0	0	0	0	0	0	0	0	0	0	7
$A_{10}^{(-1)}$	0	1	0	0	0	0	0	0	1	0	0	7
$A_{11}^{(-1)}$	0	0	0	0	1	0	0	0	0	0	0	1
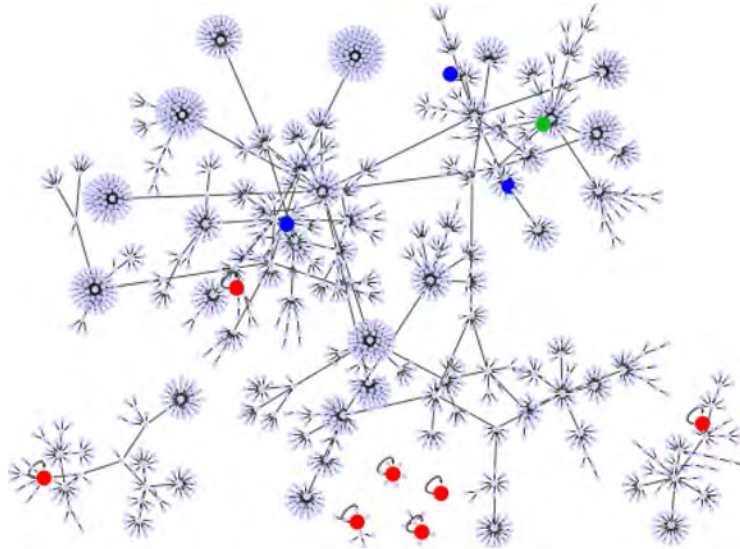
Figure 2. (Color online) The point attractors and the basin structures of the network $G^{(-1)}$. The 7 red circles present the common point attractors to $G^{(0)}$ and $G^{(-1)}$. The blue and green circles present attractors newly added by the network becoming $G^{(-1)}$. The poin attractor with the largest basin of $G^{(-1)}$ is indicated by green circle.

flowing to the fixed points given in Table 2. The red circles are the point attractors of $G^{(0)}$, and the blue circles indicate the four point attractors newly added by the network becoming $G^{(-1)}$. Obviously, the basin size of the same attractor of $G^{(-1)}$ to those of attractor of $G^{(0)}$ is smaller than those of $G^{(0)}$, and they are caused by branching from the basin of $G^{(0)}$. Accordingly, it is also easy to understand that all attractors (attractor sets) of the original network $G^{(0)}$ are included in the attractor set of $G^{(-1)}$. The attractor of the large BS of $G^{(0)}$ corresponds to the attractor of the relatively large BS of $G^{(-1)}$.

In Figure 3, we show the coloring basin structure of $G^{(0)}$ depending on each basin of the attractors of $G^{(-1)}$. (Figure 4 shows the one that removed the color-coded state other than red from the attractor of the largest basin.) It is found that the newly appearing attractors of $G^{(-1)}$ are created by connecting the the leaf states to the other leaf states in the original gene state in the transition diagram.

Although above results are for the specific case which the degenerate self-loop of Cln3 has been removed, but also it is found that the similar results are also true for the cases removing the other degenerate self-loops. Furthermore, if we apply this rule repeatedly in the process of removing the self-loops, we can see that in general the above relations of the attractors and the basin size also applies to the relationship before and after removing the self-loops.

3.2. Case of Adding Active Self-Loop

It is noting that in the general network which both the self-regression loops and self-activation loops exist, limit cycles can appear as the attractors, as shown in case of the fission yeast. In networks which the self-activation loop is added to

Figure 3. (Color online) The basin structure of $G^{(0)}$ classified by colors depending on the basins for each attractor of $G^{(-1)}$. The states are color-coded so that we can see basins of the 11 attractors of $G^{(-1)}$.
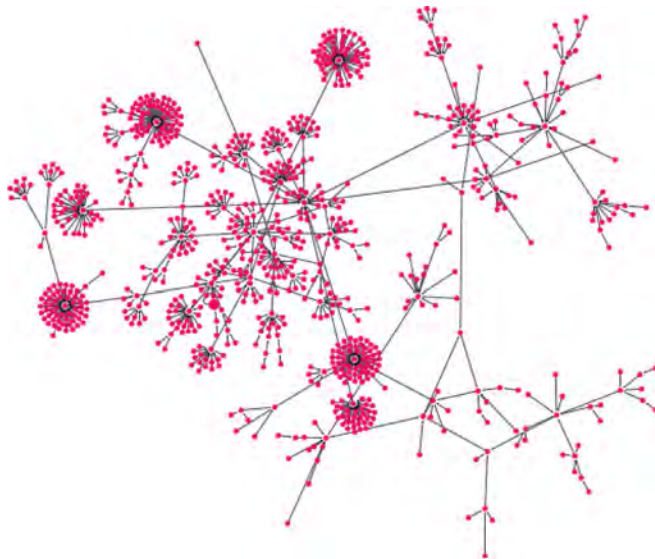
Figure 4. The basin structure that removed the color-coded states other than red in **Figure 3** from the attractor with the largest basin of $G^{(0)}$.

the original network $G^{(0)}$, not only point attractors but also other types of periodic attractors exist.

As an example, the attractors $\mathbf{A}^{(+8)}$ of the network $G^{(+8)}$ which an active self-loop added to Clb5 (the 8th node) of the $G^{(0)}$ is given in **Table 3**. It follows that the attractors $A_1^{(+8)} = A_1^{(0)}$, $A_5^{(+8)} = A_4^{(0)}$, exist also in the network $G^{(0)}$, and the limit cycle attractors of period 2, $A_2^{(+8)}$, $A_3^{(+8)}$, $A_4^{(+8)}$, are newly emerging as the attractors of the network $G^{(+8)}$. Also, it follows that many attractors of $G^{(0)}$ have disappeared, but the attractor with largest basin size has survived. The basin structure of the attractors in the **Table 3** is shown in **Figure 5**. It is found

Table 3. Five attractors present in gene regulatory network $G^{(+8)}$ which an active self-loop is added to Clb5 (the 8th node). The three attractors $A_2^{(+8)}$, $A_3^{(+8)}$, $A_4^{(+8)}$ are limit cycle. LC_{P_2} means the limit cycle with the period 2. The last column (BS) represents the basin size of the attractors. In the decimal notation, each attractor is displayed as, $A_1^{(+8)} = 59$, $A_2^{(+8)} = (933,956)$, $A_3^{(+8)} = (613,633)$, $A_4^{(+8)} = (549,572)$, $A_5^{(+8)} = 4$.

No.	1	2	3	4	5	6	7	8	9	10	11	BS
	○			○		○	○	+			○	
$A_1^{(+8)}$	0	0	0	0	1	0	0	0	1	0	0	1897
$A_2^{(+8)} (LC_{P2})$	0	1	1	1	0	1	0	0	1	0	1	110
	0	1	1	1	0	1	1	1	1	0	0	
$A_3^{(+8)} (LC_{P2})$	0	1	0	0	1	1	0	0	1	0	1	25
	0	1	0	0	1	1	1	1	1	0	0	
$A_4^{(+8)} (LC_{P2})$	0	1	0	0	0	1	0	0	1	0	1	9
	0	1	0	0	0	1	1	1	1	0	0	
$A_5^{(+8)}$	0	0	0	0	0	0	0	0	1	0	0	7
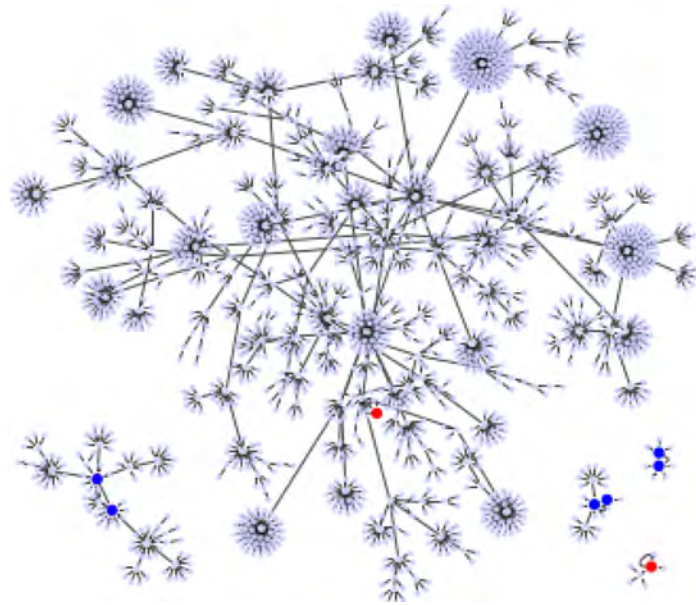
Figure 5. The attractors and the basin structures of $G^{(+8)}$. The 2 red circles present the point attractors. The 6 blue circles represent the states that belong to the three limit cycles of period 2 two each, respectively.

that the limit cycles are constituted by combining the gene states with the relatively small basin size. In such a case the limit cycles with large basin size do not occur.

These features occur even if the self-activated loop is added to the other nodes without the self-loop. Furthermore, the similar phenomena can also be confirmed by changing any of the degenerate self-loop of the five nodes to the active one.

4. Summary and Discussion

In this short report, we investigated the influence of the degenerate self-loop on attractor of the gene regulatory network model of the cell-cycle of budding yeast.

In the case of networks with degenerate self-loops removed from the original network $G^{(0)}$, only the point attractor appears because all of the self-loops are degenerate. The attractor set of the network without the degenerate self-loops includes all attractors of the original network $G^{(0)}$. In addition, when self-regression loops and self-activation loops coexist, limit cycles with the period more than 2 appear other than point attractor, and many attractors of $G^{(0)}$ are not included in the attractor set, but the attractor with the largest basin size was relatively stable against the deletions and additions of the self-loop. Above result can apply to Boolean genetic network model of *C. elegans* early embryonic cell-cycle network as it is, because the self-loops of network are only self-inhibition loops, and the attractors are only fixed points [4] [14].

Note that necessary and sufficient condition that the network attractors does not become limit cycle but only point attractors is not known yet [5] [15] [17]. However, we expect that the result in Subsec. 3.1 holds when at least the attractors are only fixed points in the random network with only degenerate self-loops.

There is a theorem in the graph theory [15]: *Consider a Boolean network such that each gene is governed with a threshold function. Then, if the associated incidence graph, without considering the diagonal elements, is a directed acyclic graph* (*DAG*) *and the thresholds are non negative,* $\theta_i \geq 0$ *, then the attractors are only fixed points.* The network of the budding yeast satisfies the following sufficient condition for the fixed points. The result of the Subsec. 3.2 seems to contradict above theorem at first glance. However, considering that the update rule (3) is different from one in Ref. [15], we can see that it is not necessarily contradictory to the theorem.

Acknowledgements

Conflicts of Interest

The authors declare that they have no competing interests.

References

[1] Salgado, H., *et al.* (2003) RegulonDB v8.0: Omics Data Sets, Evolutionary Conservation, Regulatory Phrases, Cross-Validated Gold Standards and More. *Nucleic Acids Research*, **41**, D203-D213.

[2] Han, B. and Wang, J. (2007) Quantifying Robustness and Dissipation Cost of Yeast Cell Cycle Network: The Funneled Energy Landscape Perspectives. *Biophysical Journal*, **92**, 3755-3763. https://doi.org/10.1529/biophysj.106.094821

[3] Ferhat, A., *et al.* (2009) Scalable Steady State Analysis of Boolean Biological Regula-

tory Networks. *PLoS ONE*, **12**, e7992.

[4] Huang, X., *et al.* (2013) Boolean Genetic Network Model for the Control of *C. elegans* Early Embryonic Cell Cycles. *BioMedical Engineering OnLine*, **12**, S1. https://doi.org/10.1186/1475-925X-12-S1-S1

[5] Tran, V., *et al.* (2013) On the Underlying Assumptions of Threshold Boolean Networks as a Model for Genetic Regulatory Network Behavior Frontiers in Genetics. *Bioinformatics and Computational Biology*, **4**, Article 263.

[6] Kauffman, S.A. (1969) Metabolic Stability and Epigenesis in Randomly Constructed Genetic Nets. *Journal of Theoretical Biology*, **22**, 437-467. https://doi.org/10.1016/0022-5193(69)90015-0

[7] Iguchi, K., Kinoshita, S. and Yamada, H.S. (2007) Boolean Dynamics of Kauffman Model with a Scale-Free Network. *Journal of Theoretical Biology*, **247**, 138-151. https://doi.org/10.1016/j.jtbi.2007.02.010

[8] Kinoshita, S., Iguchi, K. and Yamada, H.S. (2009) Intrinsic Properties of Boolean Dynamics in Complex Networks. *Journal of Theoretical Biology*, **256**, 351-369. https://doi.org/10.1016/j.jtbi.2008.10.014

[9] Daniels, B.C., *et al.* (2018) Criticality Distinguishes the Ensemble of Biological Regulatory Networks. *Physical Review Letters*, **121**, 138102. https://doi.org/10.1103/PhysRevLett.121.138102

[10] Li, F., Long, T., Lu, Y., Ouyang, Q. and Tang, C. (2004) The Yeast Cell-Cycle Network Is Robustly Designed. *Proceedings of the National Academy of Sciences of the United States of America*, **101**, 4781-4786. https://doi.org/10.1073/pnas.0305937101

[11] Yang, L.J., *et al.* (2013) Robustness and Backbone Motif of a Cancer Network Regulated by miR-17-92 Cluster during the G1/S Transition. *PLoS ONE*, **8**, 1-9. https://doi.org/10.1371/journal.pone.0057009

[12] Barberis, M., Todd, R.G. and van der Zee, L. (2016) Advances and Challenges in Logical Modeling of Cell Cycle Regulation: Perspective for Multi-Scale, Integrative Yeast Cell Models. *FEMS Yeast Research*, **17**, fow103.

[13] Luo, X., Xu, L., Han, B. and Wang, J. (2017) Funneled Potential and Flux Landscapes Dictate the Stabilities of Both the States and the Flow: Fission Yeast Cell Cycle. *PLOS Computational Biology*, **13**, e1005710. https://doi.org/10.1371/journal.pcbi.1005710

[14] Kinoshita, S. and Yamada, H. (2018) The Effect of Removal of Self-Loop for Attractor on Cell Cycle Network. In: Morales, A.J., *et al.*, Eds., *Unifying Themes in Complex Systems IX: Proceedings of the Ninth International Conference on Complex Systems*, Springer Proceedings in Complexity, Springer Nature Switzerland AG, 346-351.

[15] Goles, E., Montalva, M. and Ruz, G.A. (2013) Deconstruction and Dynamical Robustness of Regulatory Networks: Application to the Yeast Cell Cycle Networks. *Bulletin of Mathematical Biology*, **75**, 939-966. https://doi.org/10.1007/s11538-012-9794-1

[16] Davidich, M.I. and Bornholdt, S. (2008) Boolean Network Model Predicts Cell Cycle Sequence of Fission Yeast. *PLoS ONE*, **3**, e1672. https://doi.org/10.1371/journal.pone.0001672

[17] Richard, A. (2015) Fixed Point Theorems for Boolean Networks Expressed in Terms of Forbidden Subnetworks. *Theoretical Computer Science*, **583**, 1-26. https://doi.org/10.1016/j.tcs.2015.03.038

Appendix A: Case of the Random Network Models

We randomly construct the cell-cycle network with the same number of nodes and links as the budding yeast, and examined the attractors and its basin size x by re-linking in the network. The number of nodes is 11, the number of active links is 14, number of suppressing links is 15, and (suppressing) self loop number is 5. For each sample, attractors with the largest basin size were examined. In the cases, all are point attractors because the networks satisfy the sufficient condition. Figure 6 shows the probability distribution $Pr(x_{BS} \leq x)$ of the random network that the largest basin size x_{LBS} is smaller than x. It follows that about 20 percent even on a random network maintaining the same structure as the budding yeast have attractor with the similar or the larger basin size (≥ 1700) than the budding yeast. The result is similar with those for ES cell network of C. elegans in Ref. [4].
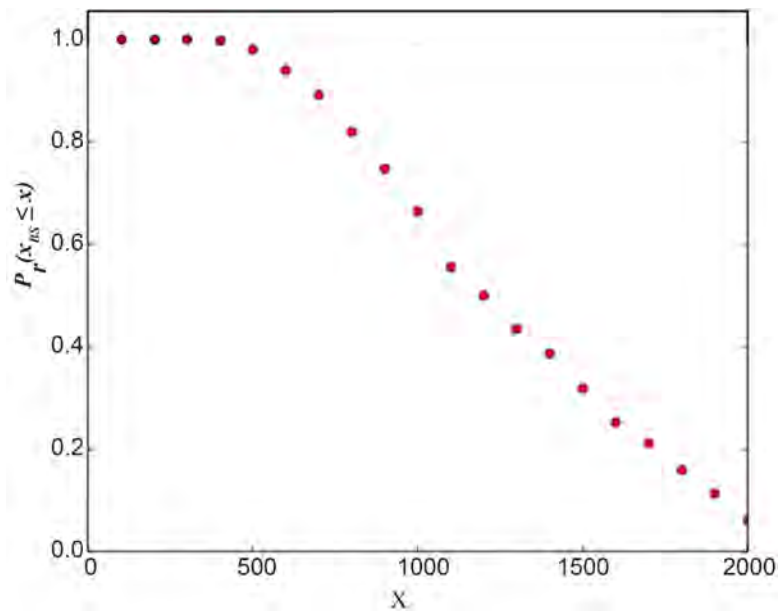
Figure 6. The probability distribution $Pr(x_{BS} \leq x)$ of the random network that the largest basin size x_{BS} is smaller than x. We used 1000 network samples that the number of nodes is 11, the number of active links is 14, number of suppressing links is 15, and (suppressing) self-loop number is 5.

Effective-Spring Model of Tympanic Response in Archosaurs

David T. Heider, J. Leo van Hemmen

Physik Department T35 and Department of Mathematics, Technische Universität München, München, Germany
Email: david.heider@tum.de, lvh@tum.de

Abstract

Whereas for smaller animals the eardrums are well-characterized as excitable membranes or drums, some animals such as several archosaurs feature, as a first approximation, a rather stiff elastic shell supported by an elastic ring. Mathematically, the theory of plates and shells is applicable but its governing equations overly complicate the modeling. Here the notion of tympanic structure is introduced as a generalization of "ordinary" tympanic membranes so as to account for sound perception as it occurs in archosaurs, such as birds and crocodilians. A mathematical model for the tympanic structure in many archosaurs called two-spring model implements this notion. The model is exactly soluble and solutions are presented in closed form and as a series expansion. Special emphasis is put onto offering an easy-to-apply model for describing experiments and performing numerical studies. The analytic treatment is supplemented by a discussion of the applicability of the two-spring model in auditory research. An elasticity-theoretic perspective of the two-spring model is given in the Appendix.

Keywords

Two-Piece Eardrum, Eardrum Vibrations, Shell, Elasticity, Archosaurs

1. Introduction

1.1. Internally Coupled ears (ICE)

More than half of the land-living vertebrates possess an air-filled cavity connecting left and right eardrums. That is, they possess internally coupled ears, for short ICE [1]. **Figure 1** shows the evolution of hearing in vertebrates using ICE [2] [3] [4]. In the simplest models [5] [6] of this widespread mechanism the two eardrums are an elastic structure interfacing the external acoustic environment
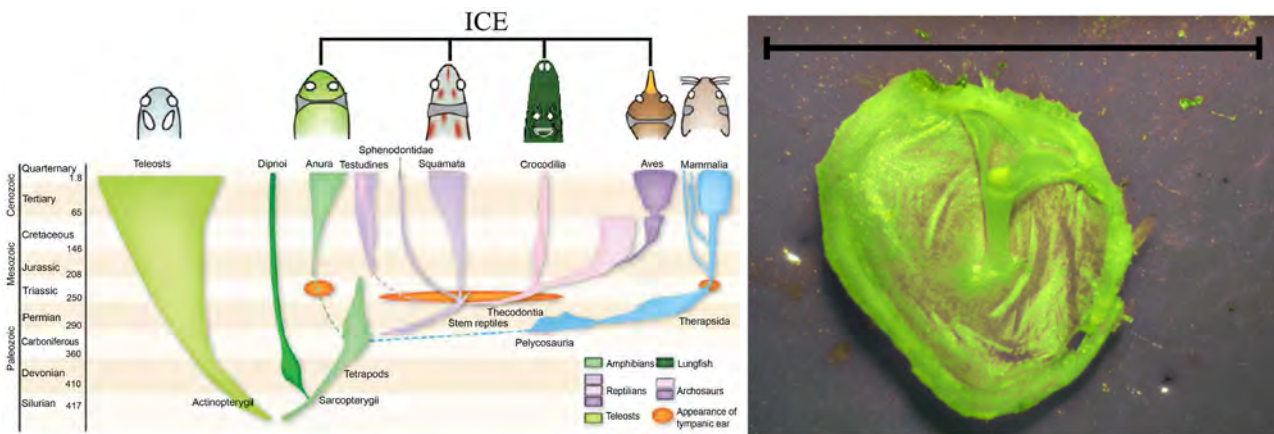
Figure 1. Left: Evolution of vertebrate hearing systems and animals using ICE. Courtesy of Anupam P. Vedurmudi for the full graphic, adapted from van Hemmen *et al.* [1]. Right: The elastic shell of a crocodilian (youngster's) eardrum. The black bar sets a length scale of 1 cm. The diameter and height of the shell structure are 8 mm and 2 mm, respectively. The extracolumellar lever is located in the upper right quadrant of the picture. Its geometry resembles a spherical sector. Picture courtesy of Bruce A. Young.

with the interaural cavity, functioning as an acoustic wave guide [7] [8]. The interaural cavity ensures that the membranes' vibrations are not independent but mutually coupled. For neuronally less developed animals, the coupling provides an easy-to-realize mechanism to generate a more precise directional hearing than without ICE; for early attempts at an explanation, see Autrum [9] [10].

Although the mechanism of internally coupled ears seems *in principio* universal for numerous animals, the biological realization differs from species to species and animal to animal [1]. Aquatic frogs such as *Xenopus* [11] employ plate-like eardrums bounding an air-filled cavity whereas several birds, in particular chicken, use a flexible membrane in a cavity filled with, surprisingly, not air [3]. Lizards [5] [6] [12] use flexible membranes connected by a large cylindrical cavity whereas crickets employ, possibly to comply with their exoskeletal anatomy, a complicated tracheal system featuring two membranes connected through a complicated cavity system. The latter is partitioned itself into two symmetric halves by another elastic structure called septum [13].

An increase in the area covered by the eardrums leads to a lowering of the fundamental frequency in a "clamped membrane model" because the first eigenvalue of the Laplacian (with Dirichlet boundary conditions) scales as the inverse of the square of the area covered by the eardrums. Thus a small eardrum area seems favorable to these animals. Anatomically, these requirements are realized in some archosaurs through a self-supporting spherical shell supported by an elastic ring. In reptiles and birds, an elastic ring occurs far more often [14] in the middle ear than one might naively expect.

The construction is shown schematically in **Figure 2**. The spherical shell itself may vibrate due to bending and is shown *in vitro* in **Figure 1**. Its net displacement in vertical direction leads to an induced vibration of the ring supporting the spherical shell elastically. This means that the notion of a tympanic membrane naturally breaks down because the shell is far less flexible than the elastically
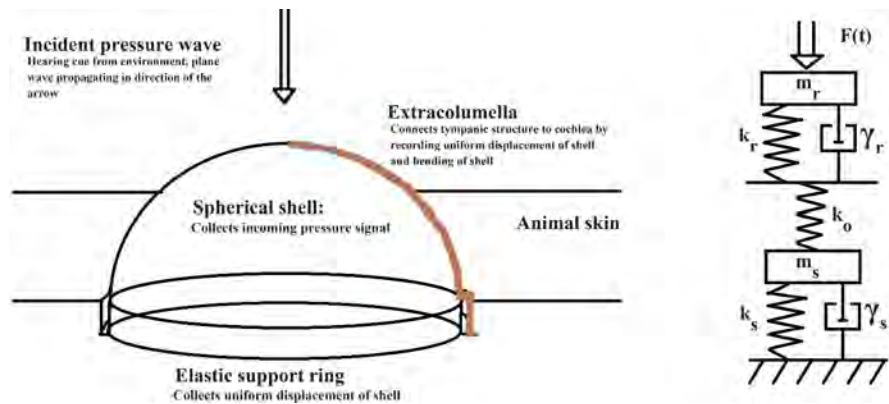
Figure 2. Left: Schematic physical decomposition of the vibration of the tympanic structure due to an incident pressure signal. Right: Conceptual representation of the two-spring model. The pressure signal causes a uniform displacement of the spherical shell or, equivalently, an elastic deformation x_r of the supporting ring underneath. The vibration of the ring leads, once the shell is not a hemisphere, to a an excess torque applied to the boundary of the shell and thus to shell bending, x_s, and has been incorporated through a coupling of the x_r-oscillator to the x_s-oscillator through a massless spring of spring constant k_0.

supporting ring so that the latter is responsible most for the fundamental frequency of the "eardrum". It needs to be constantly borne in mind that the amplitudes are in the nm range whereas the ring has a thickness of mm so that the difference is at least 5 orders of magnitude. Physical auditory research [13] currently lacks both adequate jargon and formalism to capture these phenomena and indicate the direction of useful modeling. This is the gap we aspire to fill with the present treatment.

1.2. Tympanic Structures

A tympanic structure is defined to be the (finite) set of elastic elements that 1) interface the interaural cavity of the animal under consideration with its external acoustic environment, 2) by virtue of mutual elastic coupling of the constituents function as a single elastic structure, and 3) respond in this form at least locally to auditory signals. We call a given tympanic structure N-constituent tympanic structure, if the set of elastic elements in the sense of the previous definition has cardinality N. An elastic element of a tympanic structure is also called a constituent.

2. Two-Spring Model

2.1. Heuristic Derivation of the Two-Spring Model

The two-spring model is based on two simplifying assumptions. First, we are only interested in the impact that the vibration of a tympanic structure has on the volume in the interaural cavity. Vibrations give rise to a local mass density change in the cavity and thus trigger the formation of a pressure wave traveling between the, usually two, tympanic structures [1] [5] [6]. We refer to Howe [8]

[7] for an introductory treatment of sound generated by vibrating elastic structures, to Timoshenko [15] [16] for a detailed treatment of elasticity, and to van Hemmen and Leibold [17] for elasticity theory as applied to biological membranes.

Let (q_1, q_2, q_3) be coordinates such that $q_3 = 0$ and $(q_1, q_2) \in \Gamma$ define the equilibrium position of an elastic element where $\Gamma \subset \mathbb{R}^2$ is bounded and suitably regular domain. (For two eardrums there is, say, another element at $q_3 = L > 0$.) Furthermore, let u be the displacement, $i.e.$, a small $u \ll \sqrt{\mathrm{Area}(\Gamma)}$ perturbation from the former equilibrium. Solving elasticity equations for two-dimensional elastic structures is equivalent to the inversion of operators $\partial_t^2 + \mathrm{O}$ where O typically is the Laplacian Δ, its square Δ^2, the bi-harmonic operator Δ_{bi}^2 or linear combinations thereof [17]. Let us replace the displacement of the constituents of a tympanic structure by its average

$$x(t) \equiv \frac{1}{\mathrm{Area}(\Gamma)} \int_\Gamma \mathrm{d}^2(q_1, q_2) u(t, q_1, q_2). \tag{1}$$

This approximation is called piston approximation [5] [12]. Assuming physical behavior of the full displacement u depending on the temporal variable t as well as the spatial coordinates q_1, q_2, we can apply the mean value theorem of integration. It ensures the existence of a $(q_1', q_2') \in \Gamma$ such that $u(t, q_1', q_2') = x(t)$.

We now perform a partial Taylor series expansion in the spatial variables

$$u(t, q_1, q_2) = x(t) + R(t, q_1, q_2) \tag{2}$$

where $R(t, q_1, q_2)$ is Lagrange's remainder,

$$R(t, q_1, q_2) = \sum_{i=1}^{2} (q_i - q_i') \int_0^1 \mathrm{d}s \, \partial_i u\left(t, \left\{(1-s)q_j' + sq_j\right\}_j\right). \tag{3}$$

The remainder is absolutely bounded from above by firstly applying Cauchy's inequality to the Euclidean inner product. We note that

$$\left\|(q_1 - q_1', q_2 - q_2')\right\|_2 \le \mathrm{diam}(\Gamma) \equiv \sup\left\{\left\|(q_1, q_2) - (q_1', q_2')\right\|_2 : (q_1, q_2), (q_1', q_2') \in \Gamma\right\}$$

and that the function inside the integral is smaller than or equal to its maximum modulus. The remainder is now bounded by

$$\left. |R| \right|_{q_1, q_2}(t) \le \mathrm{diam}(\Gamma) \max_{(q_1, q_2) \in \Gamma} \left\|(\nabla u)\right\|_2(t). \tag{4}$$

In particular, the piston approximation is dynamically accurate, if

$$\max_{(q_1, q_2) \in \Gamma} \left\|(\nabla u)\right\|_2(t) \ll \frac{|x|(t)}{\mathrm{diam}(\Gamma)}. \tag{5}$$

Our first assumption is that the above inequality is fulfilled.

Next we define $\tilde{x}$ and $\omega^2 > 0$ through averaging over $(-\mathrm{O})[u]$,

$$\omega^2 \tilde{x}(t) \equiv \frac{1}{\mathrm{Area}(\Gamma)} \int_\Gamma \mathrm{d}^2(q_1, q_2) (-\mathrm{O})[u](t, q_1, q_2). \tag{6}$$

Since $-\mathrm{O} \ge 0$, $i.e.$, O is positive-definite for all practical purposes, we obtain a square of an effective average frequency and an average displacement $\tilde{x}$ that

may be different from x. By inspection of a formal eigenfunction expansion of u, it is seen that

$$x \approx \tilde{x}, \qquad (7)$$

if dominantly *one* eigenmode is excited in the spatial vibration pattern. The dominant biological mode is the fundamental mode, which is most often the excited vibrational mode of elastic structures relevant to auditory processes. The second assumption is that $x \approx \tilde{x}$ can be utilized as $x = \tilde{x}$. That is, only one mode of the elastic structure is excited dominantly.

Effectively, the partial differential equation that would be needed for a full description of *one* constituent of the tympanic structure can be written in the form of a harmonic oscillator equation,

$$m\ddot{x} + kx = F_{\text{full}}. \qquad (8)$$

To derive the two-spring model we will use the following argument: Since the spherical shell is supported elastically by a ring underneath, we only need to store *local* vibrations of the shell surface in x_s.

The displacement of the shell as a whole along the symmetry axis of the ring is equal to the displacement x_r of the ring. With phenomenological damping coefficients γ_s and γ_r average displacements x_s and x_r in the sense of the piston approximation satisfy damped harmonic oscillator equations with two driving source terms $F_{s,\text{full}}$ and $F_{r,\text{full}}$

$$m_s \ddot{x}_s + 2 m_s \gamma_s \dot{x}_s + k_s x_s = F_{s,\text{full}}\left(t; x_s, x_r\right), \qquad (9)$$

$$m_r \ddot{x}_r + 2 m_r \gamma_r \dot{x}_r + k_r x_r = F_{r,\text{full}}\left(t; x_s, x_r\right). \qquad (10)$$

We now need to specify the driving forces $F_{s,\text{full}}$ and $F_{r,\text{full}}$ in more detail. First, we assume that an external pressure signal p hits the spherical shell homogeneously. Put simple, p transfers a uniform momentum to the shell's surface and thus makes the shell move up and down without deformation of its equilibrium shape. By definition of x_s, x_r, this corresponds to an external force applied to x_r because x_s shall only store *local* shell vibrations but no *global* piston modes. Since the ring itself is elastic, it will vibrate and thus lead to a small bending of the shell [15].

For the elastic interaction between the two constituent elastic structures, we use the Hooke approximation. We regard the constituents as being coupled by a massless, elastic spring with spring constant k_0: $F_{s,\text{full}} = k_0 x_r$ and $F_{r,\text{full}} = F + k_0 x_s$ where k_0 is treated as a fitting parameter. A rough estimate concerning the ratio k_0/k_r can be found in the Appendix. The other parameters $m_s, m_r, \gamma_s, \gamma_r, k_s, k_r$ can be determined from experimental measurements. The above choice of source terms defines the two-spring model. Its underlying physical picture is summarized for the reader's convenience in Figure 2, on the right.

2.2. Two-Spring Model

The deliberations of the previous paragraph are summarized by the governing

equations of our two-spring model,

$$m_s \ddot{x}_s + 2m_s \gamma_s \dot{x}_s + k_s x_s = k_0 x_r, \tag{11}$$

$$m_r \ddot{x}_r + 2m_r \gamma_r \dot{x}_s + k_r x_r = k_0 x_s + F. \tag{12}$$

We assume $k_0 < \min\{k_s, k_0\}$. This means that the coupling through the massless spring does not dominate the spring constants corresponding to eigenmodes of the individual constituents.

Since the tympanic structure is supposed to be at rest in the absence of an incident acoustic pressure signal on the shell, the initial conditions at $t = 0$, *i.e.*, when a signal is about to hit the shell, are fully homogeneous:

$$x_s(t = 0) = 0 = x_r(t = 0) \quad \text{and} \quad \dot{x}_r(t = 0) = 0 = \dot{x}_s(t = 0).$$

Let us denote the surface of the shell by $\Sigma(t)$. An incident pressure wave is described as $p(t, \boldsymbol{x})$ where $\boldsymbol{x}$ are the coordinates in the surrounding space. It becomes a vector quantity when we multiply it by the direction of wave propagation, viz., the normal to the wave front. Then the scalar net force exerted on the shell is given by

$$F(t) = \left(\int_{\Sigma} \left\langle \mathrm{d}\boldsymbol{S}(\Sigma), \boldsymbol{p} \right\rangle_{\mathbb{R}^3} \right)(t). \tag{13}$$

In practice, a time harmonic signal $F(t) \simeq p_0 \Sigma_0 \exp(i\omega t + i\phi)$ proves to give decent results for an incident low-frequency plane-wave-like signal with uniform scalar amplitude p_0 due to a sourced at a position in the acoustic far field. Σ_0 is the area of the equilibrium shape of the shell constituent, ω denotes the frequency carried by the acoustic signal, and ϕ symbolizes where to place an additive phase to account for directional information stored in the signal.

2.3. Solution of the Two-Spring Model

We solve the two-spring model by reduction to a first-order system. Let us define $y_s = \dot{x}_s$ and $y_r = \dot{x}_r$. With $a_r \equiv F/m_r$, the first-order system reads

$$\frac{\mathrm{d}}{\mathrm{d}t} \begin{pmatrix} x_s \\ y_s \\ x_r \\ y_r \end{pmatrix} = \begin{pmatrix} 0 \\ 0 \\ 0 \\ a_r \end{pmatrix} + \boldsymbol{M} \begin{pmatrix} x_s \\ y_s \\ x_r \\ y_r \end{pmatrix} \quad \text{where} \quad \boldsymbol{M} \equiv \begin{pmatrix} 0 & 1 & 0 & 0 \\ -\omega_s^2 & -2\gamma_s & \omega_{d,s}^2 & 0 \\ 0 & 0 & 0 & 1 \\ \omega_{d,r}^2 & 0 & -\omega_r^2 & -2\gamma_r \end{pmatrix}. \tag{14}$$

We have employed the following definitions of squares of reduced frequencies: $\omega_r^2 = k_r/m_r$, $\omega_s^2 = k_s/m_s$ and $\omega_{d,s}^2 = k_0/m_s$ as well as $\omega_{d,r} = k_0/m_r$. The system is linear so that we can invoke the variation-of-constants or Duhamel formula [18]. We denote by $[\boldsymbol{A}]_{kl}$ the (k, l)-entry of a matrix $\boldsymbol{A}$. Conveniently, the initial conditions to be satisfied by x_r, x_s are homogeneous so that the variation of constants method yields

$$x_s(t) = \int_0^t \mathrm{d}\tau \left[\exp\left((t - \tau)\boldsymbol{M}\right) \right]_{14} a_r(\tau), \tag{15}$$

$$x_r(t) = \int_0^t \mathrm{d}\tau \left[\exp\left((t - \tau)\boldsymbol{M}\right) \right]_{34} a_r(\tau) \tag{16}$$

2.4. Solution to the Eigenvalue Problem

The matrix exponential requires the solution of the eigenvalue problem for the matrix M and, in particular, knowledge of the zeros of the characteristic polynomial $\chi_M(\omega) \equiv \det(-i\omega 1_4 + M)$. More precisely, we need the roots of the following quartic equation,

$$
\begin{aligned}
0 = & \left(\omega_r^2 \omega_s^2 - \omega_{d,r}^2 \omega_{d,s}^2\right) + 2i\omega\left(\omega_r^2 \gamma_s + \gamma_r \omega_s^2\right) \\
& + \omega^2\left(-4\gamma_r\gamma_s - \omega_r^2 - \omega_s^2\right) - 2i\omega^3\left(\gamma_r + \gamma_s\right) + \omega^4 \\
\equiv & \; d + c\omega + b\omega^2 + a\omega^3 + \omega^4 .
\end{aligned}
\tag{17}
$$

The above equation can be analytically solved for ω by combining the methods of Cardano and Ferrari [19] [20] for the solution of a generic cubic (Cardano) and quartic (Ferrari) polynomial equations by algebraic completeness of $\mathbb{C}$. By a somewhat lengthy but straightforward calculations we can specify the four, possibly multiple, roots ω_k's for $k \in \{1,2,3,4\}$ in terms of $\omega_s^2, \omega_{d,s}^2, \omega_r^2, \omega_{d,r}^2, \gamma_s, \gamma_r$:

$$
\omega_1 = \left[i(\gamma_s + \gamma_r) - \sqrt{p + 2\Omega^2} + \sqrt{p + 2\Omega^2 + 4\left(\frac{q}{2\sqrt{p + 2\Omega^2}} + p + \Omega^2\right)}\right]\Big/2 , \tag{18}
$$

$$
\omega_2 = \left[i(\gamma_s + \gamma_r) - \sqrt{p + 2\Omega^2} - \sqrt{p + 2\Omega^2 + 4\left(\frac{q}{2\sqrt{p + 2\Omega^2}} + p + \Omega^2\right)}\right]\Big/2 , \tag{19}
$$

$$
\omega_3 = \left[i(\gamma_s + \gamma_r) + \sqrt{p + 2\Omega^2} + \sqrt{p + 2\Omega^2 + 4\left(-\frac{q}{2\sqrt{p + 2\Omega^2}} + p + \Omega^2\right)}\right]\Big/2 , \tag{20}
$$

$$
\omega_4 = \left[i(\gamma_s + \gamma_r) + \sqrt{p + 2\Omega^2} - \sqrt{p + 2\Omega^2 + 4\left(-\frac{q}{2\sqrt{p + 2\Omega^2}} + p + \Omega^2\right)}\right]\Big/2 \tag{21}
$$

$$
\begin{aligned}
\Omega^2 = & -\frac{5p}{6} + \sqrt[3]{\frac{27\left(\frac{125p^3}{108} - \frac{5p(p^2 - r)}{3} + \frac{4p^2 - 4pr - q^2}{8}\right) + \sqrt{729\left(\frac{125p^3}{108} - \frac{5p(p^2 - r)}{3} + \frac{4p^2 - 4pr - q^2}{8}\right)^2 + 108\left(\frac{25p^2}{12} + 2(p^2 - r)\right)}}{54}} \\
& + \sqrt[3]{\frac{27\left(\frac{125p^3}{108} - \frac{5p(p^2 - r)}{3} + \frac{4p^2 - 4pr - q^2}{8}\right) - \sqrt{729\left(\frac{125p^3}{108} - \frac{5p(p^2 - r)}{3} + \frac{4p^2 - 4pr - q^2}{8}\right)^2 + 108\left(\frac{25p^2}{12} + 2(p^2 - r)\right)}}{54}}
\end{aligned}
\tag{22}
$$

$$
p = -3i(\gamma_r + \gamma_s)^3 - 4\gamma_r\gamma_s - \omega_r^2 - \omega_s^2 \tag{23}
$$

$$
q = -i\left(-(\gamma_r + \gamma_s)(4\gamma_r\gamma_s + \omega_r^2 + \omega_s^2) - 2(\omega_r^2\gamma_s + \gamma_r\omega_s^2) + (\gamma_r + \gamma_s)^3\right), \tag{24}
$$

$$
\begin{aligned}
r = & \frac{3(\gamma_s + \gamma_r)^4}{16} + \frac{(\gamma_s + \gamma_r)^2\left(4\gamma_r\gamma_s + \omega_s^2 + \omega_r^2\right)}{4} \\
& + (\gamma_s + \gamma_r)(\gamma_r\omega_s^2 + \gamma_s\omega_r^2) + (\omega_s^2\omega_r^2 - \omega_{d,s}^2\omega_{d,r}^2).
\end{aligned}
\tag{25}
$$

2.5. Damping

It is interesting to note that damping enters directly through the average $(\gamma_s + \gamma_r)/2$ of the individual damping coefficients γ_r, γ_s as specified in Equation (11) and Equation (12). Under physical assumptions regarding the measurement parameters, $k_s, k_r, \gamma_s, \gamma_r, m_s, m_r$ and the fit parameter k_0, we may assume that all four roots (18), (19), (20), and (21) are pairwise distinct. By a small variation of the parameters within the range of measurement uncertainty, this assumption can be fulfilled trivially. We denote by $\mathcal{Z}$ the resulting set of the four solutions ω to the eigenvalue problem of the matrix M.

2.6. Calculation of the Matrix Exponentials

To obtain x_s and x_r from (15) and (16), we need to calculate the matrix exponential. The calculation is performed with the aid of Mathematica.

We find

$$x_s(t) = \sum_{\omega \in \mathcal{Z}} \int_0^t \mathrm{d}\tau\, G_\omega(t - \tau) a_r(\tau), \tag{26}$$

$$x_r(t) = \sum_{\omega \in \mathcal{Z}} \int_0^t \mathrm{d}\tau\, H_\omega(t - \tau) a_r(\tau) \tag{27}$$

where the sum runs over the four solutions $\omega_1, \omega_2, \omega_3, \omega_4$ obtained in the previous paragraph. The kernels $G_\omega(t - \tau)$ and $H_\omega(t - \tau)$ are obtained from the eigenmode solutions upon diagonalization of M and defined such that

$$\left[\mathrm{e}^{(t-\tau)M} \right]_{14} = \sum_{\omega \in \mathcal{Z}} G_\omega(t - \tau), \tag{28}$$

$$\left[\mathrm{e}^{(t-\tau)M} \right]_{34} = \sum_{\omega \in \mathcal{Z}} H_\omega(t - \tau). \tag{29}$$

Assuming regularity of the input force F and thus of a_r and by the assumption of distinctness of the $\omega_k \in \mathcal{Z}$, the sum and the integral in the solution formulas (26) and (27) have been interchanged. Using the computational methods summarized above, we find the convolution kernels G_ω and H_ω to be given by

$$G_\omega(t - \tau) = \frac{\omega_{d,r}^2}{2} \frac{\mathrm{e}^{i\omega(t-\tau)}}{-2i\omega^3 - 3\omega^2\gamma_r - 3\omega^2\gamma_s + 4i\omega\gamma_r\gamma_s + i\omega\omega_r^2 + i\omega\omega_s^2 + \omega_r^2\gamma_s + \gamma_r\omega_s^2} \tag{30}$$

$$H_\omega(t - \tau) = \frac{1}{2} \frac{-\omega^2 \mathrm{e}^{i\omega t - \tau} + 2i\omega\gamma_r \mathrm{e}^{i\omega t - \tau} + \omega^2 \mathrm{e}^{i\omega t - \tau}}{-2i\omega^3 - 3\omega^2\gamma_r - 3\omega^2\gamma_s + 4i\omega\gamma_r\gamma_s + i\omega\omega_r^2 + i\omega\omega_s^2 + \omega_r^2\gamma_s + \gamma_r\omega_s^2}. \tag{31}$$

Needless to say that although the model is simple and captures the physics of a combined movement of the spherical shell membrane due to bending and the elastic deformation of the supporting ring, the solution is somewhat cumbersome.

3. Numerics & Physical Discussion

3.1. Numerical Results

For the numerical simulation we use a time scale with units ω_r^{-1} and a length scale of units $F_0 / (m_r \omega_r^2)$. The remaining parameters are fixed by $\gamma_r = 0.5\omega_r$, $\gamma_s = 0.7\omega_r$, $\omega_s^2 = 0.8\omega_r^2$ and $m_s = m_r$. The fit constant k_0 is chosen such that

$\omega_{d,s}^2 = \omega_{d,r}^2 = 0.25\omega_r^2$ and $\omega = 0.9\omega_r$. In the top row of **Figure 3**, one sees that the elastic ring vibrates at a larger amplitude than the amplitude of bending of the spherical shell for both the real part (left) and the imaginary part (right) of the solution for the input $\exp(i0.8t)$ in the unit system specified above.

The color code employed in **Figure 3** is as follows for the ring's vertical elastic displacement x_r. The real part $\Re[x_r]$ in the top left plot and the imaginary part $\Im[x_r]$ in the top right plot are shown as solid blue curves. As for the shell's bending displacement x_s, the following color code is employed in **Figure 3**. The real part $\Re[x_s]$ in the top left plot and the imaginary part $\Im[x_s]$ in the top right plot are shown is solid orange curves. Varying the parameter k_0 in the model simulation, it is found that the smaller k_0, the smaller the amplitude of x_s.

For the same choice of parameters, we have plotted the ratio

$$\left|\Re[x_s]\right| / \left(\left|\Re[x_s]\right| + \left|\Re[x_r]\right|\right)$$

in the bottom-left plot of **Figure 3** and

$$\left|\Im[x_s]\right| / \left(\left|\Im[x_s]\right| + \left|\Im[x_r]\right|\right)$$

in the bottom-right plot of **Figure 3**. By definition, both ratios are smaller than unity. This is indicated by the orange lines in the two bottom plots. The ratios
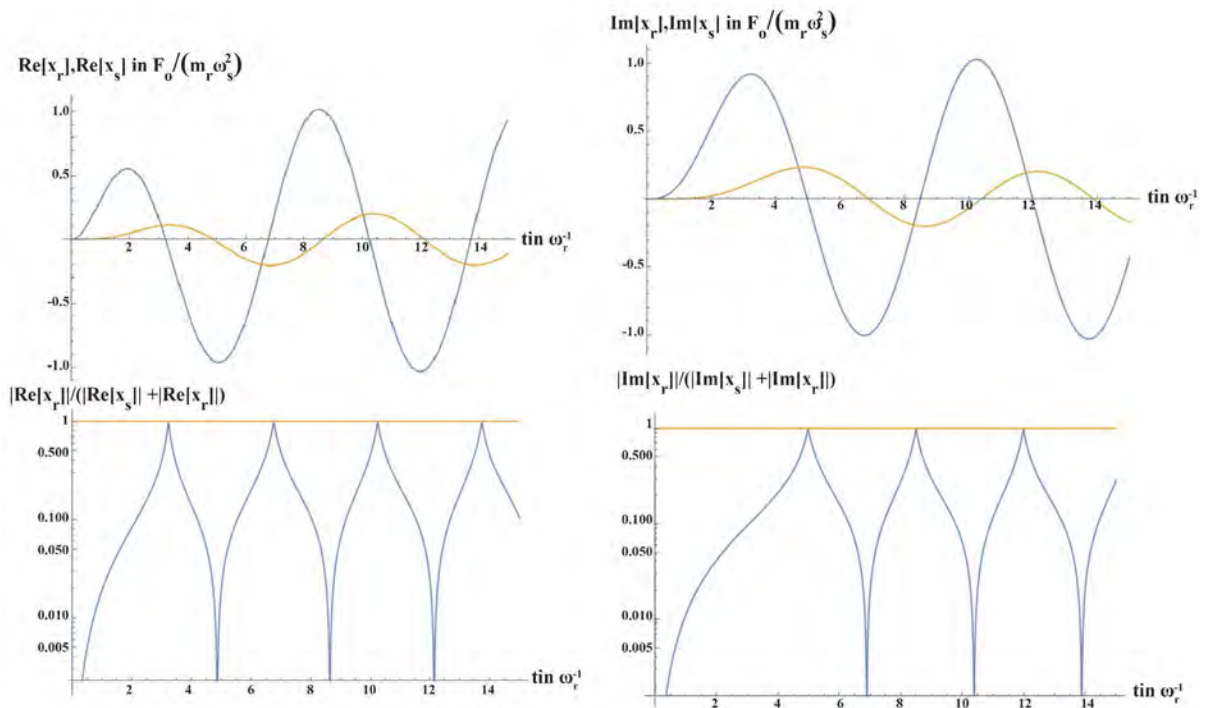
Figure 3. Top-left plot: $\Re[x_r]$ (blue) and $\Re[x_s]$ (orange) in units of $F_0/(m_r\omega_r^2)$ over time $t \in [0,15]$ in units of ω_r^{-1}. Bottom-left: Absolute displacement over sum of absolute displacements $\left|\Re[x_s]\right| / \left(\left|\Re[x_s]\right| + \left|\Re[x_r]\right|\right)$ as a function of $t \in [0,15]$ measured in units of ω_r^{-1} Top-and bottom-right plots: Analogous plots as in the left column with the corresponding imaginary parts used instead of the real parts.

quantify how important the bending of the plate is in comparison to the vertical oscillation of the ring at a given time t. The peaks in the bottom row plots in **Figure 3** result from distinct zeros of $\Re[x_s], \Re[x_r]$ and $\Im[x_s], \Im[x_r]$. Yet, and most of the time, the bending of the spherical shell is small compared to the vertical displacement of the ring.

The amplitude ratios $\max \Im[x_s]/\max \Im[x_r]$ and $\max \Re[x_s]/\max \Re[x_r]$ have been found by looking for the maximum amplitudes in $t \in [4,15]$ after the periodic behavior stabilizes in the range $t \gtrsim 4$ because of relaxation of the system (by damping) into the quasi-stationary state. We found

$$\max \Im[x_s]/\max \Im[x_r] \approx 0.2 \approx \max \Re[x_s]/\max \Re[x_r],$$

rounded mathematically to one counting digit. This agrees with the reasoning of the introduction that the elastic ring is the preferred constituent of the tympanic structure of multitudinous archosaurs to generate the fundamental frequency that is processed further by ICE. As for the extracolumella that is wired to the cochlea, the relative smallness of the bending of the shell compared to the elastic stretching of the ring implies that the its deflection from equilibrium, $x_s + x_r$, can be approximated as x_r for sufficiently small k_0 compared to k_r and k_s.

3.2. Physical Discussion

The quantity of keen interest to model builders in auditory research is the velocity of the tympanic membrane, or, more generally, of the tympanic structure [13]. While for geckos and frogs the interaural cavity can be and has been approximated by a cylinderical acoustic waveguide of equivalent volume [3] [4] [6], the archosaur counterpart has the topology of a, sometimes even higher-genus, torus [21]. In view of ongoing analytic approaches to the study of hearing in "icy" animals, the geometric complexity as well as the number of equations required for mathematical description both necessitate approximations for efficient solutions. The piston approximation in conjunction with approximate modeling of the entire interaural cavity as effectively one-dimensional wave guide form the base of the preferential toolkit.

For comparison with biological data, quantities of the structure

$$\text{ILD} = 20\log_{10}\left|\frac{\dot{u}_L}{\dot{u}_R}\right| \tag{32}$$

have proved useful [3] [4]. Such quantities are inspired by the definition of the sound pressure level in acoustics. Via no-penetration boundary conditions $\rho_{\text{air}}\partial_t(\partial_t u) = -(\hat{\boldsymbol{n}} \cdot \nabla p)$ at the eardrums, these quantities compare the acoustic pressure at the left to the one at the right ear. In Equation (32), $\dot{u}_L$ and $\dot{u}_R$ denote the (total) speed of the left and right tympanic membrane. In the new case of a tympanic structure with more than one constituent, a similar measure can be obtained by considering the total displacement of the tympanic structure, denoted by U_L and U_R. In the case of the present two-spring model, we iden-

tify $\dot{U}_L = \dot{x}_{s,L} + \dot{x}_{r,L}$ and $\dot{U}_R = \dot{x}_{s,R} + \dot{x}_{r,R}$ for the total speed at the left and right tympanic structure. The substitutions $u_L \rightarrow U_L$ and $u_R \rightarrow U_R$ in (32) result in

$$\text{ILD} = 20\log_{10} \left| \frac{\dot{x}_{s,L} + \dot{x}_{r,L}}{\dot{x}_{s,R} + \dot{x}_{r,R}} \right|. \tag{33}$$

The primary objective of this work is to provide auditory research with a practically applicable model for the tympanic structure of numerous archosaurs. We discuss a simpler treatment of the two-spring model in Section 4.1.

4. Approximate Solution

4.1. Iterative Solution of the Two-Spring Model

Since the constituents of the tympanic structure—see (11) and (12)—are damped, an iterative solution is to be favored instead of the lengthy closed form solution derived in the previous paragraph. By iterative solution, we mean a decoupling of the equations of motion for the full tympanic structure into the individual equations of motion for its constituents using the assumption $k_0 < \min\{k_r, k_s\}$.

Because of damping, the impact of higher-order coupled contributions to the displacement of either constituent from the other constituent will decrease in time. We refer to Hassani [18] for a mathematical introduction to operators as used in physics. For the sake of notational brevity, we introduce the following constant-coefficient differential operators

$$\text{D}_s^2 \equiv m_s d_t^2 + 2m_s \gamma_s d_t + k_s, \tag{34}$$

$$\text{D}_r^2 \equiv m_r d_t^2 + 2m_r \gamma_r d_t + k_r. \tag{35}$$

They are defined on the space $\mathcal{H} = \mathcal{C}^2\left(\mathbb{R}_0^+ \rightarrow \mathbb{C}\right)$. Moreover, we require the driving force F to be smooth. Both operators are accompanied by homogeneous initial conditions. We have $\left[\text{D}_r^2, \text{D}_s^2\right] = 0$ on $\mathcal{H} \cap \mathcal{C}^4\left(\mathbb{R}_0^+ \rightarrow \mathbb{C}\right)$. That is, the operators defined in (34) and (35) commute for high enough regular functions. The governing equations of the two-spring model read in operator notation

$$\text{D}_s^2 [x_s] = k_0 x_r \,\&\, \text{D}_r^2 [x_r] = k_0 x_s + F. \tag{36}$$

Using one of Schwarz' representation theorems, we can represent the inverse operator by a convolution-type integral [18]. Let $\bullet \in \mathcal{C}^0\left(\mathbb{R}_0^+ \rightarrow \mathbb{C}\right)$ and $t \geq 0$. We then find

$$\text{D}_s^{-2} [\bullet](t) = \int_0^t \frac{\mathrm{d}\tau \mathrm{e}^{-\gamma_s(t-\tau)} \sin\left(\sqrt{\omega_s^2 - \gamma_s^2}\,(t-\tau)\right)}{m_s \sqrt{\omega_s^2 - \gamma_s^2}} \bullet(\tau), \tag{37}$$

$$\text{D}_r^{-2} [\bullet](t) = \int_0^t \frac{\mathrm{d}\tau \mathrm{e}^{-\gamma_r(t-\tau)} \sin\left(\sqrt{\omega_r^2 - \gamma_r^2}\,(t-\tau)\right)}{m_r \sqrt{\omega_r^2 - \gamma_r^2}} \bullet(\tau). \tag{38}$$

By direct computation, it is seen that $\text{D}_r^2 \circ \text{D}_r^{-2} = 1 = \text{D}_r^{-2} \circ \text{D}_r^2$ on $\mathcal{H}$ and analogously for D_s^2 and D_s^{-2}.

Next, the smoothness assumption $F \in \mathcal{C}^{\infty}\left(\mathbb{R}_0^+ \to \mathbb{C}\right)$ allows us to confine the search to smooth solutions $x_s, x_r \in \mathcal{H} \bigcap \mathcal{C}^{\infty}\left(\mathbb{R}_0^+ \to \mathbb{C}\right)$. If we are able to find such x_s and x_r, the existence and uniqueness theorems from the theory of ordinary differential equations guarantee that we have also found the only solution to the inhomogeneous initial value problem. Using the inverse operators (37) and (38), we recast (36) into the equivalent system of integral equations

$$x_s = k_0 D_s^{-2}\left[x_r\right] \& x_r = k_0 D_r^{-2}\left[x_s\right] + D_r^{-2}\left[F\right] \tag{39}$$

The Banach fixed-point theorem entails a construction to obtain the fixed-point by iteration. In order to satisfy the model's initial conditions, we choose $\left(x_s, x_r\right) = (0,0) \in \mathcal{H}_{\infty}$. Let $t > 0$ and define for all $n \in \mathbb{N}$ by

$$\left(t_0 = 0, t_1, \cdots, t_n = t\right) \in \left(\mathbb{R}_0^+\right)^n$$

with $t_i < t_{i+1}$ for $0 < i < n-1$ a subdivision of $[0,t]$. We introduce the notation for subdivisions $\left(t_0, t_1, t_2\right) \in \left(\mathbb{R}_0^+\right)^3$,

$$\left(t_0, t_1, t_2, \cdots, t_{2k-1}, t_{2k}\right) \in \left(\mathbb{R}_0^+\right)^{2k+1}, k > 1$$

with the properties declared above

$$\begin{aligned} A_{t_1, t_2}\left[\bullet\left(t_0\right)\right]\left(t_2\right) &\equiv D_s^{-2}\left[D_r^{-2}\left[\bullet\left(t_0\right)\right]\left(t_1\right)\right]\left(t_2\right), \\ A_{t_1, \cdots, t_{2k}} &\equiv A_{t_1, \cdots, t_{2k-2}} \circ A_{t_1, t_2}. \end{aligned} \tag{40}$$

The indices have been inserted in the definition of the A operators to make the nesting of integrals explicit. They indicate the integration variables in the nested integrals.

For $t > 0$, we find the following series representation for the components of $\left(x_s, x_r\right)$

$$x_s(t) = \left(\sum_{m=1}^{\infty} k_0^m A_{t_1, \cdots, t_{2m}}\left[F\left(t_0\right)\right]\right)(t), \tag{41}$$

$$x_r(t) = \left(\sum_{m=0}^{\infty} k_0^m D_r^{-2}\left[A_{t_1, \cdots, t_{2m}}\left[F\left(t_0\right)\right]\right]\right)(t). \tag{42}$$

The above expression is not a Neumann series because of the appearance of the nested integrals. It cannot be summed up to a closed-form solution. Recalling the fixed-point argument from above, we see that the maximum norm of the series converges. The regularity properties of x_s, x_r are the result of smoothness of the input F and the fact that the operators (37) and (38) have smooth integration kernels and thus do not decrease the regularity of their arguments. Equations (41) and (42) can be applied in practice by truncating the series. In the next paragraph, we compare truncations of the series solutions (41) and (42) with the exact solutions of the two-spring model for a given parameter set.

4.2. Discussion of the Applicability in Auditory Research

We state the first two iterations. In the notation of the previous paragraph, this corresponds to $x_s^{(N)}, x_r^{(N)}$ with $N \in \{1, 2\}$,

$$x_r^{(1)}(t) = \int_0^t \frac{d\tau e^{-\gamma_r(t-\tau)}\sin\left(\sqrt{\omega_r^2 - \gamma_r^2}(t-\tau)\right)}{m_r\sqrt{\omega_r^2 - \gamma_r^2}} F(\tau), \tag{43}$$

$$x_s^{(1)}(t) = \omega_{d,r}^2 \int_0^t \frac{d\tau e^{-\gamma_s(t-\tau)}\sin\left(\sqrt{\omega_s^2 - \gamma_s^2}(t-\tau)\right)}{m_s\sqrt{\omega_s^2 - \gamma_s^2}}$$
$$\cdot\left[\int_0^\tau \frac{d\tau' e^{-\gamma_r(\tau-\tau')}\sin\left(\sqrt{\omega_r^2 - \gamma_r^2}(\tau-\tau')\right)}{\sqrt{\omega_r^2 - \gamma_r^2}} F(\tau')\right], \tag{44}$$

$$x_r^{(2)}(t) = \int_0^t \frac{d\tau e^{-\gamma_r(t-\tau)}\sin\left(\sqrt{\omega_r^2 - \gamma_r^2}(t-\tau)\right)}{m_r\sqrt{\omega_r^2 - \gamma_r^2}} F(\tau)$$
$$+ \omega_{d,r}^2\omega_{d,s}^2 \int_0^t \frac{d\tau e^{-\gamma_r(t-\tau)}\sin\left(\sqrt{\omega_r^2 - \gamma_r^2}(t-\tau)\right)}{m_r\sqrt{\omega_r^2 - \gamma_r^2}}$$
$$\cdot\left\{\int_0^\tau \frac{d\tau' e^{-\gamma_s(\tau-\tau')}\sin\left(\sqrt{\omega_s^2 - \gamma_s^2}(\tau-\tau')\right)}{\sqrt{\omega_s^2 - \gamma_s^2}}\right.$$
$$\left.\cdot\left[\int_0^{\tau'} \frac{d\tau'' e^{-\gamma_r(\tau'-\tau'')}\sin\left(\sqrt{\omega_r^2 - \gamma_r^2}(\tau'-\tau'')\right)}{\sqrt{\omega_r^2 - \gamma_r^2}} F(\tau'')\right]\right\}, \tag{45}$$

$$x_s^{(2)}(t) = \omega_{d,r}^2 \int_0^t \frac{d\tau e^{-\gamma_s(t-\tau)}\sin\left(\sqrt{\omega_s^2 - \gamma_s^2}(t-\tau)\right)}{m_s\sqrt{\omega_s^2 - \gamma_s^2}}$$
$$\cdot\left[\int_0^\tau \frac{d\tau' e^{-\gamma_r(\tau-\tau')}\sin\left(\sqrt{\omega_r^2 - \gamma_r^2}(\tau-\tau')\right)}{\sqrt{\omega_r^2 - \gamma_r^2}} F(\tau')\right]$$
$$+ \omega_{d,s}^2\omega_{d,r}^4 \int_0^t \frac{d\tau e^{-\gamma_s(t-\tau)}\sin\left(\sqrt{\omega_s^2 - \gamma_s^2}(t-\tau)\right)}{m_s\sqrt{\omega_s^2 - \gamma_s^2}}$$
$$\cdot\left\{\int_0^\tau \frac{d\tau' e^{-\gamma_r(\tau-\tau')}\sin\left(\sqrt{\omega_r^2 - \gamma_r^2}(\tau-\tau')\right)}{\sqrt{\omega_r^2 - \gamma_r^2}}\right.$$
$$\left.\cdot\left[\int_0^{\tau'} \frac{d\tau'' e^{-\gamma_s(\tau'-\tau'')}\sin\left(\sqrt{\omega_s^2 - \gamma_s^2}(\tau'-\tau'')\right)}{\sqrt{\omega_s^2 - \gamma_s^2}}\right.\right.$$
$$\left.\left.\cdot\left(\int_0^{\tau''} \frac{d\tau''' e^{-\gamma_r(\tau''-\tau''')}\sin\left(\sqrt{\omega_r^2 - \gamma_r^2}(\tau''-\tau''')\right)}{\sqrt{\omega_r^2 - \gamma_r^2}} F(\tau''')\right)\right]\right\}. \tag{46}$$

From the phenomenological point of view, the "strength" of coupling can be determined from the ratios $\omega_{d,s}^2/\omega_s^2 = k_0/k_s$ or $\omega_{d,r}^2/\omega_r^2 = k_0/k_r$ for 2-constituent tympanic structures. By the assumptions regarding k_0, both ratios

are smaller than unity. A suitable smallness parameter is defined through $\epsilon = \max\left\{k_0/k_s, k_0/k_r\right\}$. By mathematical induction it follows

$$\left|x_s^{(N)} - x_s^{(N-1)}\right|/\left|x_s^{(N-1)}\right| \sim \left|x_r^{(N)} - x_r^{(N-1)}\right|/\left|x_s^{(N-1)}\right| \sim \epsilon^2.$$

The series solution gradually builds up the coupling between the two constituents of the tympanic structure.

4.3. Numerical Results

In order to assess the accuracy of the iterative solution developed in this section, we simulate the Equation (43) and Equation (44), respectively (45) and (46), for both the parameter choice and the input model used for the simulation of the full two-spring model presented the previous section. The numerical results for (43) and (44) are shown in **Figure 4**. The axis units therein have been chosen in accordance with **Figure 3** and the unit system introduced at the beginning of the previous section. The numerical results for (45) and (46) are shown in **Figure 5**. In each of **Figure 4** and **Figure 5**, the left column depicts results for the real parts $\Re\left[x_r^{(1)}\right]$ and $\Re\left[x_s^{(1)}\right]$, respectively $\Re\left[x_r^{(2)}\right]$ and $\Re\left[x_s^{(2)}\right]$.

The right columns of **Figure 4** and **Figure 5** show the results for $\Im\left[x_r^{(1)}\right]$ and $\Im\left[x_s^{(1)}\right]$, respectively $\Im\left[x_r^{(2)}\right]$ and $\Im\left[x_s^{(2)}\right]$. In the top row of **Figure 4**, $\Re\left[x_r^{(1)}\right], Im\left[x_r^{(1)}\right]$ is shown as solid blue curves, while $\Re\left[x_s^{(1)}\right], Im\left[x_s^{(1)}\right]$ is represented by the solid orange curves. The same color code has been employed in the top row of **Figure 5** with $x_r^{(2)}$ and $x_s^{(2)}$ used in place of $x_r^{(1)}$ and $x_s^{(1)}$.

The bottom rows of the two figures are devoted to quantifying the absolute deviations from the full solution obtained by means of the simulation presented in the previous section. In the two bottom plots of **Figure 4**, the differences $\left|\Re[x]_r^{(1)}\right| - \left|\Re[x]_r\right|$ and $\left|\Re[x]_s^{(1)}\right| - \left|\Re[x]_s\right|$ are shown as the solid blue and solid orange curve on the left and the differences $\left|\Im[x]_r^{(1)}\right| - \left|\Im[x]_r\right|$ and $\left|\Im[x]_s^{(1)}\right| - \left|\Im[x]_s\right|$ are shown as the solid blue and solid orange curve on the right. Similarly, the differences $\left|\Re[x]_r^{(1)}\right| - \left|\Re[x]_r\right|$ and $\left|\Re[x]_s^{(1)}\right| - \left|\Re[x]_s\right|$ are shown as the solid blue and solid orange curve in the left plot and the differences $\left|\Im[x]_r^{(1)}\right| - \left|\Im[x]_r\right|$ and $\left|\Im[x]_s^{(1)}\right| - \left|\Im[x]_s\right|$ are shown as the solid blue and solid orange curve in the right plot of the bottom row in **Figure 5**.

At a first sight, the top rows of **Figure 4** and **Figure 5** look like their "exact" pendants in the top row of **Figure 5**. We see, however, that the deviations of the moduli of the real and imaginary part of the first iterates, *i.e.*, (43) and (44), from the moduli of the real and imaginary part of the exact solution of the two-spring model do not equilibrate fast into the quasi-stationary state behavior; cf. the bottom row of **Figure 4**.

In contrast, the bottom row of **Figure 5** shows that, for the specified parameter values, the moduli of the real and imaginary part of the exact solution of the two-spring model and the absolute values (45) and (46) of the real and imaginary part of the second iterates match well, as compared with the amplitude of the exact solution, after equilibration into the quasi-stationary state. For $t \gtrsim 6\omega_r^{-1}$, the
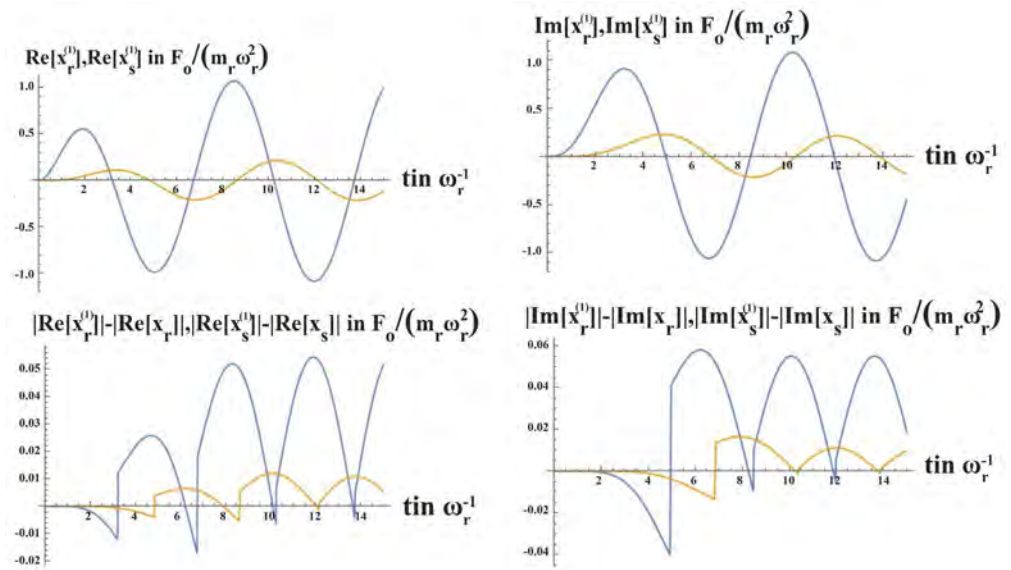
Figure 4. Top-left: Approximate solution $\Re\left[x_r^{(1)}\right]$ (blue) and $\Re\left[x_s^{(1)}\right]$ (orange) in units of $F_0\big/\left(m_r\omega_r^2\right)$ after the first iteration as a function of $t\in[0,15]$ in units of ω_r^{-1}. Bottom-left: Comparison of the solution for the full two-spring model with the approximate solutions: $\left|\Re\left[x_r^{(1)}\right]\right|-\left|\Re\left[x_r\right]\right|$ (blue) and $\left|\Re\left[x_s^{(1)}\right]\right|-\left|\Re\left[x_s\right]\right|$ (orange) in units of $F_0\big/\left(m_r\omega_r^2\right)$ as a function of $t\in[0,15]$ in units of ω_r^{-1} Top- and bottom right: Analogous plots as in the left column with the corresponding imaginary parts used in place of the real parts.
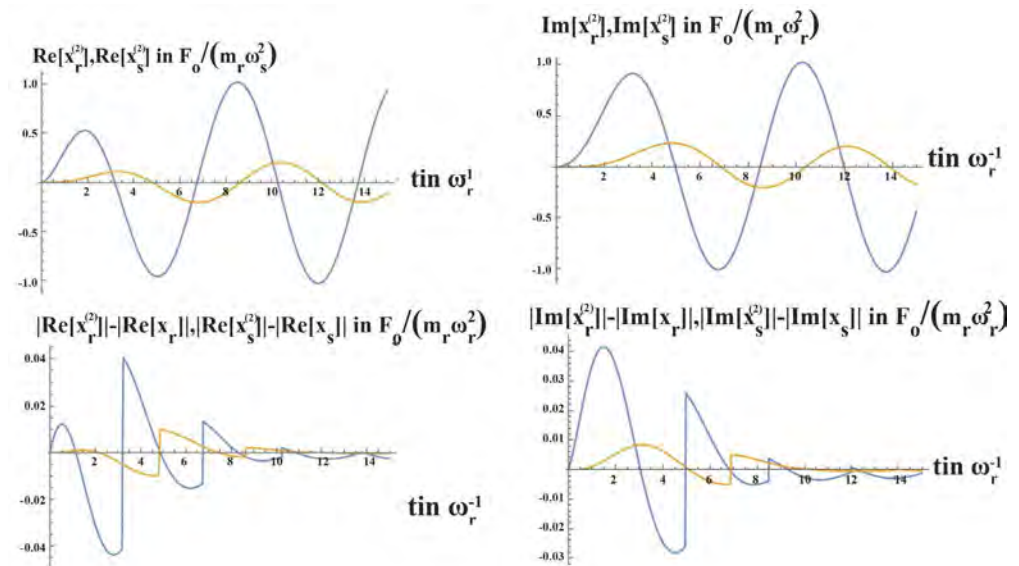
Figure 5. Top-left: Approximate solution $\Re\left[x_r^{(2)}\right]$ (blue) and $\Re\left[x_s^{(2)}\right]$ (orange) in units of $F_0\big/\left(m_r\omega_r^2\right)$ after the second iteration as a function of $t\in[0,15]$ in units of ω_r^{-1}. Bottom-left: Comparison of the solution for the full two-spring model with the approximate solutions: $\left|\Re\left[x_r^{(2)}\right]\right|-\left|\Re\left[x_r\right]\right|$ (blue) and $\left|\Re\left[x_s^{(2)}\right]\right|-\left|\Re\left[x_s\right]\right|$ (orange) in units of $F_0\big/\left(m_r\omega_r^2\right)$ as a function of $t\in[0,15]$ in units of ω_r^{-1}. Top- and bottom-right: Analogous plots as in the left row with the corresponding imaginary parts used in place of the real parts.

relative deviation compared to the amplitudes is below 1% for both real and imaginary part for both the ring and the shell displacement. This is lower than the relative deviation compared to the amplitude of the oscillation of the real and imaginary part of x_r and x_s found for the first iterates from the bottom row of Figure 4. In this case, we find the ratio in question being under 6% for $t \gtrsim 6\omega_r^{-1}$.

5. Summary

For the first time in auditory research, we have articulated a physically implementable definition of tympanic structures that generalizes the notion of a tympanic membrane. In the terminology introduced in the main body of the present article, a tympanic membrane is seen to be a special case of the wider notion of "tympanic structure". The case of archosaurs as "icy" animals exemplified the necessity to define a more general notion in order to model the tympanic responses in these animals in a physically meaningful way. Favoring applicability of the ICE model in auditory research over mathematical complexity, the two-spring model has been derived from the piston approximation applied to the elastic constituents of the 2-constituent tympanic structure as observed in numerous archosaurs. Two damped harmonic oscillators, interacting via a Hooke-elastic coupling, were found to account for the combined motion of the tympanic structure. That is, the displacement of the spherical shell membrane of the animals without local bending and bending of the shell.

By numerical simulations with parameters chosen from the expected parameter range, the biologically motivated hypothesis that the overall displacement of the extracolumella is mainly due to uniform, piston-like displacement of the shell as a whole without large contributions due to local bending, could be supported. Only a maximum of 20% of the extracolumella displacement's amplitude was found to be on the part of shell bending in the two-spring model with the chosen simulation parameters.

Because of the length of the analytic solution formulas, a simpler iterative treatment has been developed. Treating the two-spring model as a set of two damped, suitably weakly coupled harmonic oscillators, a Banach fixed-point iteration scheme has been derived. Simulations of the first two non-trivial iterates for the model solutions were performed using the same parameters as in the exact solution of the two-spring model. For sufficiently weak coupling of the two constituents of the tympanic structure, the second iterates were found to be sufficiently accurate and efficient-to-calculate at the same time so as to be favored over the exact solution, if the computational power available is limited. The strength of the coupling is stored in the parameter $\epsilon = \max\{k_0/k_r, k_0/k_r\}$, which requires specification through up-to-now unavailable experimental data.

Acknowledgements

for helpful suggestions regarding the literature on plates and shells, and Professor Bruce Young (A.T. Still University, Kirksville, MO) for insightful remarks concerning the anatomy of crocodilian eardrums. They apologize to the latter for biologically overly simplifying a mathematically highly complicated problem.

Conflicts of Interest

The authors declare no conflicts of interest regarding the publication of this paper.

References

[1] van Hemmen, J.L., Christensen-Dalsgaard, J., Carr, C.E. and Narins, P. (2016) Animals and ICE: Meaning, Origin and Diversity. *Biological Cybernetics*, **110**, 237-246. https://doi.org/10.1007/s00422-016-0702-x

[2] Schnupp, J. and Carr, C.E. (2009) One Hearing with More than One Ear: Lessons from Evolution. *Nature Neuroscience*, **12**, 692-697. https://doi.org/10.1038/nn.2325

[3] Vedumurdi, A.P. (2018) General Aspects of Sound Localization through Intenally Coupled Ears. PhD Thesis, Technische Universität München, München.

[4] Vossen, C. (2010) Auditory Information Processing in Systems with Internally Coupled Ears. PhD thesis, Technische Universität München, München.

[5] Vedurmudi, A.P., Goulet, J., Christensen-Dalsgaard, J., Young, B.A., Williams, R. and van Hemmen, J.L. (2016) How Internally Coupled Ears Generate Temporal and Amplitude Cues for Sound Localization. *Physical Review Letters*, **116**, 028101. https://doi.org/10.1103/PhysRevLett.116.028101

[6] C. Vossen, J. Christensen-Dalsgaard, and J. L van Hemmen. Analytical model of internally coupled ears. *Journal of the Acoustical Society of America*, 128(2):909-918, 2010. https://doi.org/10.1121/1.3455853

[7] Howe, M.S. (2007) Hydrodynamics and Sound. Cambridge University Press, Cambridge, UK.

[8] Howe, M.S. (2014) Acoustics and Aerodynamic Sound. Cambridge University Press, Cambridge, UK.

[9] Autrum, H. (1940) Über Lautäusserungen und Schallwahrnehmungen bei Anthropoden II. Das Richtungshören von Locusta und Versuch einer Hörtheorie für Tympanalorgane vom Locustidentyp. *Zeitschrift für Vergleichende Physiologie*, **28**, 326-352.

[10] Autrum, H. (1942) Schallempfang bei Tier und Mensch. *Naturwissenschaften*, **30**, 69-85. https://doi.org/10.1007/BF01475622

[11] Vedurmudi, A.P., Christensen-Dalsgaard, J. and van Hemmen, J.L. (2018) Modeling Underwater Hearing and Sound Localization in the Aquatic Frog *Xenopus laevis*. *Journal of the Acoustical Society of America*, Submitted.

[12] Vedurmudi, A.P., Young, B.A. and van Hemmen, J.L. (2016) Internally Coupled Ears: Mathematical Structures and Mechanisms Underlying ICE. *Biological Cybernetics*, **110**, 237-246. https://doi.org/10.1007/s00422-016-0696-4

[13] Fletcher, N.H. (1992) Acoustic Systems in Biology. Oxford University Press, Oxford, UK.

[14] Saunders, J.C., Duncan, R.K., Doan, D.E. and Werner, Y.L. (2000) The Middle Ear of Reptiles and Birds. In: Dooling, R.J., Fay, R.R. and Popper, A.N., Eds., *Comparative Hearing: Birds and Reptiles*, Springer, New York, Chapter 2. https://doi.org/10.1007/978-1-4612-1182-2_2

[15] Timoshenko, S.P. and Goodier, J. (1969) Theory of Elasticity. 3rd Edition, McGraw-Hill, New York.

[16] Timoshenko, S.P. and Woinowsky-Krieger, S. (1959) Theory of Plates and Shells. 2nd Edition, McGraw-Hill, New York.

[17] Van Hemmen, J.L. and Leibold, C. (2007) Elementary Excitations of Biomembranes: Differential Geometry of Undulations in Elastic Surfaces. *Physics Reports*, **444**, 51-99. https://doi.org/10.1016/j.physrep.2006.12.007

[18] Hassani, S. (2013) Mathematical Physics: An Introduction to Its Foundations. 2nd Edition, Springer, Berlin. https://doi.org/10.1007/978-3-319-01195-0

[19] Van der Waerden, B.L. (1993) Algebra I. 9th Edition, Springer, Berlin. https://doi.org/10.1007/978-3-642-85527-6

[20] Van der Waerden, B.L. (1993) Algebra II. 6th Edition, Springer, Berlin. https://doi.org/10.1007/978-3-642-58038-3

[21] Colbert, E. (1946) The Eustachian Tubes in the Crocodilia. *Copeia*, **12**, 12-14. https://doi.org/10.2307/1438813

[22] Spencer, P. and Moon, D. (1971) Field Theory Handbook: Including Coordinate Systems, Differential Equations and their Solutions. Springer, Berlin.

[23] Lautrup, B. (2004) Physics of Continuous Matter: Exotic and Everyday Phenomena in the Macroscopic World. IoP Publishing, Bristol.

[24] Skudrzyk, E. (1971) Foundations of Acoustics: Basic Mathematics and Basic Acoustics. Springer, Berlin. https://doi.org/10.1007/978-3-7091-8255-0

[25] Falloon, P., Abbott, P. and Wang, J. (2002) Theory and Computation of the Spheroidal Wave Functions. https://arxiv.org/ftp/math-ph/papers/0212/0212051.pdf

[26] Meixner, J. and Schäfke, R. (1954) Mathieusche Funktionen und Sphäroidfunktionen. Springer, Berlin. https://doi.org/10.1007/978-3-662-00941-3

[27] Meixner, J., Schäfke, R. and Wolf, G. (1980) Mathieu Functions and Spheroidal Functions and Their Mathematical Foundations (Further Studies). Lecture Notes in Mathematics 837. Springer, Berlin. https://doi.org/10.1007/BFb0096194

[28] Zhao, L. (2017) Spherical and Spheroidal Harmonics: Examples and Computations. Master's Thesis, Ohio State University, Columbus.

Appendix

The two-spring model is an effective model, a strong simplification of both biological and mathematical reality. In order to ensure the overall applicability of the model as well as the readability for a less mathematically inclined audience, a more complete, yet mathematically more advanced model, has been postponed to this appendix. Here spheroidal wave functions will appear at the end. Unfortunately, the state of the art in the numerics of spheroidal wave functions obstructs a detailed numerical evaluation while further analytic investigations are ruled out by the non-existence of closed form representations of spheroidal wave functions.

Geometry of the configuration

As explained in the main text, the two constituents of the tympanic structure in multitudinous archosaurs are (1) an elastic sectorial spherical shell and (2) an elastic circular symmetric ring. In spherical coordinates, the shell has radius R_0, azimuthal opening angle $\theta_0 \in [0, \pi/2]$, and a polar opening angle $\phi \in [\beta, 2\pi - \beta]$ where $0 < \beta \ll \pi$. The breaking of the full rotational symmetry of the tympanic structure results from the presence of the extracolumella; cf. **Figure 1**. It is a bony structure placed in the sector $\phi \in [0, \beta) \cup (2\pi - \beta, 2\pi]$ of the shell. The extracolumella effectively prevents vibrations *on* the shell surface itself. Yet, in the present model the shell is allowed to move up and down, the entire shell moving uniformly as a piston.

For the ensuing treatment, the extracolumella is assumed to be only connected to the shell but not to the underneath ring. The ring itself has radius R_0 and height H, extending in negative z-direction. We denote by $\Omega_s^0, \Omega_r^0 \subset \mathbb{R}^3$ the equilibrium surfaces of shell and ring,

$$\Omega_s^0 = S_{R_0}^2 \left(\mathbf{0}_{\mathbb{R}^3} \right) \bigcap \left\{ (x, y, z) \in \mathbb{R}^3 \mid z \geq 0 \right\}, \tag{47}$$

$$\Omega_r^0 = S_{R_0}^1 \left(\mathbf{0}_{\mathbb{R}^2} \right) \times [0, -H]. \tag{48}$$

For the elasto-dynamic analysis, it is useful to account for the small but finite thickness of the elastic constituents as well. Let us denote the corresponding compacta by $\Omega_s^{d_s}$ and $\Omega_r^{d_r}$ where $d_s, d_r \ll \min \{R_0, H\}$ stand for the thickness of the shell and the ring, respectively. We assume $d_s = d_r$ and use d_s as a symbol for the thickness of shell and ring. Explicitly, $\Omega_r^{d_s}$ and $\Omega_s^{d_s}$ are defined as

$$\Omega_s^{d_s} = \text{Cl} \left(B_{R_0 + d_s/2}^3 \left(\mathbf{0}_{\mathbb{R}^3} \right) \setminus B_{R_0 - d_s/2}^3 \left(\mathbf{0}_{\mathbb{R}^3} \right) \right) \bigcap \left\{ (x, y, z) \in \mathbb{R}^3 \mid z \geq 0 \right\}, \tag{49}$$

$$\Omega_r^{d_s} = \text{Cl} \left(B_{R_0 + d_s/2}^2 \left(\mathbf{0}_{\mathbb{R}^2} \right) \setminus B_{R_0 - d_s/2}^2 \left(\mathbf{0}_{\mathbb{R}^2} \right) \right) \times [0, H_0] \tag{50}$$

where $\text{Cl}(M)$ denotes the topological closure operation on the set M in brackets. Letting $d_s \geq 0$ tend to zero from above, we reproduce Ω_s^0 and Ω_r^0 as the maximal set contained in all the $\Omega_s^{d_s}$'s and $\Omega_r^{d_s}$'s, respectively. The interface between the two constituents is given the intersection $\Omega_s^{d_s} \bigcap \Omega_r^{d_s} \equiv \Gamma^{d_s}$. It is localized in the $z = 0$-plane, $\Gamma^{d_s} \subset \mathbb{R}^2 \times \{0\}$ and is isometrically homeomorphic

to the closed annulus $\overline{\mathbb{A}}_{R_0-d_s/2, R_0+d_s/2}$. If $d_s \geq 0$ tends to zero from above, the intersection of all the $\Gamma_s^{d_s}$'s gives $\Gamma^0 \equiv S_{R_0}^1 \left(\mathbf{0}_{\mathbb{R}^2} \right) \times \{0\}$.

Physical description of the problem

Each of the two constituents of the tympanic structure is an elastic material that satisfies approximately material isotropy and homogeneity assumptions. That is, shell and ring have respective Lamé constants (λ_s, μ_s) and (λ_r, μ_r). Since, even in the absence of a physical cause for deformations, the shell plus extracolumella has the shape of a hemisphere, it is treated as self-supporting: If stimulated by an pressure signal incident from the z-direction, the shell undergoes elastic deformations only along the z-direction.

Navier-Cauchy equation

The continuum momentum balance equations simplify to linear partial differential equations if only small elastic deformations are to be modeled. For the shell and the ring, they read quite generally

$$\rho_s \partial_t^2 \boldsymbol{u}_s = \nabla \boldsymbol{\sigma}_s + \boldsymbol{f}_s, \tag{51}$$

$$\rho_r \partial_t^2 \boldsymbol{u}_r = \nabla \boldsymbol{\sigma}_r + \boldsymbol{f}_r \tag{52}$$

where ρ_s, ρ_r denote the constant mass per volume density of shell and ring material, respectively, $\boldsymbol{f}_s$ and $\boldsymbol{f}_r$ stand for an external force density applied to the shell and ring, and $\boldsymbol{\sigma}_r$ and $\boldsymbol{\sigma}_r$ denote the (symmetric) stress tensors. The Navier-Cauchy equations [23] are obtained as a consequence of the assumption of a linear stress-strain relation. The linearized strain tensors $\boldsymbol{\epsilon}_r = 1/2 \cdot \left((\nabla \otimes \boldsymbol{u}_r) + (\nabla \otimes \boldsymbol{u}_r)^\mathrm{T} \right)$ and $\boldsymbol{\epsilon}_s = 1/2 \cdot \left((\nabla \otimes \boldsymbol{u}_s) + (\nabla \otimes \boldsymbol{u}_s)^\mathrm{T} \right)$ for the ring and shell occur in the linear stress-strain relation as

$$\left(\boldsymbol{\sigma}_s \right)_{ij} = \left(\boldsymbol{\Lambda}^{(s)} :: \boldsymbol{\epsilon}_s \right)_{ij} \quad \text{and} \quad \left(\boldsymbol{\sigma}_r \right)_{ij} = \left(\boldsymbol{\Lambda}^{(r)} :: \boldsymbol{\epsilon}_r \right)_{ij}.$$

The $::$ denotes double contraction in engineers' notation. The material homogeneity and isotropy assumptions reduce the number of components from *a priori* $3^4 = 81$ to 2 for both of the rank 4 tensors $\boldsymbol{\Lambda}^{(r)}$ and $\boldsymbol{\Lambda}^{(s)}$. The stress tensors $\boldsymbol{\sigma}_r$ and $\boldsymbol{\sigma}_s$ are themselves symmetric. They can only depend linearly on the respective strain tensor and the trace of the respective strain tensors. A textbook calculation [23] demonstrates that the Equation (51) and Equation (52) reduce to the elasto-dynamic equations, also known as the Navier-Cauchy equations,

$$\rho_s \partial_t^2 \boldsymbol{u}_s = (\lambda_s + 2\mu_s) \nabla (\nabla \cdot \boldsymbol{u}_s) - \mu_s \nabla \times \nabla \times \boldsymbol{u}_s + \boldsymbol{f}_s, \tag{53}$$

$$\rho_r \partial_t^2 \boldsymbol{u}_r = (\lambda_r + 2\mu_r) \nabla (\nabla \cdot \boldsymbol{u}_r) - \mu_r \nabla \times \nabla \times \boldsymbol{u}_r + \boldsymbol{f}_r. \tag{54}$$

Relations of the Lamé constants to other elastic parameters

Let λ and μ indicate Lamé's constants. The literature denotes μ occasionally by G and calls G the shear modulus. The expression $\lambda + \mu = G/(1 - 2\nu_p)$ defines the Poisson number ν and is smaller than 0.5. The Young's modulus E satisfies $E = 2G(1 + \nu) = 4\mu^2/(2\mu - \lambda)$. The bulk modulus K relates to the Lamé constants via $K = E/(3 \cdot (1 - 2\nu_p)) = (\lambda + \mu)(2\mu - \lambda)/(3\mu)$.

Model specification

The shell's force-density drive is assumed to take place only in the z-direction due to the self-supporting property of the shell. The prototypical external stimulus used in auditory research is a pressure signal emanating from a point far away from the shell surface so that a plane is the more appropriate shape for the wave front than a shell. Since the propagation speed of sound times a few milliseconds still exceeds the geometric dimensions of the tympanic structure, arrival time differences on the shell surfaces are negligible. Thus the net force-per-volume density on the shell is spatially uniform and purely time-dependent, and only has a non-trivial z-component: $\boldsymbol{f}_s = f_z^{(s)}(t)\hat{e}_z$.

Its relation to the acoustic pressure signal is established by considering the z-component of force-per-volume density to be the pressure difference along the thickness of the shell: $f_z^{(s)}(t) = p(t)/d_s$. Indeed, integrating over the homogeneous membrane's thickness d_s, we reproduce the pressure difference $p(t)$ as the force-per-surface density which is responsible for driving the system.

The ICE model has proven quite successful in auditory research [1] [12]. Due to the superposition principle, the investigation is confined to a pure tone, $p(t) = p_0 \exp(i\omega t)$ with a fixed positive stimulus angular frequency $\omega > 0$. The ring only interacts with the shell but receives no external stimulation, *i.e.*, $\boldsymbol{f}_r = \boldsymbol{0}$. The ring-shell interaction via boundary conditions will be discussed later on.

Our focus is on the quasi-stationary state. That is, the tympanic structure is assessed at a time where tympana's undulations generated previously have decayed as a result of damping. Mathematically, this amounts to working in frequency-domain space where linearity ensures that the tympana undulate with the same angular frequency ω as carried by the stimulus but in general with a phase shift for stimulus directions $\neq 0$. The self-supporting assumption reduces the components of the displacement vector field $\boldsymbol{u}_s$ from 3 to only 1, namely, to the component aligned in parallel to the external stimulus: $\boldsymbol{u}_s = u_s^{(z)}\hat{e}_z$.

As mentioned before, the shell rests on top of the ring. If piston-like motion is excited, the entire ring vibrates as if it were a point mass under the influence of Newton's law in vertical direction. Neglecting back-couplings of the ring's displacement to spatially dependent vibrations on the shell, the ring's displacement is aligned in parallel to $\boldsymbol{u}_s$ so that $\boldsymbol{u}_r = u_z^{(r)}(t)\hat{e}_z$. The configuration hints at using cylindrical coordinates for the spatial arguments of the functions $u_z^{(s)}$ and $u_z^{(r)}$. Upon insertion of the vector operators in cylindrical coordinates [22], (53) and (54) simplify,

$$\rho_s \partial_t^2 u_z^{(s)} = (\lambda_s + \mu_s)\partial_z^2 u_z^{(s)} + \mu_s \Delta_s u_z^{(s)} + p(t)/d_s, \tag{55}$$

$$\rho_r \partial_t^2 u_z^{(r)} = (\lambda_r + \mu_r)\partial_z^2 u_z^{(r)} + \mu_r \Delta_r u_z^{(r)}. \tag{56}$$

Δ_s and Δ_r denote the Laplace-Beltrami operators in cylindrical coordinates on the three-dimensional equilibria volumes of shell and ring. That is, on $\Omega_s^{d_s}$ and $\Omega_r^{d_s}$. The expression $\Delta_v = \nabla(\nabla \cdot) - \nabla \times \nabla \times$ can be utilized to convert (54)

and (53) to hyperbolic differential equations akin to (56) and (55) featuring only the vector Laplacian and the composition of gradient and divergence as differential operators in spatial variables.

Compressional coupling

We now deal with appropriate elastic matching conditions at the interface of ring and shell, *i.e.*, on Γ^{d_s}. Requiring validity of the differential Equation (56) and Equation (55) on $\Omega_r^{d_s} \supset\neq \Gamma^{d_s}$ and $\Omega_s^{d_s} \supset\neq \Gamma^{d_s}$, respectively, ensures that $u_z^{(s)}$ and $u_z^{(r)}$ are $\mathcal{C}^2$ on Γ^{d_s} as well. As a side comment this means that we would be allowed to extend the solutions to a larger but open domain, say, $\Omega_{r,+} \supset\neq \Omega_r^{d_s}$ and $\Omega_{s,+} \supset\neq \Omega_s^{d_s}$, so that we can already assume the solutions to be sufficiently well-behaved.

We recall that the compression of an elastic medium generates an excess pressure inside that medium through $p_m = -K_m \nabla \cdot \boldsymbol{u}_m$. The index m refers to the medium, whence $m \in \{r, s\}$ here. Upon insertion of the divergence operator in cylindrical coordinates and due to the ansatz for $\boldsymbol{u}_r$ and $\boldsymbol{u}_s$ from the previous paragraph, the excess pressures p_r and p_s are given by

$$p_r = -K_r \partial_z u_z^{(r)} \tag{57}$$

$$p_s = -K_s \partial_z u_z^{(s)} \tag{58}$$

The regularity requirement discussed at the beginning of this paragraph permits the usage of these expressions on the interface Γ^{d_s}. The difference in material generates a pressure difference $\delta p = p_r - p_s = -K_r \partial_z u_z^{(r)} + K_s \partial_z u_z^{(s)}$ localized at $z = 0$. One possible boundary condition would be to equate this compressional pressure difference and its partial derivative in *z*-direction to zero on Γ^{d_s}. In the configuration under consideration this is, however, not a good idea because the ring experiences yet another pressure on $\Gamma_s^{d_s}$. Viz., the one generated by pressure signal $p(t)$, which pulls the shell as a mass point up and down. The detailed discussion of the consequences is the subject of the next paragraph.

Here we confine ourselves to introducing the compressional coupling conditions at the interface $\Gamma_s^{d_s}$. In Newton's second law, the gradient of the pressure difference δp generates a force-per-volume. The boundary of shell and ring vibrate in such a way that the pressure gradients in positive and negative z-direction are compensated,

$$\rho_s \partial_t^2 u_z^{(s)} = \partial_z \delta p = -K_r \partial_z^2 u_z^{(r)} + K_s \partial_z^2 u_z^{(s)}, \tag{59}$$

$$\rho_r \partial_t^2 u_z^{(r)} = -\partial_z \delta p = K_r \partial_z^2 u_z^{(r)} - K_s \partial_z^2 u_z^{(s)}. \tag{60}$$

The equations express mathematically that the two constituent structures can be compressed at the interface. The resulting difference in excess pressures, δp, acts as force drive for the shell and the ring at the interface in the $z = 0$ plane. The bulk moduli K_r and K_s are material constants that can be determined from the Lamé constants (λ_r, μ_r) and (λ_s, μ_s) for the ring and shell, respectively, see the paragraph entitled "Relations of the Lamé constants to other elastic parameters". In order to deal with the piston mode where the total of shell

and extracolumella is driven as one point mass by the incident pressure signal needs to be considered in the above equations.

Force-collector model

Let us suppose that the shell is placed on an incompressible iron floor instead of an elastic ring. Since the shell is self-supporting and the pressure uniform, only forces in z-direction need to be considered. By Newton's third law, the iron floor enacts a excess normal force on the annular interface region of floor and shell as a reaction to the total of excess pressure driving the membrane. The resulting reaction force equates to the reaction pressure p_{int} times the area of the interface A_{int}. Since the shell obviously does not oscillate up and down through the "iron" force, the reaction force needs to compensate the total force generated by the incident pressure p on the area of the shell plus extracolumella as seen from a point on the z-axis, $A_{\text{hit}} = \pi R_0^2$. We note $A_{\text{hit}} \neq A_{\text{hemisphere}} = 2\pi R_0^2$ because radial oscillations of the sphere are prohibited by the self-supporting assumption. The interface region Γ^{d_s} between shell and floor is annular and has the area

$$A_{\text{int}} = \pi\left(R_0 + d_s/2\right)^2 - \pi\left(R_0 - d_s/2\right)^2 \simeq 2\pi R_0 d_s$$

neglecting contributions of order $\sim d_s^2/R_0^2$ relative to A_{hit}. The global force balance according to Newton's third law (actio = -reactio) translates into

$$p_{\text{int}} = -p_{\text{ext}} A_{\text{hit}}/A_{\text{int}} = -p_{\text{ext}} R_0/\left(2 d_s\right).$$

The difference between the iron floor and the elastic ring is that the latter experiences the interface pressure as an additional pressure. We observe that (59) needs no correction, if the piston mode is subtracted from $u_z^{(s)}$ since $u_z^{(s)}$ only quantifies dislocations generated by the compressional coupling between shell and ring.

One technical issue needs to be fixed. In the shell model (55) the pressure difference along the shell interface enters the force-per-volume balance rather than only an incident pressure gradient. The shell *collects* the pressure difference, the physical motivation for the nomenclature "force-collector model". It needs to be shown that the interface region Γ^{d_s} is subject to the *collected* pressure difference. Namely, the force-collector model demonstrates that an additional force-per-volume density acts on the ring at the boundary namely

$$f_{\text{ext}}^{\partial} = R_0/\left(2 d_s\right) \cdot p(t)/d_s .$$

Shell and ring extend in radial direction by d_s. Let us replace the fields $u_z^{(s)}$ and $u_z^{(r)}$ in (59) and (60) by their respective average along a ray segment of length d_s in the $\{z = 0\}$ plane. After multiplication by d_s, Equation (59) and Equation (60) read

$$\sigma_s \partial_t^2 u_{z,\text{avg}}^{(s)}\left(t, z = 0, \phi\right)$$
$$= -\left(K_s d_s\right)\partial_z^2 u_{z,\text{avg}}^{(s)}\left(t, z = 0, \phi\right) - \left(K_r d_s\right)\partial_z^2 u_{z,\text{avg}}^{(r)}\left(t, z = 0, \phi\right), \tag{61}$$

$$\sigma_r \partial_t^2 u_{z,\text{avg}}^{(r)}\left(t, z = 0, \phi\right)$$
$$= -\left(K_r d_s\right)\partial_z^2 u_{z,\text{avg}}^{(r)}\left(t, z = 0, \phi\right) - \left(K_s d_s\right)\partial_z^2 u_{z,\text{avg}}^{(s)}\left(t, z = 0, \phi\right). \tag{62}$$

The quantities σ_r and σ_s are effective surface mass densities defined through $\sigma_r \equiv \rho_r d_s$ and $\sigma_s \equiv \rho_s d_s$. Given that $d_s \ll R_0, H$, the approximation is sensible. Its advantage lies in the fact that $-p_{\text{int}}$ as specified at the beginning of the paragraph can be included in these boundary conditions in the spirit of the "force collector" argument,

$$\sigma_s \partial_t^2 u_{z,\text{avg}}^{(s)}(t, z=0, \phi)$$
$$= -(K_s d_s) \partial_z^2 u_{z,\text{avg}}^{(s)}(t, z=0, \phi) - (K_r d_s) \partial_z^2 u_{z,\text{avg}}^{(r)}(t, z=0, \phi), \tag{63}$$

$$\sigma_r \partial_t^2 u_{z,\text{avg}}^{(r)}(t, z=0, \phi)$$
$$= -(K_r d_s) \partial_z^2 u_{z,\text{avg}}^{(r)}(t, z=0, \phi) - (K_s d_s) \partial_z^2 u_{z,\text{avg}}^{(s)}(t, z=0, \phi) + \mathfrak{a}\, p(t). \tag{64}$$

The dimensionless quantity $\mathfrak{a} \equiv R_0 / (2d_s)$ is called amplification factor. Upon division by d_s, the statement that also the pressure difference along the interface is collected holds true in an approximate sense. Namely, we need to replace the fields $u_z^{(r)}$ and $u_z^{(s)}$ by the averages over the thickness of the annulus.

Effectively, we are left with fields on the interface Γ^0 rather than Γ^{d_s}. Indeed, $d_s \ll H, R_0$ already hints at using Ω_s^0 and Ω_r^0 in place of $\Omega_s^{d_s}$ and $\Omega_r^{d_s}$. We need to answer the question of whether or not to keep the source term in (55). In order to address this issue, we need to asses the ratio of maximum amplitudes of shell and ring. At the sphere's top at $(z=H_0)$, the shell experiences a pressure as $\sigma_s \partial_t^2 u_{z,\text{avg}}^{(s)}(t, z=H_0) = p(t)$. Neglecting spatial variations on the interface for the estimate, (64) reduces to

$$\sigma_r \partial_t^2 u_{z,\text{avg}}^{(r)}(t, z=0, \phi) = \mathfrak{a} p(t).$$

Since $p(t) \sim p_0 \exp(i\omega t)$, the quotient becomes

$$\frac{u_{z,\text{avg}}^{(s)}(t, z=H_0)}{u_{z,\text{avg}}^{(r)}(t, z=0, \phi)} = \frac{\sigma_s}{\sigma_r} \frac{1}{\mathfrak{a}} = \frac{\rho_s}{\rho_r} \frac{2d_s}{R_0} \ll 1 \tag{65}$$

in the quasi-stationary state, i.e., only the solution to the inhomogeneous problem is considered. The "$\ll$" awaits some justification.

Typically, $\rho_s \sim \mathcal{O}(\rho_r)$ because the material of the shell and ring are biological tissue. That is, mostly water. However, the thickness of the membrane $d_s \sim 10^{-5}\,\text{m} \ll R_0$ exceeds $R_0 \sim 0.5 \times 10^{-2}\,\text{m}$ by 2 to 4 orders of magnitude! Compared to the elastic deformation of the ring which experiences an amplification $\mathfrak{a}p_0$ of the pressure collected by the shell, the shell only a pressure of amplitude p_0. The amplification factor $\mathfrak{a}$ contains purely geometrical information, $\mathfrak{a} = R_0 / (2d_s) = A_{\text{hit}} / A_{\text{int}}$. The estimate of the orders of magnitude shows that the maximum amplitude of the piston shell is small compared to the amplitude of the ring compression. The "up and down" oscillation of the shell plus extracolumella system is thus dominantly due to the compressional oscillation of the elastic ring as a response to the total pressure. It therefore makes sense to drop the source term in (55) and account for the external stimulus in (64) instead.

The limit of thin shells and rings, $d_s \to 0^+$

Since we are only interested in displacement averaged over the shell's thickness d_s, the variables r and z are no longer independent but subject to the constraint $r = r(z) = \sqrt{R_0^2 - z^2}$. The clamping due to the presence of the extracolumella is unproblematic and only settles $\phi \in [\beta, 2\pi - \beta]$. The constraint $r^2 + z^2 = R_0^2$ with $z \geq 0$ is a cue to try transforming the differential operator of the spatial variables in (55) into spherical coordinates. The problem, however, is that $\lambda_s + \mu_s \neq 0$. The case $\lambda_s + \mu_s = 0$ corresponds to a negative Poisson number, more precisely $\nu = -1$. The relation between the shell's Lamé constants λ_s and μ_s on the one hand and the Young's modulus E and the Poisson number ν on the other hand becomes ill-defined. Furthermore, the Poisson number is typically between 0 and 1/2. Biological tissue does not increase its volume in such a way that it gets thicker under application of an external pulling force. Rather, its volume stays constant or increases while the shell becomes thinner [23].

In view of the above issues, a different method to localize the shell on $r^2 + z^2 = R_0^2$ for $z \geq 0$ is what we look for. One possibility starts with redefining $z \equiv z' \cdot \aleph$ where $\aleph > 0$ is a suitable re-scaling factor involving the Lamé constants. It is then chosen so that the problematic partial differential operator with spatial variables in (55) equals the Laplacian in the new coordinates. $\aleph$ is then determined to be

$$\aleph \equiv \sqrt{2 + \frac{\lambda_s}{\mu_s}} > 1. \tag{66}$$

In the new coordinates (r, ϕ, z'), the physical hemisphere defined through $r^2 + z^2 = R_0^2$ with $z \geq 0$ is half of an oblate spheroidal hemisphere,

$$\frac{r^2}{R_0^2} + \frac{(z')^2}{\dfrac{R_0^2}{\aleph^2}} = 1. \tag{67}$$

Implementing the deliberations outlined above, (55) reads in (z', r)-coordinates

$$\rho_s \partial_t^2 u_z^{(s)} = \mu_s \left(r^{-1} \partial_r \left(r \partial_r u_z^{(s)} \right) + r^{-2} \partial_\phi^2 u_z^{(s)} + \partial_{z'}^2 u_z^{(s)} \right) \tag{68}$$

where $u_z^{(s)} = u_z^{(s)}(t, r, \phi, z')$. In view of (67), oblate spheroidal coordinates are useful. For their definition, we refer to Spencer and Moon [22]. We need to solve the equations $R_0^2 = a^2 \cosh^2 \eta_0$ and $R_0^2 / \aleph^2 = a^2 \sinh^2 \eta_0$. This results in $a^2 = R_0^2 \left(1 - \aleph^{-2} \right) < R_0^2$ and $0 < \eta_0 = \text{arcoth}(\aleph)$. We then let

$$\eta \in \left(\eta_0 - \delta\eta/2, \eta_0 + \delta\eta/2 \right)$$

model the finite thickness of the membrane. This is needed because the Helmholtz operator cannot be restricted to the $\eta = \eta_0$ iso-surface in oblate spheroidal coordinates so that a solvable eigenvalue problem is maintained. This is in contrast to spherical coordinates where we can restrict them to the $r = R$ iso-surface.

The coordinate transform we aim at is established as $r = a \cosh \eta \sin \theta$ and

$z = a \sinh \eta \cos \theta$. The result is a Laplacian in oblate spheroidal coordinates [22]. Let Φ be a suitably function depending on the oblate spheroidal variables (η, θ, ϕ). The Laplacian $\Delta \Phi$ is then given by the expression

$$\Delta \Phi = \frac{1}{a^2 \left(\cosh^2 \eta - \sin^2 \theta \right)} \left(\frac{1}{\cosh \eta} \frac{\partial}{\partial \eta} \left(\cosh \eta \frac{\partial \Phi}{\partial \eta} \right) + \frac{1}{\sin \theta} \frac{\partial}{\partial \theta} \left(\sin \theta \frac{\partial \Phi}{\partial \theta} \right) \right)$$
$$+ \frac{1}{a^2 \left(\cosh^2 \eta - \sin^2 \theta \right)} \frac{\partial^2 \Phi}{\partial \phi^2}. \tag{69}$$

It is convenient to define $k_s^2 \equiv \rho_s \omega^2 / \mu_s$ for a stimulus of frequency ω. Quasi-stationarity permits the assumption that the shell oscillates with the same frequency. The resulting Helmholtz equation $\Delta u_s^{(z)} + k_s^2 u_s^{(z)} = 0$ will be separated in oblate spheroidal coordinates in the next paragraph.

Separation of the Helmholtz equation in oblate spheroidal coordinates

As a separation Ansatz, we take $u_z^{(s)} = O(\eta) P(\phi) A(\theta)$ with as yet to-be-determined functions O, P & A. Along the lines indicated elsewhere ([22], p. 36), the following equations result,

$$\frac{1}{\cosh \eta} \frac{d}{d\eta} \left(\cosh \eta \frac{dO}{d\eta} \right) + \left(k_s^2 a^2 \cosh^2 \eta - p(p+1) + \frac{q^2}{\cosh^2 \eta} \right) O(\eta) = 0, \tag{70}$$

$$\frac{1}{\sin \theta} \frac{d}{d\theta} \left(\sin \theta \frac{dA}{d\theta} \right) + \left(-k_s^2 a^2 \sin^2 \theta + p(p+1) - \frac{q^2}{\sin^2 \theta} \right) A(\theta) = 0, \tag{71}$$

$$\frac{d^2 P(\phi)}{d\phi^2} + q^2 P(\phi) = 0 \tag{72}$$

where $p > 0$ and $q > 0$ are separation parameters. They will be fixed during the discussion to follow. The thickness ($\approx d_s$) of the elastic shell in η-direction enters by noting that $\eta \in (\eta_0 - \delta\eta/2, \eta_0 + \delta\eta/2)$ has a small interval length. We force $O(\eta) = O(\eta_0) \neq 0$ to be a non-zero constant in the interval. This corresponds to requiring that the whole shell moves along its thickness in η-direction. At $\theta = \pi/2$, the η-average is consistent with the radial average performed to obtain Equation (64) and Equation (63). Physically, the average under consideration formalizes the requirement that only constant elastic deformations with respect to η occur. The equation (70) then gives rise to an equation for the separation parameter p,

$$k_s^2 a^2 \cosh^2 \eta - p(p+1) + \frac{q^2}{\cosh^2 \eta} = 0. \tag{73}$$

The above equation can be solved for p and the correct sign in front of the square root of the discriminant is fixed by the requirement $p > 0$. The result for p is then

$$p = p(q, \eta) = \frac{-1 + \sqrt{1 + 4 \left(\frac{k_s^2 a^2 \cosh^4 \eta + q^2}{\cosh^2 \eta} \right)}}{2}. \tag{74}$$

The function p depends on η and q in a well-behaved way. The dependence

upon η can actually be eliminated. The interval for η has a length $\delta\eta$ suitably small so that $\eta \approx \eta_0$ introduces a negligible error. The dependence upon q is fixed by investigating the polar part $P = P(\phi)$. The clamping of extracolumella needs to be accounted for as the piston mode of the shell plus extracolumella system has already been massaged into (64). The vibrations on the shell's surface follow from the compressional coupling conditions defined before in (64) & (63), where the shell had been excluded as immobile element. The clamping at $\phi \in \{\beta, 2\pi - \beta\}$ requires Dirichlet boundary conditions for (72):

$$P(\phi = \beta) = 0 = P(\phi = 2\pi - \beta),$$

which settles as a pair of $L^2\left(\left[\beta, 2\pi - \beta\right]\right)$-normalized solutions

$$\Phi_q(\phi) = \frac{\sin\left(q(m)(\phi - \beta)\right)}{\sqrt{\pi - \beta}}, \tag{75}$$

$$q(m) = \frac{m\pi}{2\pi - 2\beta}\left(m \in \mathbb{N}\right). \tag{76}$$

The q-dependence of the parameter p in (74) can be specified explicitly,

$$p(m) = \frac{-1 + \sqrt{1 + 4\left(\dfrac{\left(2\pi - 2\beta\right)^2 k_s^2 a^2 \cosh^4 \eta_0 + m^2\pi^2}{\left(2\pi - 2\beta\right)^2 \cosh^2 \eta_0}\right)}}{2}. \tag{77}$$

The obstruction for further analytic investigation is rooted in the solution of (71). Since the separation parameter p is constant with respect to θ, the azimuthal dependence of $u_z^{(s)}$ is contained in functions of the form

$$A_m(\theta) = A_m \mathrm{ps}_{p(m)}^{q(m)}\left(ik_s a, \cos\theta\right) + B_m \mathrm{qs}_{p(m)}^{q(m)}\left(ik_s a, \cos\theta\right). \tag{78}$$

The objects denoted by $\mathrm{ps}_{p(m)}^{q(m)}(i\lambda, x)$ and $\mathrm{qs}_{p(m)}^{q(m)}(i\lambda, x)$ are known as (azimuthal-) angular part of oblate spheroidal functions. No closed-form analytic representation is known [24]. Following the notation of Falloon, Abbott, and Wang [25] and taking $z, \mu, \gamma \in \mathbb{C}$, they are solutions of the following ordinary differential equation of Sturm-Liouville type,

$$\frac{\mathrm{d}}{\mathrm{d}z}\left(\left(1 - z^2\right)\frac{\mathrm{d}f}{\mathrm{d}z}\right) + \left(\lambda_\nu^\mu + \gamma^2\left(1 - z^2\right) - \frac{\mu^2}{1 - z^2}\right) = 0 \tag{79}$$

We refer to the literature [25] [26] [27] for a further treatment of spheroidal wave functions for non-integer parameters p and q. Here we restrict ourselves to noting that the general solution $u_z^{(s)}$ for the shell equation can be expressed as

$$
\begin{aligned}
&u_z^{(s)}(t, z, \phi) \\
&= \sum_{m=1}^{\infty} A_m \frac{\mathrm{ps}_{p(m)}^{q(m)}\left(i\omega\sqrt{\dfrac{\rho_s}{\mu_s}}R_0\sqrt{1 - \aleph^{-2}}, \dfrac{z}{R_0}\right)\sin\left(q(m)(\phi - \beta)\right)}{\sqrt{2\pi - 2\beta}}\exp(i\omega t) \\
&+ \sum_{m=1}^{\infty} B_m \frac{\mathrm{qs}_{p(m)}^{q(m)}\left(i\omega\sqrt{\dfrac{\rho_s}{\mu_s}}R_0\sqrt{1 - \aleph^{-2}}, \dfrac{z}{R_0}\right)\sin\left(q(m)(\phi - \beta)\right)}{\sqrt{2\pi - 2\beta}}\exp(i\omega t)
\end{aligned}
\tag{80}
$$

The quantity $\aleph$ is defined in (66), $q(m)$ is specified in (76) and $p(m)$ in (77) where $\eta_0 = \text{arcoth}\left(\sqrt{2 + \lambda_s/\mu_s}\right)$ is to be used in these equations. The two constants A_m and B_m for a polar mode of index $m \in \mathbb{N}$ are theoretically fixed by the boundary conditions (64) and (63) as well as by the requirement that the top of the shell does not vibrate after exclusion of the piston mode: $u(t, z = R_0, \phi) = 0$. As of 2017 [28], no stable computer algebra system seems to be available. As such, more than a specification of the general expression (80) is out of reach.

Elastic ring

Expressing the Laplacian Δ in (56) in cylindrical coordinates, a restriction to $r = R_0$, $u_z^{(r)}$ is the solution of the differential equation

$$\rho_r \partial_t^2 u_z^{(r)} = \left(\lambda_r + 2\mu_r\right) \partial_z^2 u_z^{(r)} + \mu_r R_0^{-2} \partial_\phi^2 u_z^{(r)}. \tag{81}$$

Quasi-stationarity is employed to factor out an $\exp(i\omega t)$ and thus convert the above wave equation to a Helmholtz equation. The method to re-scale the variable z that has been employed to convert (55) to (68) applies to (81) as well, with the obvious substitutions of Lamé constants. Let us define $k_r^2 = \omega^2 \rho_r / \mu_r$ and redefine $z = \aleph' z''$ where

$$\aleph' \equiv \sqrt{2 + \frac{\lambda_s}{\mu_s}} > 1. \tag{82}$$

At $z = -H$, we demand that the ring is clamped. The elastic ring is supposed to terminate by being "glued" into the bony structure of the animal's skull. In the variable z'', the clamping condition is imposed at $z' = H_0 \equiv \left(\aleph'\right)^{-1} H < H$. Because of the ring's axial symmetry, periodic boundary conditions are appropriate for the cylindrical angular variable. Then the $u_z^{(r)}$ solving (81) is of the form

$$u_z^{(r)}(t, \phi, z) = \sum_{m=-\infty}^{\infty} C_m \sin\left(\frac{\sqrt{k_s^2 - \frac{m^2}{R_0^2}}(z + H)}{\aleph'}\right) e^{im\phi} e^{i\omega t}. \tag{83}$$

For $m \in \mathbb{Z}$, C_m is a constant that can be found by insertion of (80) and (83) into the compressional boundary conditions (63) and (64). Together with the condition $u_z^{(s)}(t, z = R_0, \phi) = 0$, the constants in $\left\{(A_m, B_m) \mid m \in \mathbb{N}\right\}$ for the shell's displacement as given in (80) and $\left\{C_m \mid m \in \mathbb{Z}\right\}$ for the ring's displacement as given in (83) are the solutions to the inhomogeneous system of linear equations that would be defined by the boundary conditions—but:

Analytic investigations of the resulting equations are out of reach because of the lack of closed form expressions for the spheroidal wave functions ps and qs. Because of serious concerns over the reliability of numerical predictions even for integer-indexed spheroidal wave functions, a numerical treatment is ruled out. So we face the question: How can we still make a bit of progress?

Weak coupling assumption

We recall that amplitudes of the piston vibration of the shell have already been shown to be small compared to the vibration amplitude of the ring; cf. Equation (65). Furthermore, biological tissue consists, to a large fraction, of water. Under small external pressures, water is practically incompressible. Also the generation of excess-pressure contributions to the compressional boundary conditions (63) and (64) should be small. In view of the amplification factor $\mathfrak{a}$, we therefore assume that the compressional moduli K_r, K_s of ring and shell are sufficiently small so as to permit iteration of the boundary conditions (63) and (64), a weak coupling assumption.

That is, we assume $\left| K d_s \partial_z^2 u_z^{(r)} \right|, \left| K d_s \partial_z^2 u_z^{(s)} \right| \ll \mathfrak{a} p(t)$. The assumption corresponds to requiring that the elastic coupling in the two-spring model impacts the overall coupled vibration of shell and ring sub-dominantly as compared to the stimulus' impact. From a biological viewpoint, this behavior is reasonable because the tympanic structure shall respond predominantly only to the external stimulus p that an animal needs to detect. Furthermore, the similarity in material composition between water and biological tissue hints at the smallness of compressional effects compared in driving the membrane system as compared to the influence of the external pressure p. The boundary conditions (64) and (63) are the understood as differential equations defined on the joint boundary at $z = 0$ and finally subjected to a Picard-iteration. The iterated analogues of (64) and (63) read

$$
\begin{aligned}
&\sigma_s \partial_t^2 \left[u_z^{(s)} \right]^{(k+1)} (t, 0, \phi) \\
&= -\left(K_s d_s \right) \partial_z^2 \left[u_z^{(s)} \right]^{(k)} (t, 0, \phi) + \left(K_r d_s \right) \partial_z^2 \left[u_z^{(r)} \right]^{(k)} (t, 0, \phi),
\end{aligned}
\tag{84}
$$

$$
\begin{aligned}
&\sigma_r \partial_t^2 \left[u_z^{(r)} \right]^{(k+1)} (t, 0, \phi) \\
&= -\left(K_r d_s \right) \partial_z^2 \left[u_z^{(r)} \right]^{(k)} (t, 0, \phi) + \left(K_s d_s \right) \partial_z^2 \left[u_z^{(s)} \right]^{(k)} (t, 0, \phi) + \mathfrak{a} p(t)
\end{aligned}
\tag{85}
$$

at $z = 0$.

The iteration index k is a non-negative integer. As a starting value for the boundary conditions, we specialize to $\left[u_z^{(s)} \right]^{(-1)} = 0 = \left[u_z^{(s)} \right]^{(-1)}$. The fact that the external stimulus is the physical cause for the displacement of the tympanic structure underlies this choice of starting values.

For the 0-th iterate in (84), we find $\sigma_s \partial_t^2 \left[u_z^{(s)} \right]^{(0)} (t, \phi, z = 0) = 0$ for the shell, which is fulfilled, if $A_m = B_m = 0$ for all $m \in \mathbb{N}$ so that $u_s^{(z)} (t, \phi, z) = 0$. The result means that apart from the piston mode, which has already been translated into a contribution to the ring's displacement, the shell exhibits no vibrations. For the ring, (85) produces

$$
\sigma_s \partial_t^2 \left[u_z^{(r)} \right]^{(0)} (t, \phi, z = 0) = \mathfrak{a} p(t)
\tag{86}
$$

as 0-th iterate boundary condition. In the quasi-stationary state

$$
\left[u_z^{(r)} \right]^{(0)} \sim \exp(i\omega t),
$$

the above equation reduces to inhomogeneous Dirichlet boundary conditions,

viz.,

$$\left[u_z^{(r)}\right]^{(0)}(t,\phi,z=0) = \frac{-\mathfrak{a}p_0}{\rho_r d_s \omega^2}\exp(i\omega t). \qquad (87)$$

Since the homogeneous part of the boundary conditions in 0-th iteration is Dirichlet, the eigenfrequencies of the ring's vibration pattern in 0-th order can be obtained, following the standard procedure to solve Dirichlet eigenvalue problems, from the requirement $\sqrt{k_r^2 - m^2/R_0^2} = \aleph'\pi n/H$ in (83). This is equivalent to requiring that the z-dependent contribution to $u_z^{(r)}$ in (83) satisfies homogeneous Dirichlet boundary conditions, so that

$$\omega \equiv \omega_{nm} = \frac{\mu_r}{\rho_r}\frac{m^2}{R_0^2} + \frac{\lambda_r + 2\mu_r}{\rho_r}\frac{n^2\pi^2}{H^2} \qquad (88)$$

where $n \in \mathbb{N}$ and $m \in \mathbb{Z}$. It remains to solve (56) with 0-th order boundary condition (87) imposed instead of the full (64). The approximate boundary value problem gives rise to approximate solutions to (55) and (56) where, instead of the boundary conditions (64) and (63), the iterated boundary conditions (85) and (84) are used in 0-th order. In doing so, we assume that compressional effects of the membrane tissue is small compared to the external pressure drive.

Due to axial symmetry of the stimulus $\mathfrak{a}p = \mathfrak{a}p(t)$, only the $m=0$-mode in (83) contributes. Consequently, the 0-th iterate solution reads

$$u_z^{(r)}(t,z,\phi) = -\frac{R_0 p_0 e^{i\omega t}}{2\rho_r d_s^2 \omega^2}\frac{\sin\left(\sqrt{\frac{\mu_r}{\lambda_r + 2\mu_r}}\sqrt{\frac{\rho_r\omega^2 R_0^2 - \mu_r m^2}{\mu_r R_0^2}}(z+H)\right)}{\sin\left(\sqrt{\frac{\mu_r}{\lambda_r + 2\mu_r}}\sqrt{\frac{\rho_r\omega^2 R_0^2 - \mu_r m^2}{\mu_r R_0^2}}H\right)}, \qquad (89)$$

where $\mathfrak{a} = R_0/2d_s$ has been reinstalled.

Implications for the iteration parameter of the two-spring model

The absence of tools to generate reliable numerical predictions for the coupled motion of shell and ring led to the creation of the two-spring model as an effective theory in which the compressional coupling has been stored in the fit constant k_0. One possible approach to obtain insights in the strength is by noting $k_0/k_r \sim K_r/(\lambda_r + 2\mu_r)$ in view of the solution (89). Under the additional assumption that the shell vibration supports an analogous sinusoidal behavior as in (89), an analogous estimate results: $k_0/k_s \sim K_s/(\lambda_s + 2\mu_s)$. In terms of elastic parameters

$$\frac{k_0}{k_r} \sim \frac{E_r(1+v_r)}{3E_r(1-v_r)} = \frac{1}{3}\frac{1+v_r}{1-v_r}, \qquad (90)$$

$$\frac{k_0}{k_s} \sim \frac{E_s(1+v_s)}{3E_s(1-v_s)} = \frac{1}{3}\frac{1+v_s}{1-v_s}. \qquad (91)$$

Since for most materials $0 \le v_r, v_s \le 0.5$, the assumption $k_0/k_r, k_0/k_s \lesssim 1$ seems quite reasonable.

Fluctuations Hypothesize the New Explanation of Meridians in Living Systems

Gyula Peter Szigeti[1], Andras Szasz[2]

[1]Institute of Human Physiology and Clinical Experimental Research, Semmelweis University, Budapest, Hungary
[2]Department of Biotechnics, St. Istvan University, Budaors, Hungary
Email: biotech@gek.szie.hu, szigeti.gyulapeter@gmail.com

Abstract

Biosystems are complex. Their physiology is well-controlled with various negative feedback signals and processes, it describes by opposite interfering effects which are characterized in the Eastern philosophy by Yin-Yang (Y-Y) pairs. Y-Y pairs could be described by the promoter-suppressor pairs in a wide range of physiologic signals creating the homeostasis of the complex system. This type of control appears as fluctuations from the average (mean) value of the signal. The mean carries an ineluctable fluctuation (called pink-noise or $1/f$ noise). All signals in homeostasis have equal entropy ($S_E = 1.8$), which is the character of the complex equilibrium. The various controlling opposite signals (Y-Y) have different time-scales which change by aging. The processes with smaller time-scale are degraded by aging, but the pink-noise ensures that the deviations of the signals of the healthy homeostatic system remain constant. Meridians are connected to the general transport systems that combined the material and the information transport with the considerable transport networks, like blood, lymph, nerve, cell-junctions, mesenchymal "ground substance" cytoskeletons. The meridians in this meaning only virtual line averaged from multiple realized paths to connect two acupuncture points by the material, energy and information transport processes. The meridian network is designed by various coupling points (acupoints), which could be perturbed by actuating stimulus. Our objective is to describe the meridian system from complexity point of view.

Keywords

Pink-Noise, Complexity, Living System, Meridians, Acupoints, Homeostasis

1. Introduction

There are numerous questions related to Traditional Chinese Medicine (TCM),

especially to acupuncture and the existence of meridians [1]. Is it an ancient cure or modern therapy? Is it art (psychology) or a treatment (physiology)? Is it a natural philosophy or an experimental medical practice? Answers are not formed yet [2].

When the importance of the dissipative processes was recognized, and the general system theory was established [3], we started to examine living systems differently from before [4]. It was discovered how environmental impact affected living systems and we started to examine the complexity of life. We understood the problem of complexity in physiologic processes and had more and more complications to explain the interference of the signals while studying the complete system as one. We face difficult challenges to examine individual physiologic changes in isolation from the body; but discovered specific general mechanisms (universalities) which do not depend on the details of the system with the same scales through few orders of magnitudes in spatiotemporal descriptions. The hallmarks of complexity give us new insights into the description and understanding of the general integrity of living objects. Non-stationarity (time-dynamics), non-linearity (cross-talks of signals, complicated interactions), multiscale organization (spatiotemporal fractal behavior), time irreversibility (non-equilibrium dynamics and fluctuations) are all giving surprising news when studying living objects. Non-equilibrium thermodynamics started to be connected to explanations and the equilibrium became a dynamic fluctuation with unique noises.

The dialectic dynamics of life had connections to philosophy (from Lao-Zi through Heraclitus of Ephesus to Hegel GWF), understanding the strict negative feedback connections by the thesis ↔ antithesis ↔ synthesis triad.

The ancient knowledge was based on long-term and much extended observations and experimental trials which of course were mixed with the ancient beliefs, philosophy and explanation of the environmental structures. In this paper, we would like to show some consequences of the complex physiology, some hypothesized effects which could explain the existence of acupoints and meridians without using any formulation or philosophical points from the ancient explanations.

2. Method

Multiple solutions were developed for the calculation of entropy of the data-row with finite length (like a representative sampling of physiological signals). These solutions are coherent with Shannon's entropy formulation. The Richman-Moorman entropy [5] was applied to the analysis of multiscale entropy (MSE) of physiological signals [6].

Following the calculation of [6], let us denote a time-series containing N samples by $\{X_l\} = \{X_1, \cdots, X_l, \cdots, X_N\}$. Choose from this vector with m-dimension:

$$u_m(i) = \{x_i, x_{i+1}, \cdots, x_{i+m-1}\}, \quad 1 \le i \le N-m+1 \tag{1}$$

We use the maximum of the absolute deviation of components to characterize

the distances between the vectors, so

$$d\left[u_m(i), u_m(j)\right] = \max\left[\left|x(i+k) - x(j+k)\right|\right], \quad 0 \le k \le m-1 \qquad (2)$$

The $u_m(i)$ and $u_m(j)$ vectors are r-neighbors when their distance is less than r. The negative logarithm of that conditional probability when the vectors remain r-neighbors is when an additional sampling is given to the time-series increasing, the length of the vectors too. Consequently, by applying this definition, Richman-Moorman-entropy is:

$$S_E = -\ln P\left(\left|x_i - x_j\right| \le r, \left|x_{i-1} - x_{j-1}\right| \le r\right) \qquad (3)$$

where S_E is the Richman-Moorman-entropy. Denote $n_i^m(r)$, the number of $u_m(j)$ $(i \ne j)$ vectors which have a distance from the vector $u_m(i)$ is smaller than r. The probability that the vector $u_m(j)$ is located in the distance of r-radius from a vector $u_m(i)$ is:

$$P_i^m(r) = \frac{n_i^m(r)}{N - m + 1} \qquad (4)$$

where the $P_i^m(r)$ is the probability of the distance of $u_m(j)$ form $u_m(i)$ is smaller than r; while the probability that the vector $u_{m+1}(j)$ is found in the r-radius neighborhood of $u_{m+1}(i)$ is:

$$P_i^{m+1}(r) = \frac{n_i^{m+1}(r)}{N - m + 2} \qquad (5)$$

The conditional probability from these would be:

$$\frac{P_i^m(r)}{P_i^{m+1}(r)} \cong \frac{n_i^m(r)}{n_i^{m+1}(r)} \qquad (6)$$

with these notations the Richman-Moorman-entropy could be interpreted in this form:

$$S_E = -\ln \frac{P_i^m(r)}{P_i^{m+1}(r)} \cong -\ln \frac{n_i^m(r)}{n_i^{m+1}(r)} \qquad (7)$$

The $n_i^m(r)$ and $n_i^{m+1}(r)$ values could be determined to know the probability density function. We may suppose that Gaussian pink noise [6] is allowed by the central limit theorem in physiological signals [7]. To characterize the multidimensional Gaussian distribution, the covariance matrix must be given too. The power-spectrum defines the covariance matrix, and from that the entropy could be derived.

The definition of the covariance matrix containing N-number of random variables:

$$\overline{\overline{C}}\left(X_i, X_j\right) := E\left[\left(X_i - \overline{X}_i\right)\left(X_j - \overline{X}_j\right)\right] \qquad (8)$$

The diagonal of the covariance matrix represents the deviations of the individual random variables. Due to the symmetry and real-elements of the hermitic matrix it could be transformed to the principal axis. The eigenvalues for this transformation:

$$\overline{\overline{C}}\,\overline{U}_i = \lambda_i \overline{U}_i \tag{9}$$

Therefore:

$$\overline{U}_j \overline{\overline{C}}\,\overline{U}_i = \lambda_i \overline{U}_j \overline{U}_i = \lambda_i \delta_{ij} \tag{10}$$

Consequently, when we form a $\overline{U}$ matrix from the eigenvectors like its columns, then:

$$\overline{\overline{U}}^{\mathrm{T}} \overline{\overline{C}}\,\overline{\overline{U}} = diag\left(\lambda_1, \cdots, \lambda_i, \cdots, \lambda_N\right) = \overline{\overline{\Lambda}} \tag{11}$$

is a diagonal matrix. The covariance matrix transformed random variable is:

$$\overline{Y} = \overline{\overline{U}}^{\mathrm{T}} \overline{X} \tag{12}$$

because

$$\begin{aligned}
\overline{\overline{U}}^{\mathrm{T}} \overline{\overline{C}}\,\overline{\overline{U}} &= \overline{\overline{U}}^{\mathrm{T}} E\left[\left(\overline{X} - \overline{\overline{X}}\right)\left(\overline{X} - \overline{\overline{X}}\right)^{\mathrm{T}}\right]\overline{\overline{U}} \\
&= E\left[\overline{\overline{U}}^{\mathrm{T}}\left(\overline{X} - \overline{\overline{X}}\right)\left(\overline{X} - \overline{\overline{X}}\right)^{\mathrm{T}}\overline{\overline{U}}\right] \\
&= E\left[\left(\overline{\overline{U}}^{\mathrm{T}}\overline{X} - \overline{\overline{U}}^{\mathrm{T}}\overline{\overline{X}}\right)\left(\overline{X}^{\mathrm{T}}\overline{\overline{U}} - \overline{\overline{X}}^{\mathrm{T}}\overline{\overline{U}}\right)\right] \\
&= E\left[\left(\overline{\overline{U}}^{\mathrm{T}}\overline{X} - \overline{\overline{U}}^{\mathrm{T}}\overline{\overline{X}}\right)\left(\overline{\overline{U}}^{\mathrm{T}}\overline{X} - \overline{\overline{U}}^{\mathrm{T}}\overline{\overline{X}}\right)^{\mathrm{T}}\right] \\
&= E\left[\left(\overline{Y} - \overline{\overline{Y}}\right)\left(\overline{Y} - \overline{\overline{Y}}\right)^{\mathrm{T}}\right]
\end{aligned} \tag{13}$$

Consequently, the deviation of the transformed random variable Y_j is:

$$\sigma_j' = \sqrt{\lambda_j} \tag{14}$$

On the other hand, the probability density function of an N-dimensional Gaussian noise is:

$$p\left(\overline{X}\right) = \frac{1}{\sqrt{(2\pi)^N \det \overline{\overline{C}}}} e^{\left[-\frac{1}{2}\left(\overline{X} - \overline{\overline{X}}\right)\overline{\overline{C}}^{-1}\left(\overline{X} - \overline{\overline{X}}\right)\right]} \tag{15}$$

Moreover, from this the distribution function of the transformed random variable is:

$$\begin{aligned}
p\left(\overline{Y}\right) &= \frac{1}{\sqrt{(2\pi)^N \det \overline{\overline{\Lambda}}}} e^{\left[-\frac{1}{2}\left(\overline{Y} - \overline{\overline{Y}}\right)\overline{\overline{\Lambda}}^{-1}\left(\overline{Y} - \overline{\overline{Y}}\right)\right]} \\
&= \prod_{i=1}^{N} \frac{1}{\sqrt{2\pi\lambda_i}} e^{-\frac{\left(Y_i - \overline{Y}_i\right)^2}{2\lambda_i}} = \prod_{i=1}^{N} p\left(Y_i\right)
\end{aligned} \tag{16}$$

$$p\left(Y_i\right) = \frac{1}{\sqrt{2\pi\lambda_i}} e^{-\frac{\left(Y_i - \overline{Y}_i\right)^2}{2\lambda_i}}$$

To calculate the covariance matrix starting from the power-density of the pink-noise:

$$S\left(\omega\right) = \begin{cases} \dfrac{K}{\omega}, & \omega_1 \le \omega \le \omega_2 \\ 0, & \text{otherweise} \end{cases} \tag{17}$$

The autocorrelation function could be determined from this by the Wiener-Khinchin-theorem [8]:

$$\Phi(\tau) = \frac{K}{2\pi} \int_{\omega_1}^{\omega_2} \frac{\cos \omega \tau}{|\omega|} d\omega = \frac{K}{2\pi} \left[Ci(\omega_2 \tau) - Ci(\omega_1 \tau) \right],$$

$$Ci(\tau) = \gamma + \ln(\tau) + \sum_{k=1}^{\infty} \frac{(-1)^k \tau^{2k}}{(2k)! 2k} \tag{18}$$

where $Ci(\tau)$ is the function of integral-cosine, and $\gamma = 0.5772$ is the Euler's constant. Consequently:

$$\Phi(\tau) = \frac{K}{2\pi} \left\{ \ln \frac{\omega_2 \tau}{\omega_1 \tau} + \sum_{k=1}^{\infty} \frac{(-1)^k}{(2k)! 2k} \left[(\omega_2 \tau)^{2k} - (\omega_1 \tau)^{2k} \right] \right\} \tag{19}$$

3. Results

The connection of the autocorrelation function and covariance matrix for such ergodic processes like the pink-noise is 6:

$$\overline{\overline{C}} = \begin{bmatrix} \Phi(0) & \Phi(\tau) & \Phi(2\tau) & \cdots & \Phi(N\tau) \\ \Phi(\tau) & \Phi(0) & \Phi(\tau) & \cdots & \Phi((N-1)\tau) \\ \Phi(2\tau) & \Phi(\tau) & \Phi(0) & \cdots & \Phi((N-2)\tau) \\ \vdots & \vdots & \vdots & \ddots & \vdots \\ \Phi(N\tau) & \Phi((N-1)\tau) & \Phi((N-2)\tau) & \cdots & \Phi(0) \end{bmatrix} \tag{20}$$

with these conditions the MSE entropy of pink-noise [6]:

$$S_E = 1.8 \tag{21}$$

To determine the homeostatic equilibrium, we make a multi-scale entropy analysis, where the $\{x_1, \cdots, x_l, \cdots, x_N\}$ is a one-dimensional discrete time-series. From this, a consecutive coarse-grained $\left\{ y_r^{(\tau)} \right\}$ time-series can be constructed with τ scale-factor, as shown in **Figure 1**.

According to **Figure 1**, the members of the τ scale series are:

$$y_j^{(\tau)} = \frac{1}{\tau} \sum_{i=(j-1)\tau+1}^{j\tau} x_i, \quad 1 \leq j \leq N/\tau \tag{22}$$
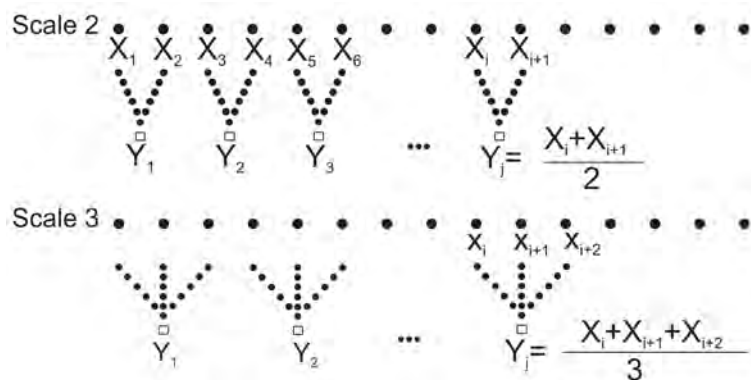
Figure 1. Illustration of the coarse-graining process in the 2nd and 3rd scale (after [9]).

MSE method is used to calculate the entropy of all the coarse-grained time-series. This was made for pink and white noises 6, and the results are shown in **Figure 2**. (The scale-factor is the number of terms in the average.) The $1/f$ noise does not change by the smoothing (cutting of high frequencies) of the function, and the Rich-man-Moorman entropy of pink-noise is scale-independent in a definite interval, it is constant and could characterize the homeostasis. The results are in perfect harmony with the others obtained by the other methods [10] [11], and applied to living systems [12].

The correlation of the white noise is small, so the entropy of the white noise decreases by series of higher time-factors, while in case of the pink noise the complex internal structure remains constant on the large time-scales due to its long correlation length. The short correlation length of the white noise causes high entropy on the small scales (<4), while the weaker correlation for long-scale ensures the constant entropy for pink noise in the wide range of scales.

4. Discussion

From a physical point of view, the scaling of discrete time series is a filtering process of some of the high-frequency components of the noise. We may construct a series of scales by bandwidths. The highest bandwidth is at the 1st scale, and by averaging more and more high-frequency components, higher scales have gradually narrower band-gaps. The highest frequency in the signal is well approximated by Shannon's sampling theorem [13], declaring that the highest frequency in the sampled noise is the half of the sampled frequency. Consequently, in the scale of the 2nd factor, the upper frequency is half of the half of sampled frequency, in the nth the nth-part of the bandwidth, and a similar one is valid on the low-frequency limit as well. The length of the data-series characterizes the time-length of the registering of the noise; when the sampling time is ΔT, and N is the size of the data-series then the length of the registration is $N\Delta T$. The reciprocal value of $N\Delta T$ is the smallest frequency in the sampled signal, so is the low limit of the bandwidth. Due to the decreasing length of the data series the low-frequency limit of the bandwidth grows. The scaling of the power-function $S(\omega)$ is shown in **Figure 3**.
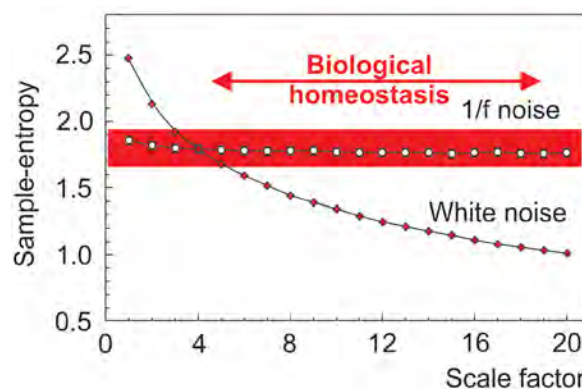
Figure 2. The result of MSE analysis of pink and white noises [6].
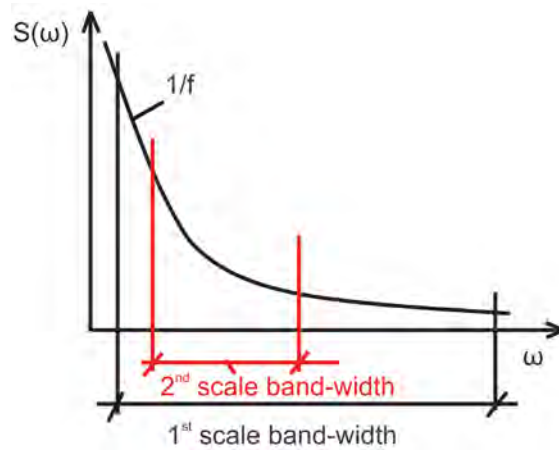
Figure 3. The shortening of bandwidth in the scaling, using the Shannon's sampling theorem. The upper limit is cutting the half of the maximal sampling frequency, while the lower limit is the double of the minimal sampling frequency. This process is continued to the 3rd, 4th, etc. scaling steps, using the *n*-th bandwidth determining the (*n* + 1)-th by the same procedure.

In this meaning, the Richman-Moorman-entropy of time-series shows some kind of a holographic behavior of the pink-noise, namely the entropy does not change by the truncating of the registering of the pink-noise.

The Richman-Moorman-entropy has a natural physical meaning too, (like the Shannon entropy also [14]), from its multiplication with Boltzmann constant ($k_B \approx 1.38 \times 10^{-23}$ [$m^2 \cdot kgs^{-2} \cdot K^{-1}$]) we get the physical entropy of the sample. We know from thermodynamics that the entropy is a function of the state of a system, so it is a function of the state-variables, like the internal decisional energy. The internal energy in our case is the sum of the energy content of the Fourier components. Consequently, the physical entropy of the signals from pink-noise does not change by decreasing its energy, similarly to the thermodynamical entropy that has extremum in the function of energy. This allows energy exchange between the sub-systems in the thermodynamic equilibrium in the form of fluctuations without its entropy changing.

A similar attribute could exist in case of stochastic processes when a system emits pink-noise. Subsystems could change energy without changing their entropy in this fluctuation analogy. However, in this case, the entropy is not extensive. The energy is an additive magnitude but the entropy, which is constant in the homeostasis, is not an additive parameter. Consequently, on the grounds of experience, the entropy is intensive in systems of homeostasis.

In the realization of homeostasis of a living system the "ground substance", which is a considerable part of the whole weight of the system, [15], has a central role. This ground state is a gel-like mesenchymal tissue, a soft connection material. The basic information transport goes through this connective tissue, which structure contains a large amount of the extracellular matrix too. The mesenchyme ensures the alimentation and excretion of cells, it is a transmitter and filter between the capillaries and cells containing highly polymerized carbo-

hydrates glucosaminoglycans, protein associated ologasacharid chains, proteoglycans and structural glycoproteins, glycolipids in the ordered set, networked with dendrites and extracellular matrix of glycocalyx. The mesenchyme is active in three communication levels on the regulation of the system: cellular, humoral and nervous. The cellular level ensures the chemical equilibrium of the connective tissue with the system of reticuloendothelial cells. It locally controls the capillary transported materials, like oxygen, metabolites and enzymes cell-life signals. Through the humoral transports, it communicates over a long distance with subsystems by electrolyte transports (lymph, blood-stream). The nervous network functionally connects the distant parts of the system. The humoral level of systemic transport processes is slow, while the nervous communications are transported fast. All the controls have negative feedback regulating the equilibrium with action signal-pairs promoting or suppressing the actual process. We could note the balancing signal pairs as Y-Y pairs taking the notation from Ying-Yang introduced by Traditional Chinese Medicine (TCM). This feedback mechanism is the smart solution to fixing the actual expected values. A simple example for the negative feedback control in non-living systems is the weight hanging on a spring. Gravitation attracts the weight in the direction of the Earth-center, while the spring suppresses the gravitation, always works against it with the same force as gravitation acts and forms equilibrium position somewhere. During any external perturbation, the opposite effects compensate the deviations, and the weight is in its equilibrium place in the time-average. In the physiological signals, a large number of controlling pairs form the average value (equilibrium value) of the physiological signal. All the three action levels are connected in the mesenchyme; which gives "stage" to form an equilibrium.

The controlled parameters of the regulation system of homeostasis (like the actual value of a physiological signal) are realized with dialectic determination. This means that the controlled value of the physiological process is formed by the dynamical equilibrium of a large number of interfering controlling signal pairs (Y-Y). Let us study the proliferation homeostasis to elucidate this process. The essence of proliferation homeostasis is the exchange of the old or damaged to new ones, fixing the size of the organs and parts of the system. The two acting opposite regulation signals (Y-Y) generate the annihilation (Yin) and creation (Yang). Programmed cell death (apoptosis) is on the Yin side while cellular division generated by the growth-factors has a leading role on the Yang side. The healthy arrangement is a dynamic equilibrium turning to disease when it comes apart. When the Yin is dominant, apoptosis overrides the situation and an autoimmune disease is formed. In case the Yang is the dominant, creation has a central role; tumorous diseases are shaped by switching-off of the programmed cell death. The complete accommodation of the system is better when it has more Y-Y pairs which interact and form subsystems too. The homeostatic equilibrium stabilizes the energy-intake of the subsystem and the whole system as well which is described by the allometry of the living systems [16].

Their board equilibrium governs multiple other effects. The Y-Y pairs could interfere with the same proliferation process controlling hypoxia or many other factors in the microenvironment of the cell by coupling like the humoral control. When oxygen delivery is not satisfactory (hypoxia, Yin-dominance), as it can happen at an excessive muscle activity, blood-perfusion becomes more active to compensate with increased permeability of the vessel walls, or even angiogenesis can begin (Yang-effects). In case of a further load (like regular sport activity) protocol enzymes will solute the extracellular matrix helping the mobility of the cells, and due to the effect of vascular endothelial growth factor (VEGF) they will start a higher proliferation activity and chemomechanical migration by the gradient of VEGF, building up a primitive blood-vessel network. The network is controlled by not only VEGF but the gradient of electric potential like a morphogenetic factor [17]. Potential gradient is formed by the more negative newborn daughter cells rather than by the matured neighbors (**Figure 4**).

The 4th period of angiogenesis is the maturation when the extracellular matrix is fixed; the appropriate cells are coupled and form the vessel-wall; angiopoietins complete the existing capillary network with the new one and make the vessel-system ready for proper physiological operation. Angiogenesis itself is not enough, the direction of the forming vessel is also important which is governed by the potential gradient. The final stage of angiogenesis is the optimizing stage, when the dialectic determination of Y-Y recovers its dynamic equilibrium from the alimentation point of view.

The above regulation process is rather simplified but shows a very complex adjustment of the parameters and is only one of the large number of cooperation processes forming homeostatic control. This must not be deterministic, because neither the appropriate accuracy nor the adequate stability could be ensured with quick signal-exchange. The non-deterministic process emphasizes the accidental processes determining the homeostasis on the way when the regulation is flexible and "economic", therefore it is no more accurate than it is necessary for the actual function.
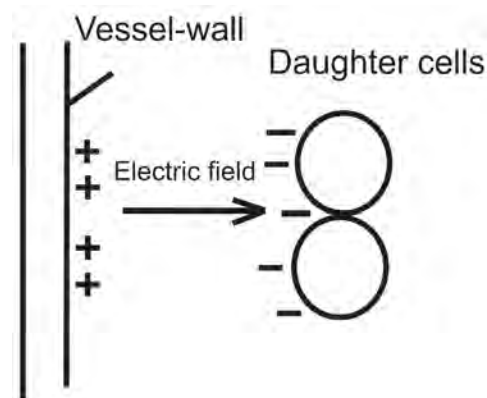
Figure 4. The forming of electric potential at angiogenesis. The electric field is an effector of the epithelial transition producing cellular joints and cytoskeletal polymerization [17].

The optimal accuracy governed by the goals of homeostasis is to provide constant environmental conditions for the living cells and their collective development. These requests are keeping the parameters within tolerance limit without the environmental conditions remaining for a longer period, assuring the mean and the deviation of a constant value. The constant mean allows fluctuations, noises when their deviation remains under the predefined limits.

We would like to show that the time-fractal fluctuation is a perfect error-signal satisfying the homeostatic requirements. We consider the mean $(\langle x(t)\rangle)$ of the n number of $x_i(t)$ signals in time t in the homeostatic controlled environment as basic signal:

$$\langle x(t)\rangle = \frac{1}{n}\sum_{i=1}^{n} x_i(t) \tag{23}$$

where the sign $\langle \ \rangle$ denotes the averaging in time. The error is the deviation from this mean, so the controlling error is the noise due to the accidental processes in the homeostatic regulation, **Figure 5**.

The noise $(z(t))$ is the deviation of the actual signal $(x(t))$ from the mean $\langle x(t)\rangle$:

$$z(t) = x(t) - \langle x(t)\rangle \tag{24}$$

Let us study the $\langle z^2(t)\rangle$ variance (square of the standard deviation) of the $x(t)$ as a function of time:

$$\langle z^2(t)\rangle = f(t) \tag{25}$$

Due to the self-similarity of the biological processes [18], the deviation of the signal must be a power function:

$$\langle z^2(t)\rangle = t^{H'} \tag{26}$$

where $H > 0$ in every case. When $H = 1$ the $\langle z^2(t)\rangle$ of the controlling error is a linear function of the time:

$$\langle z^2(t)\rangle = ct \tag{27}$$

where c is a constant. Form (26) we obtain the scaling conditions:

$$\langle z^2(rt)\rangle = r^{H'}\langle z^2(t)\rangle \tag{28}$$
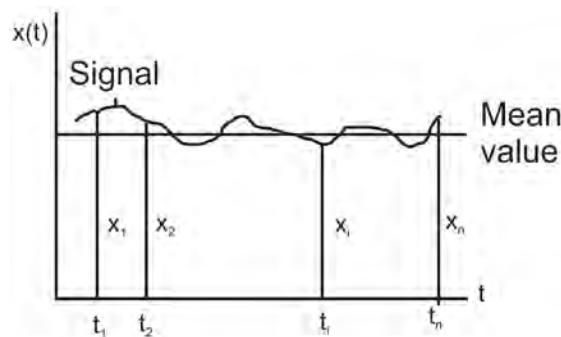
Figure 5. The noise around the mean value of a signal.

The error-signal could be characterized by its spectral power-density ($S(f)$) [19] too:

$$S(f) = F\left[G(\Delta t)\right] \qquad (29)$$

where $G(\Delta t)$ is the autocorrelation function [20] of the error-signal:

$$G(\Delta t) = \left\langle z(t)z(t+\Delta t)\right\rangle - \left\langle z(t)^2\right\rangle \qquad (30)$$

The power density of the noises like (28), is [21]:

$$S(f) \propto \frac{1}{f^{H'+1}} \qquad (31)$$

If the error signal is a pink ($1/f$) noise, then $H' = 0$. Considering (28), when the signal is pink-noise, the deviation does not depend on any r-value, so the deviation is constant in time. Consequently, there are definite limits which are never taken over by the error signal; because based on the Chebyshev inequality [22] the probability that the signal is in an interval $\left(\overline{x} - k\sigma, \overline{x} + k\sigma\right)$ is:

$$P\left(\left|x - \overline{x}\right| < k\sigma\right) > 1 - \frac{1}{k^2} \qquad (32)$$

Therefore, when k is appropriately large for the tolerance, the signal is practically always in the requested interval.

If the power-spectrum of the error-signal is not pink-noise, its exponent is larger than [11], then according to (28), the error-signal will be increased by time and the homeostatic equilibrium will be overset. This is a failure of the balancing, it leads to a jumble of control forming irregular processes, developing the disease. The character of the noise changes, it becomes "colored noise", having $H' > 0$ in (31).

The above discussion proves the fact that the physiologic signals have a pink-noise deviation from their averages keeping the limits of the homeostatic control, which in thermodynamical meaning keeps the sample entropy constant in a broad scale, $S_E = 1.8$. The famous quotation formulates this dynamic request by A. Einstein: "Life is like riding a bicycle. To keep your balance, you must keep moving.", [23]. Showing it in a simple sketch, representing the instability with a double-well potential, life is somewhere at the breaking point: it has no excess energy to lose but has enough energy to not be trapped in one fixed position, so it is always fluctuating at the breaking-point, energy means the E_{breaking}, and the fluctuation is time-fractal ($1/f$ pink noise). Energy keeps the system in this point pumped from the environment, Figure 6.

Life is on the edge of chaos, [24], as the quote from A. Szentgyorgyi, a Nobel laureate said: "Life is nothing but an electron looking for a place to rest.", [25].

The complex properties emphasize the request for change of paradigm of physiological evaluation, [26]. The problem is that in most of the medical diagnostics organ function is examined by its own structural or functional failure, and sometimes connects with a network view. However, even networking is not enough to get the realistic picture; a complex fractal view is necessarily taking
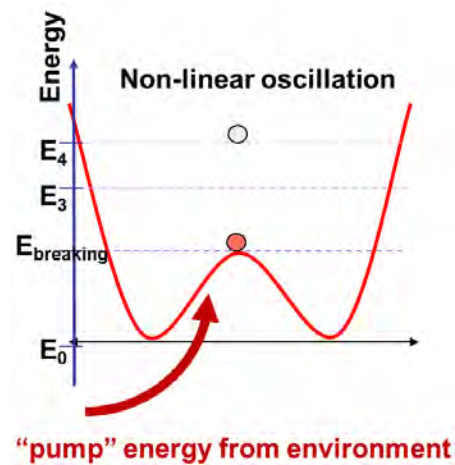
Figure 6. When the incoming energy is too high, the electron occupies a high energy level (noted by E_4 in the figure), which does not fit the homeostatic equilibrium. The electron start loosing its energy, and reaches the breaking point ($E_{breaking}$). When it looses too much energy, it will be "frozen" in one energy-well, which is again out from the homeostatic regulation. Consequently, energy keeps the electron in a "frustrated" position, at "edge of chaos" to fulfill the homeostatic equilibrium. The energy-fluctuations in this position are parts of the $1/f$-noise.

self-organized structural and dynamical (time) fractal behavior of the system into account. The mean of the physiological values does not give enough information; even its deviation could be unsatisfactory to compose a realistic diagnosis. Pink noise decides about the homeostatic equilibrium, so noise structure carries important information about the actual status of the living system.

We have to note that healthy, the healthy cell-division is also governed by fractal noise, [27]. It is shown that the relative error in the generation of the cells rapidly grows in a classical (non-fractal) model, while it remains constant (almost errorless) in case of pink-noise [28].

Aging decreases the complexity of the system, the dialectic formation of the Y-Y pairs degrades. On this way the Y-Y pairs act different time-scales, and the high frequencies gradually vanish in the noise. Consequently, aging has MSE scaling, the system develops higher scaling factors, but during the aging the entropy of physiologic signals does not change, it remains constant when the system is healthy. Thus, healthy aging is well distinguished from the disease on the level of homeostatic control, the deviation from the Y-Y determination is a character of the disease only.

The meridians are introduced by TCM to visualize the channels where the Y-Y pair acts. It is of course, a considerable simplification of the actual homeostatic balance due to the large number of active networks in the system (blood-, lymph-, nerve-networks completed with cell-junctions, cellular adherent connections, cytoskeletons, mesenchymal tissue, soft connective tissue, polymer-formations, etc.). These are interconnected and act in promoter suppressor (Y-Y) balancing as regulators. This is a controlling negative feedback loop from the initial product to the final one by interaction promoters and suppressors,

Figure 7.

The regulation network of the homeostasis is complex, having various levels of Y-Y actions, which are genuinely in interaction grouping and making new sets of actions on all levels of complexity, **Figure 8**.

This massive regrouping over the complete system has a well-defined regulation network based on the same negative feedback principles as the details of where this huge complexity built up, **Figure 9**. Life is developed as an open system, its exchange with the environment with materials, energy and other parameters essentially keep life stable. The openness is completed with energy dissipation [29], limiting the efficacy according to the entropy law of thermodynamics [30]. Of course, the inputs are noisy, as well as the outputs and all the feedback mechanisms have specific homeostatic noises as it is discussed above. The stability of this regulation is based on the constant dissipation in the open living system in a very broad scaling measured by MSE entropy ($S_E = 1.8$) keeping the entropy in the $1/f$ noise range in a very broad scaling interval.

There is a further crucial structural point of the complete organizing process. The feedback mechanisms are connected to the actual "hardcovers", so are the large networks (blood, lymph, nerve, junctions, adherents, mesenchyme, polymers, etc.). This hardware carries the "software", the regulation mechanisms, like the internet, a global network of interconnected computers, the world-wide-web (WWW), and information exchange place is based on the internet as "hardware". While WWW builds up a fractal structure, the internet does not [31]. The internet hardware has "hubs", which attract each other by the better communication possibilities guided by the economic optimizing. These systems are vulnerable due to the strong and large number of links in hubs forming strong characteristically assortative clusters. The WWW follows the user's optimization having a wide range of "weak links" meaning the connection of users outside the hub; weakens the connections to the hubs. These weak-links connect hubs with non-hubs, they make repulsion-like structures between hubs, and stabilize the system well; thus they are less vulnerable than the internet "hardware".

Figure 7. The balance of promoters and suppressors (Y-Y pairs) make an interaction negative feedback loop regulating each other, keeping the final product controlled.
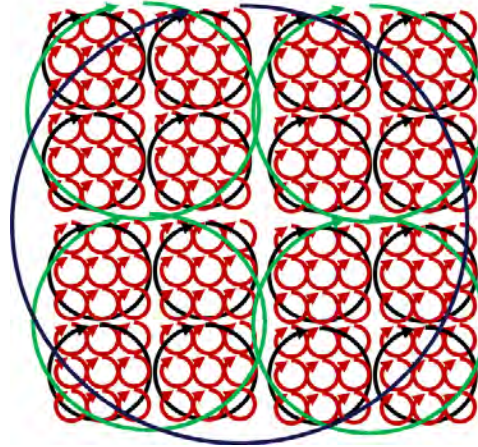
Figure 8. The regulation Y-Y loops are grouped, forming new regulation levels, and re-grouping again and so on subsequently.
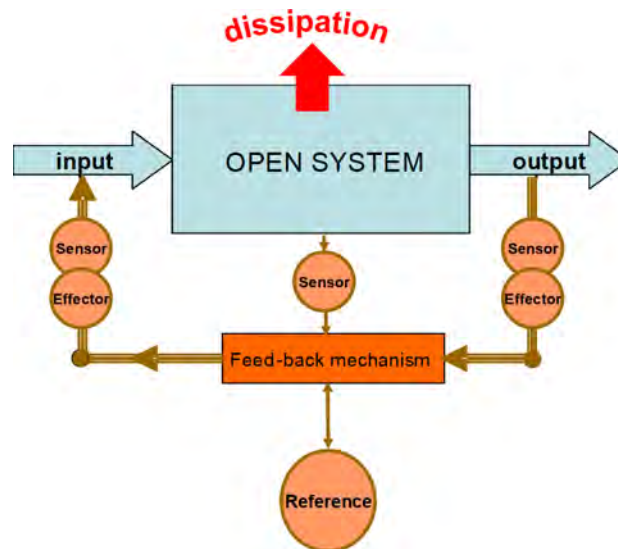
Figure 9. The complexity after all looks like one single Y-Y interaction which is regarded in TCM as the unified negative feedback Yin-Yang balance. It is a well-known negative feedback regulating principle in engineering, including dissipation due to the open system.

Living objects are built in the same way, **Figure 10**. The metabolic networks, the neural information exchange, the long-range correlated structures of information exchange in the living organisms work on WWW style (WS), while the large hubs as organs of the body structure are internet-like (IL). The information short-cuts (small-worlds [32]) optimize the integration of the systems as shown in the functional brain networks [33].

Meridians are probably structures that partly include large networks ("hardware", like blood, lymph, nerve), but also contain "software" components for communication between the organs ("hubs") and having intermediate points (probably the acupoints), on which we may modify the broken homeostatic equilibrium. Since the "ground substance" is the central place of the information
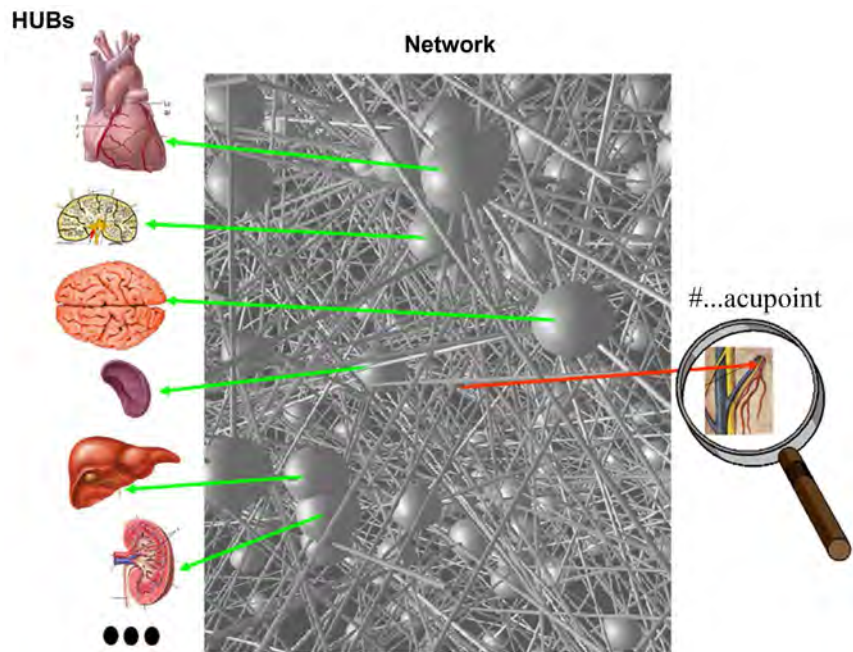
Figure 10. The schematic organizing network of the human living system. The large hubs collecting many connections and some connections are concentrated in the intermediate places (acupoints).

exchanges, the meridian network is probably tightly connected to the mesenchymal tissues in all over the body. However, the meridians as independent structures are not observable even by the most developed autopsy investigations. There are two reasons for this. The first is that the information exchange for homeostasis is valid only in living state. The second reason is more crucial than the first one. According to our hypothesis the meridians are information exchange lines, so they are part of the informational networks. It means that between two points (acupoints) they are not necessarily a hard connection, but the information is exchanged by the multiple connections between the points, Figure 11. The picture is similar to the traffic situation in a town. The two points could virtually be linked by a straight line (bee-line), but this line is not a real direct connection between the points. However, many routes exist, even in case we are forced to detour. The two chosen points are connected without a straight line connection between them.

The ground substance is not only a "meeting volume" of the signals but also a place for the action of interference. The links for these from the body surface are probably the acupuncture points, which connect the internal balance with the environment too. In this line, it is trivial that there is a possibility to step-in to the regulation process of homeostasis.

There are three possibilities of the effects, [34]:

1) The ground substance over-regulates. In this case, the decrease of the regulator-signal is desired;

2) The ground substance under-regulates. Toning is applied to increase the signal;
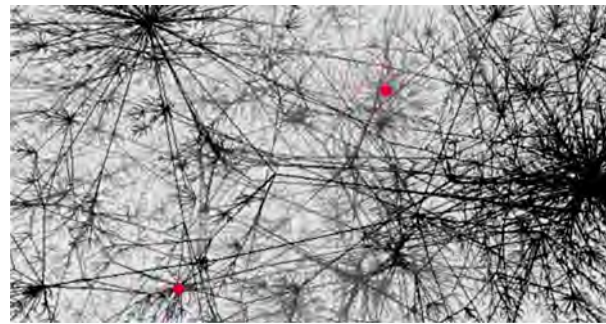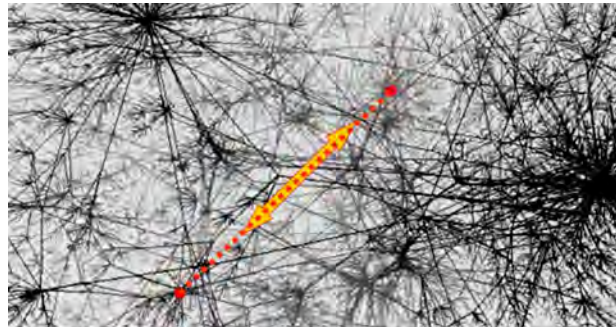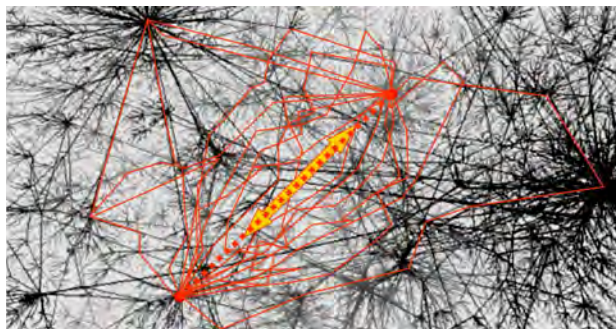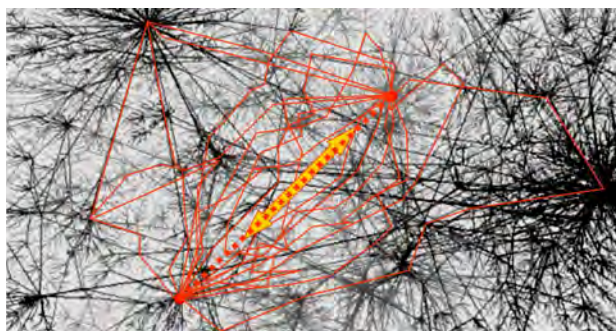
Figure 11. The forming of meridians as an information exchange virtual channel. (a) Two acupoints denoted by dots (chosen from the same meridians according to TCM); (b) The expected line of meridian according to TCM; (c) Multiple ways of information exchange connecting the two chosen points; (d) Due to the extremely large number of the possible ways for information exchange, the meridian virtually builds up. Due to the almost homogenous continue of the info-channels, the picture is very similar to the dipole forming an electric field between two opposite electric charges.

3) The deviation of the signal is too large. The error-noise is not $1/f$ pink noise. In this case, the homeostatic balance must be reconstructed by multiple acupuncture points.

5. Conclusion

We used the complexity of biosystems to study the acupuncture and meridian transports. We showed that physiology is well controlled by a complete interacting network or various negative feedback signals and processes, described by opposite interfering effects which are characterized in Traditional Chinese Medicine (TCM) by Yin-Yang (Y-Y) pairs. These regulatory pairs have a meaning in modern biology through the regulatory signals, transports, and interactions, and have a decisional role in the homeostasis of the complex system. The mean of fluctuations is used as a basis carrying a time-fractal fluctuation (called pink-noise or $1/f$ noise) of it. All signals in homeostasis have equal MSE entropy (S_E = 1.8). The various controlling opposite signals (Y-Y) have different time-scales and compose the pink-noise. The processes with smaller time-scale degrade by aging but pink-noise ensure that the deviations of the signals of the healthy homeostatic system remain constant by aging. The meridians are connected to the general material and information transport systems of the body completed as a meridian network by various coupling points. The coupling points which are near the skin-surface are called acupunctural points. These could be perturbed by actuating stimulus. We described the meridian system designated by the surface acupoints explaining why no structural appearance could be shown on these channels.

Acknowledgements

Conflicts of Interest

The authors declare that there is no conflict of interest.

References

[1] Langevin, H.M. and Wayne, P.M. (2018) What Is the Point? The Problem with Acupuncture Research That No One Wants to Talk About. *The Journal of Alternative and Complementary Medicine*, **24**, 200-207.
https://doi.org/10.1089/acm.2017.0366

[2] Godlee, F. (2018) Acupuncture: Theatrical Placebo or Caring Approach to Pain? *BM*, **360**, 1076.

[3] von Bertalanffy, L. (1934) Untersuchungen über die Gesetzlichkeit des Wachstums. I. Allgemeine Grundlagen der Theorie; mathematische und physiologische Gesetzlichkeiten des Wachstums bei Wassertieren. *Arch. Entwicklungsmech*, **131**, 613-652.

[4] Weckowicz, T.E. and von Bertalanffy, L. (1982) A Pioneer of General Systems

Theory, University of Alberta Center for Systems Research; Working Paper, 89-2.

[5] Richman, J.S. and Moorman, J.R. (2000) Physiological Time-Series Analysis Using Approximate Entropy and Sample Entropy. *American Journal of Physiology: Heart and Circulatory Physiology*, **278**, 2039-2049.
https://doi.org/10.1152/ajpheart.2000.278.6.H2039

[6] Costa, M., Goldberger, A.L. and Peng, C.K. (2005) Multiscale Entropy Analysis of Biological Signals. *Physical Review*, **71**, 021906.

[7] Pincus, S.M. and Goldberger, A.L. (1994) Physiological Time-Series Analysis: What Does Regularity Quantify? *American Journal of Physiology: Heart and Circulatory Physiology*, **266**, H1643-H1656. https://doi.org/10.1152/ajpheart.1994.266.4.H1643

[8] Chatfield, C. (1989) The Analysis of Time Series—An Introduction. 4th Edition, Chapman and Hall, London, 94-95.

[9] Costa, M., Goldberger, A.L. and Peng, C.-K. (2002) Multiscale Entropy to Distinguish Physiologic and Synthetic RR Time Series. *Computers in Cardiology*, **29**, 137-140. https://doi.org/10.1109/CIC.2002.1166726

[10] Szendro, P., Vincze, G. and Szasz, A. (2001) Pink Noise Behaviour of the Biosystems. *European Biophysics Journal*, **30**, 227-231.
https://doi.org/10.1007/s002490100143

[11] Szendro, P., Vincze, G. and Szasz, A. (2001) Bio-Response to White Noise Excitation. *Electro- and Magnetobiology*, **20**, 215-229.
https://doi.org/10.1081/JBC-100104145

[12] Hegyi, G., Vincze, G. and Szasz, A. (2012) On the Dynamic Equilibrium in Homeostasis. *Open Journal of Biophysics*, **2**, 64-71.
https://doi.org/10.4236/ojbiphy.2012.23009

[13] Sharma, K.K., Joshi. S.D and Sharma, S. (2013) Advances in Shannon Sampling Theory. *Defence Science Journal*, **63**, 41-45. https://doi.org/10.14429/dsj.63.3762

[14] Carter, T. (2014) An Introduction to Information Theory and Entropy. CSU Stanislaus Complex Systems Summer School, Santa Fe.

[15] Wheatley, D.N. (2003) Diffusion, Perfusion and the Exclusion Principles in the Structural and Functional Organization of the Living Cell: Reappraisal of the Properties of the "Ground Substance". *Journal of Experimental Biology*, **206**, 1955-1961.
https://doi.org/10.1242/jeb.00238

[16] Shingleton, A. (2010) Allometry: The Study of Biological Scaling. *Nature Education Knowledge*, **3**, 2.

[17] Szasz, O., Szigeti, Gy.P., Szasz, A. and Benyo, Z. (2018) Role of Electrical Forces in Angiogenesis. *Open Journal of Biophysics*, **8**, 49-67.
https://doi.org/10.4236/ojbiphy.2018.82005

[18] Szasz, O., Szigeti, Gy.P. and Szasz, A. (2017) On the Self-Similarity in Biologyical Processes. *Open Journal of Biophysics*, **7**, 183-196.
https://doi.org/10.4236/ojbiphy.2017.74014

[19] Oppenheim, A.V. and Verghese, G.C. (2015) Signals, Systems & Inference. *Power Spectral Density*, **10**, 183-195.

[20] Dunn, P.F. (2015) Measurement and Data Analysis for Engineering and Science. McGraw-Hill, New York.

[21] Bak, P., Tang, C. and Wiesenfeld, K. (1987) Self-Organized Criticality: An Explanation of $1/f$ Noise. *Physical Review Letters*, **59**, 381-384.
https://doi.org/10.1103/PhysRevLett.59.381

[22] Steliga, K. and Szynal, D. (2010) On Markov-Type Inequalities. *International Jour-*

nal of Pure and Applied Mathematics, **58**, 137-152.

[23] Isaacson, W. (2007) Einstein. His Life and Universe. Simon & Schuster Sydney.

[24] Lewin, R. (1999) Complexity—Life at the Edge of Chaos. The University of Chicago Press.

[25] Martin, W.F. (2011) Early Evolution without a Tree of Life. *Biology Direct*, **6**, 36-60. https://doi.org/10.1186/1745-6150-6-36

[26] West, B.J. (2006) Where Medicine Went Wrong: Rediscovering the Path to Complexity. World Scientific. https://doi.org/10.1142/6175

[27] Hoop, B. and Peng, C.K. (2000) Fluctuations and Fractal Noise. *The Journal of Membrane Biology*, **177**, 177-185. https://doi.org/10.1007/s002320010001

[28] West, B.J. and Deering, W. (1944) Fractal Physiology for Physicists: Levy Statistics. *Physics Reports*, **246**, 2-100.

[29] Maryan, M.I., Kikineshi, A.A. and Szasz, A. (2001) Self-Organizing Processes and Dissipative Structure Formation in the Non-Crystalline Materials. *Physics and Chemie Status Solidi*, **2**, 585-593.

[30] Martell, A.E. (1946) Entropy and the Second Law of Thermodynamics. *Journal of Chemical Education*, **23**, 166-170. https://doi.org/10.1021/ed023p166

[31] Gallos, L.K., Song, C.-M. and Makse, H.A. (2007) A Review of Fractality and Self-Similarity in Complex Networks. *Physica A*, **386**, 686-691. https://doi.org/10.1016/j.physa.2007.07.069

[32] Watts, D.J. and Strogatz, S.H. (1998) Collective Dynamics of "Small-World" Networks. *Nature*, **393**, 440-442. https://doi.org/10.1038/30918

[33] Gallos, L.K., Makse, H.A. and Sigman, M. (2012) A Small World of Weak Ties Provides Optimal Global Integration of Self-Similar Modules in Functional Brain Networks. *Proceedings of the National Academy of Sciences*, **109**, 2825-2830. https://doi.org/10.1073/pnas.1106612109

[34] Filshie, J. and White, A. (1998) Medical Acupuncture. A Western Scientific Approach. Churchil Livingstone.

Age-Dependent Comparative Study of 4 Hz and 8 Hz EMF Exposure on Heart Muscle Tissue Hydration of Rats

Lilia Narinyan, Sinerik Ayrapetyan*

UNESCO Chair—Life Sciences International Postgraduate Educational Center, Yerevan, Armenia
Email: *info@biophys.am, life@biophys.am

Abstract

Previously we have shown that 4 Hz and 8 Hz EMF exposures have depressing effect on the thermodynamic activity of water, which decreases peroxide formation. It has also been shown that 4 Hz EMF-treated physiological solution modulates the growth and development of microbes and heart muscle contractility, but 8 Hz EMF has pronounced inhibitory effect on bacterial growth and development. Therefore, in order to elucidate the possible mechanism of 4 Hz and 8 Hz EMF effects on heart muscle function, in the present work the effects of 4 Hz and 8 Hz EMF exposures on heart muscle tissue hydration, the sensitivity of 4 Hz and 8 Hz EMF-induced tissue hydration to 10^{-4} M ouabain (Na^+/K^+ pump inhibition) and 10^{-9} M ouabain (activation of intracellular signaling system) as well as the effects of 4 Hz and 8 Hz EMF exposures on the number of Na^+/K^+ pump units in the membrane of both young and old rats have been studied. The obtained data allow us to suggest that 8 Hz EMF exposure has more pronounced age-dependent modulation effect on tissue hydration of heart muscle than 4 Hz EMF and this effect is sensitive to Na^+/K^+ pump activity and intracellular signaling system.

Keywords

EMF, Tissue Hydration, Heart, Na^+/K^+ Pump, Na^+/Ca^{2+} Exchange

1. Introduction

In literature there are a lot of contradictory data on the biological effect of electromagnetic fields (EMF) on heart function [1] [2] [3] [4]. Our weak knowledge about cellular and molecular mechanisms of EMF effect on heart muscle is the reason of the variability of these data.

Since cell hydration (water content) is a fundamental cellular parameter con-

trolling metabolism, it is predictable that any factor able to change cell hydration can modulate cell metabolism and, conversely, cell metabolism changes will cause variation of cell hydration level [5] [6] [7] [8].

As physicochemical properties of water are sensitive to EMF [9] [10] [11] and cell membrane is highly permeable for water [12] [13], water molecules take the role of a primary messenger for EMF signal transduction from cell bathing medium into cell metabolism.

The Na^+/K^+ pump with a key role in cell volume regulation [14] [15] [16] [17] [18] is determining for the magnetic sensitivity of cell hydration. Our previous work has demonstrated that age-dependent decrease in magnetic sensitivity of heart muscle hydration is clearly expressed, when the Na^+/K^+ pump is in an inhibited state [19].

The Na^+/K^+-ATPase (working molecules of Na^+/K^+ pump) has three catalytic isoforms (a_1, a_2, a_3) in neuronal and muscle membranes [14]. These isoforms have different affinities to cardiac glycoside-ouabain and functional activities: a_1 and a_2 isoforms are involved in transportation of Na^+ and K^+ through membrane, while a_3 has only intracellular signaling function [14] [15]. Previously it has been shown that among these three families of receptors, a_3 isoform is a target for EMF effect [19] [20].

By our previous experiment, performed on snail hearts, it has been shown that 4 Hz EMF-treated physiological solution (PS) modulates the growth and development of microbes and heart muscle contractility [3] [21].

Our previous study on the effect of extremely low frequencies of EMF (ELF EMF) (<10 Hz) on physicochemical properties and hydrogen peroxide (H_2O_2) formation in water and water solution has elucidated that 4 Hz and 8 Hz frequencies depress water molecule dissociation and H_2O_2 formation in PS. It has also been shown that 8 Hz EMF has pronounced inhibitory effect on bacterial growth and development [21] [22] [23].

Thus, the aim of the present work was to perform a comparative study of 4 Hz and 8 Hz EMF exposure effect on heart muscle tissue hydration, 10^{-9} M and 10^{-4} M ouabain binding with cell membrane in young and old rats.

2. Materials and Methods

2.1. Animals

All procedures performed on animals were carried out following the protocols approved by Animal Care and Use Committee of Life Sciences International Postgraduate Educational Centre (LSIPEC, Yerevan, Armenia).

The experiments were performed on 45 young (6 weeks old) and 45 old (18 months old) Wistar albino rats. They were regularly examined, kept under control of the veterinarians in LSIPEC and reserved in a specific pathogen-free animal room under optimum conditions of 12 h light/dark cycles, at temperature of $22°C \pm 2°C$, with a relative humidity of 50% and were fed *ad libitum* on a standard lab chow and water.

2.2. Chemicals

Tyrode's PS containing (in mM) 137 NaCl, 5.4 KCl, 1.8 $CaCl_2$, 1.05 $MgCl_2$, 5 $C_6H_{12}O_6$, 11.9 $NaHCO_3$, and 0.42 NaH_2PO_4 and adjusted to pH 7.4 with NaOH was used. All chemicals were obtained from "Medisar" Industrial Chemical Importation Company (Yerevan, Armenia). The [^{3}H]-ouabain with specific activity (25.34 Ci/mM) (PerkinElmer, Massachusetts, USA) at 10^{-9} M and 10^{-4} M concentrations dissolved in PS were used for tissue incubation.

2.3. Source of EMF Radiation

The background of magnetic field in the area of experimental setup in the laboratory, due to the 60 Hz electricity system, was less than 0.001 mT. The holder of the exposure tube and the coil holder were placed on two neighboring tables to exclude the vibration during the exposure. The room temperature was 23°C. The exposure set up is presented in Figure 1.

The coil system has the diameter of 154 mm. The system consists of two Helmholtz rings with the distance of 77 mm that generate homogeneous magnetic field. Coils of Helmholtz are formed by two equal ring coils located coaxially and in a parallel way. The distance between ring coils is equal to their radius of 77 mm. The magnetic field created by these coils has high homogeneity. On distance of 0.25 R from the center of an axis, measured field strength differs from computed by formula only by 0.5% (H = 71.6 ωI/R). Here, the intensity of generated EMF is equal to 2.5 mT at 4 Hz and 8 Hz. The 4Hz and 8Hz exposures are generated by a special rectangular pulsing generator having output amplifier connected to the coil. The instrument used for measurement of magnetic field intensity was a Teslometer W1-8 (Armenian Radiophysical Institute, Yerevan, Armenia). This instrument measures magnetic fields in the range 10^{-3} T to 1.6 T (±5%). The magnetic induction converter was a crystal, type X511-1, 1.5 × 0.2 mm^2 and was fixed on non-magnetized material (PX13-1).

Animals were placed into the box and then in the setup and exposed by EMF for 15 min. After this procedure animals were sharply immobilized and decapitated. The same was done for sham group without EMF radiation.

2.4. Tissue Preparation

It is well known that anesthetics with different chemical and pharmacological
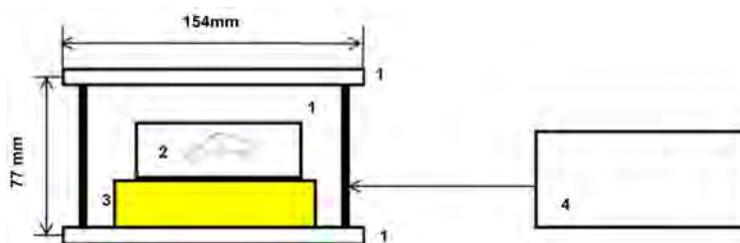
Figure 1. The exposure set up. 1—Helmholtz coil (D = 154 mm, H = 77 mm), 2—Plexiglas Box (134 mm × 105 mm × 55 mm), 3—Wooden table, 4—4 Hz and 8 Hz generator having output amplifier connected to coil.

profiles significantly affect metabolic processes, which play an important role in regulation of cell volume [24] [25]. Therefore, in the present experiments animals were sharply immobilized by freezing method (dipping their noses into liquid nitrogen for 3 - 5 sec) and decapitated. After such a procedure the full absence of somatic reflexes on extra stimuli was recorded.

Experiments were performed on 45 young and 45 old animals. From each group 15 young and 15 old animals were considered as sham animals, while 15 young and 15 old animals were exposed to 4 Hz or to 8 Hz EMF. Six pieces with 50 - 60 mg wet weight (w.w.) per piece were taken from each tested heart muscle. The obtained 90 samples from 15 sham animals were divided into 3 groups: 30 samples were incubated in PS, 30 samples—in PS containing 10^{-4} M [^{3}H]-ouabain and 30 samples—in PS containing 10^{-9} M [^{3}H]-ouabain. The same procedure has been performed on 15 animals exposed to 8 Hz and on 15 animals exposed to 4 Hz EMF. Thus, each column on the figures presents the mean value of the data from 30 samples.

2.5. Definition of Water Content of Heart Tissues

Water content of heart muscle tissues was determined by traditional "tissue drying" method [26]. After measuring the wet weight (w.w.) of heart muscle tissue samples it was dried in oven (Factory of Medical Equipment, Odessa, Ukraine) for 24 h at 105°C for determination of dry weight (d.w.). The quantity of water in 1 g of d.w. tissue was counted by the following equation: (w.w. – d.w./d.w). For investigation of water content variations and ouabain effects each animal group was divided into 3 subgroups: in the first (sham) subgroup there were animals without any radiation, in the second subgroup the animals were radiated with 8 Hz EMF and in the third subgroup the animals were radiated with 4 Hz EMF.

2.6. Counting of [^{3}H]-Ouabain Receptors in Membrane

Heart muscle tissue samples were incubated in 10 ml of 10^{-9} M or 10^{-4} M [^{3}H]-ouabain solutions for 30min. Then they were washed three times (10 min-5 min-5 min) in normal PS (ouabain-free) for removing [^{3}H]-ouabain from tissue. After determination of dry weights of samples, they were homogenized in 50 μl of 68% HNO_3 solution. Finally 2 ml of Bray's scintillation fluid was added and the radioactivity of samples was calculated as counted per minute (CPM)/mg of dry weight by Wallac 1450 liquid scintillation and luminescence counter (Wallac Oy, Turku, Finland).

2.7. Statistical Analysis

Microsoft Excel and Sigma-Plot (Version 8.02A, NY, USA) were used for data analyses. Significance in comparison with the sham group was calculated with Student's t-test with the following symbols (*$p < 0.05$; **$p < 0.01$; ***$p < 0.001$).

3. Results

In our previous works cell hydration has been suggested as a primary messenger through whi3ch the biological effects of EMF are realized [11] [17] [27] [28] [29].

As it can be seen in **Figure 2(A)**, **Figure 2(B)**, the level of heart muscle hydration was significantly increased upon the effects of 4 Hz (1.4%-in young; 1.8%-in old) and 8 Hz (5.7%-in young; 4%-in old) EMF exposures as compared to sham group.

The dysfunction of Na^+/K^+ pump, which is a common consequence of ageing, has a key role in metabolic regulation of cell hydration and intracellular Ca homeostasis ($[Ca^{2+}]_i$). The Na^+/K^+-pump, being a high metabolic energy (ATP) utilizing mechanism and working with high intensity in cardiomyocytes, has a great intracellular signaling role in controlling Ca^{2+} sorption properties by intracellular structure as well as in generation of endogenous H_2O in cytoplasm. Therefore, Na^+/K^+-pump could be considered not only as an ion transporting mechanism but also as a powerful intracellular signaling system controlling cell hydration and $[Ca^{2+}]_i$ in myocytes.

To evaluate the role of Na^+/K^+ pump in realization of biological effects of 4Hz and 8Hz EMF on heart muscle hydration, after EMF exposure the heart muscle samples of animals are incubated in 10^{-4} M ouabain solution, which has inhibitory effect on Na^+/K^+ pump activity [30].

As it can be seen in **Figure 3(A)**, **Figure 3(C)**, in sham groups heart muscle sample incubation in 10^{-4} M ouabain brings to tissue hydration (11%) in young animals and dehydration (2.1%) in old ones (sham groups). In experimental groups (after 4 Hz EMF radiation) sample incubation in 10^{-4} M ouabain containing PS leads to tissue hydration (5.4%) in old animals, while in young animals muscle
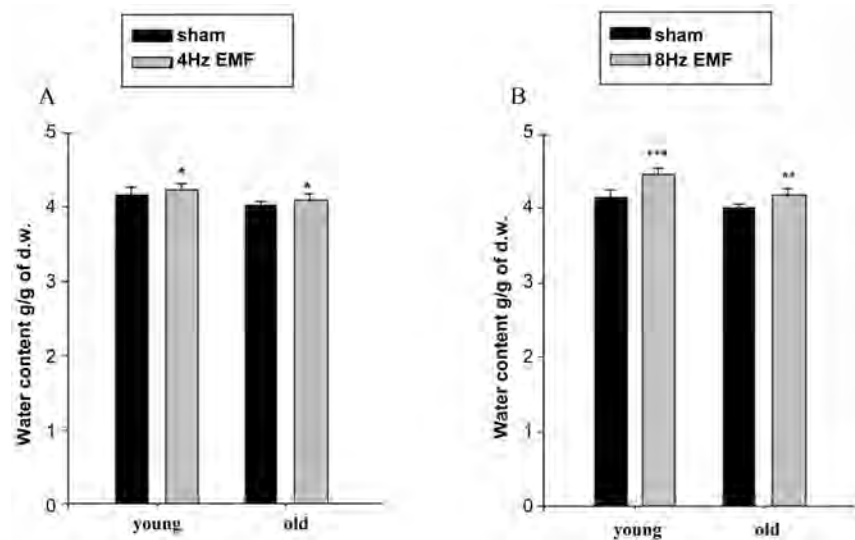
Figure 2. 4 Hz (A) and 8 Hz EMF (B) exposures on hydration of heart muscle tissues of young and old animals. Each bar on figure represents the mean ± SEM of 30 samples. The symbols (*), (**) and (***) indicate p < 0.05, p < 0.01 and p < 0.001, respectively.
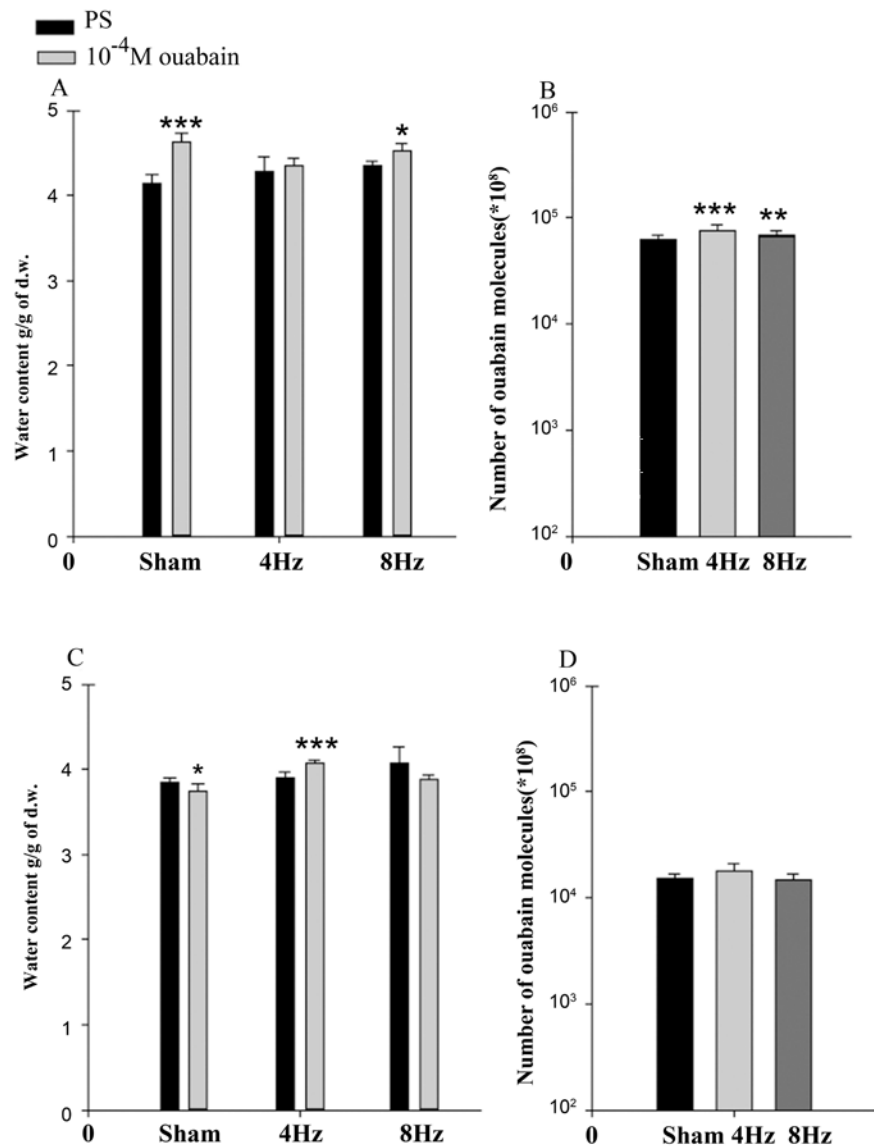
Figure 3. The changes of heart muscle tissue hydration after incubation in 10^{-4} M ouabain in sham, 4 Hz EMF and 8 Hz EMF-exposed young (A, B) and old (C, D) animals. Ordinates on A, C indicate the mean value of water content in heart muscle tissues. Ordinates on B, D are logarithmic and define the number of [^{3}H]-ouabain binding molecules with cell membrane in heart muscle tissues. Each bar represents the mean ± SEM of 30 samples. The symbols (*), (**) and (***) indicate $p < 0.05$, $p < 0.01$ and $p < 0.001$, respectively.

hydration is not significantly changed compared with muscle hydration incubated in ouabain-free PS. After 8 Hz EMF radiation 10^{-4} M ouabain leads to muscle hydration (4.6%) in young animals and dehydration (8%) in heart muscle tissues in old animals. The previous studies have revealed that cell swelling increases the number of ouabain binding sides in membrane [6], while the affinity of ouabain receptors is depressed as a result of [Ca^{2+}]$_i$ increase [20] [31].

As shown in **Figure 3(B)**, **Figure 3(D)** after 4 Hz EMF exposure at 10^{-4} M ouabain concentration the number of [^{3}H]-ouabain binding receptors in heart

muscle are slightly increased in young and old animals compared to sham groups of rats. After 8 Hz EMF exposure at 10^{-4} M ouabain concentration, the number of [³H]-ouabain binding receptors with cell membrane in heart muscle tissues is significantly increased in young and is not changed in old rats.

Previously it has been shown that 10^{-9} M ouabain brings to stimulation of cAMP and activation of Na^+/Ca^{2+} exchange in reverse mode (R Na^+/Ca^{2+} exchange) without inactivation of Na^+/K^+ pump activity [32]. Therefore, in order to find out the role of Na^+/Ca^{2+} exchange in EMF-induced modulation of heart muscle hydration, in the next series of experiments the above presented protocol of experiments with 10^{-4} M ouabain is repeated with 10^{-9} M ouabain.

The data presented in Figure 4 (A), Figure 4(C) indicate that 10^{-9} M ouabain has hydration effect on heart muscle tissues in both young (3.7%) and old (5.4%)
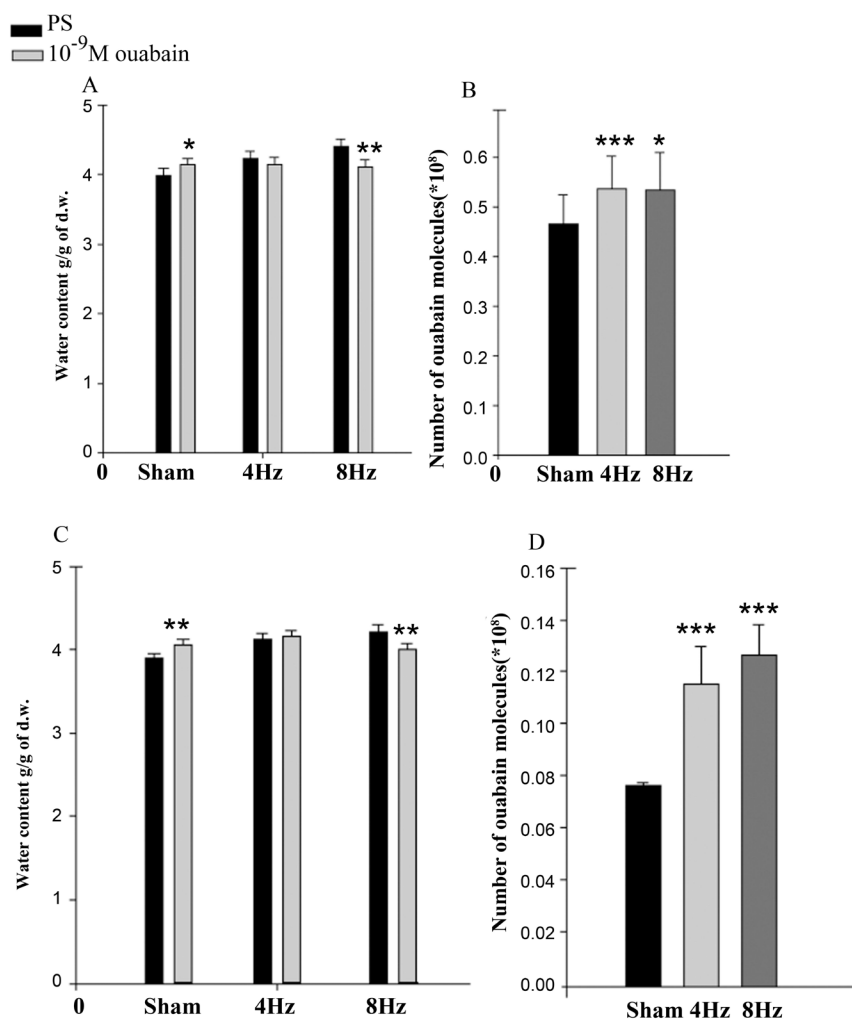
Figure 4. The changes of heart muscle tissue hydration after incubation in 10^{-9} M ouabain in sham, 4 Hz EMF and 8 Hz EMF-exposed young (A, B) and old (C, D) animals. Ordinates on A, C indicate the mean value of water content in tissues. Ordinates on B, D are logarithmic and define the number of [³H]-ouabain binding molecules in tissues. Each bar represents the mean ± SEM of 30 samples. The symbols (*), (**) and (***) indicate $p < 0.05$, $p < 0.01$ and $p < 0.001$, respectively.

animals. As it can be seen in Figure 4(A), Figure 4(C), the 10^{-9} M ouabain has dehydration effect on heart muscle tissues of 4 Hz EMF-exposed young (2.4%) animals compared to sham group of animals and has no effect in old animals. After 8 Hz EMF exposure 10^{-9} M ouabain has dehydration effect (7%) on heart muscle tissues of young animals as compared to sham group of animals and has no effect in old ones. The dehydration effect in 4 Hz and 8 Hz EMF-exposed young animals are accompanied by the increase (15.2%) of ouabain binding with cell membrane in heart muscle tissues (Figure 4(B)). In old animals the exposure with 4 Hz and 8 Hz EMF are also accompanied by the increase of ouabain binding with membrane (37.5% and 50%, respectively) (Figure 4(D)).

4. Discussion

It is known that the permeability of cell membrane for water molecules is much higher than the permeability of cell membrane for ions [12] [13] and that intracellular osmotic pressure exceeds the extracellular one [33]. Therefore, to keep cell volume in a steady state, the osmotic water uptake must be balanced by water efflux from the cell.

Our study performed on intracellular dialyzed squid axons and intact neurons of snails has shown that water fluxes through membrane have a crucial role in regulation of cell membrane permeability for Na^+, Ca^{2+}, K^+: water influx and efflux through cell membrane have activation and inactivation effects on inward ionic currents on Na^+ and Ca^{2+} current, and opposite effect on outward K^+ current, respectively [8] [34] [35] [36].

The Na^+/K^+ pump is a fundamental metabolic mechanism in cell membrane which controls cell functional activity. The activation of Na^+/K^+ pump leads to generation of water efflux from the cells by 1) push out of $3Na^+$ and uptake of $2K^+$ and 2) release of H_2O in cytoplasm (42 H_2O for one molecule glucose oxidation) as a result of activation of intracellular oxidative phosphorylation [37]. Previously we have shown that Na^+/K^+ pump-dependent regulation of cell volume is a powerful metabolic mechanism through which both the auto-regulation of Na^+/K^+-pump and the regulation of membrane chemo sensitivity [7] and excitability [8] are realized by changing surface-dependent number of functionally active proteins in membrane.

The data presented in Figure 2(A) and Figure 2(B) indicate that heart muscle tissue hydration in both group of animals is sensitive to 4 Hz and 8 Hz EMF. By our previous study it has been shown that static and pulsing magnetic fields activate cGMP-dependent Na^+/Ca^{2+} exchange in forward mode (F Na^+/Ca^{2+}) pushing out Ca^{2+} from the cell [16]. As Na^+/Ca^{2+} exchange functions in stoichiometry of $3Na^+$:$1Ca^{2+}$ [38] it was predicted that F Na^+/Ca^{2+} exchange should have hydration effect on cells. This effect was presented in Figure 2(A), Figure 2(B). As it can be seen in Figure 2(A), Figure 2(B) the 8 Hz EMF leads to more pronounced effect on hydration in both group of animals compared to 4 Hz EMF.

The obtained data (Figure 3(A), Figure 3(C)) on the effects of 10^{-4} M ouabain (Na$^+$/K$^+$ pump is in inactive state) on heart muscle tissue hydration indicate that in sham animals 10^{-4} M ouabain-induced hydration has age-dependent (metabolic-dependent) character (in young animals it brings to hydration, while in old animals it has dehydration effect). Previously it has been shown that Na$^+$/K$^+$ pump inactivation-induced hydration is due to both Na$^+$ uptake and cAMP-dependent R Na$^+$/Ca^{2+} exchange-induced activation of intracellular oxidative processes leading to the release of endogenous water molecules, and the hydration of heart muscle tissue in young sham animals (Figure 3(A)) is considered as a result of these processes.

It is known that the dysfunction of Na$^+$/K$^+$ pump, which is accompanied by the increase of intracellular Ca^{2+} concentration ($[Ca^{2+}]_i$), is a common consequence of any cell pathology (including ageing). The dehydration of heart muscle in old sham rats (Figure 3(C)) is considered as a result of initial high level of $[Ca^{2+}]_i$. The increase of $[Ca^{2+}]_i$, which is accompanied by Na$^+$/K$^+$ pump inactivation, is considered as a result of intracellular Na$^+$ concentration ($[Na^+]_i$) increase which stimulates Ca^{2+} uptake through R Na$^+$/Ca^{2+} exchange.

In heart muscle tissues of 4 Hz and 8 Hz EMF-exposed young animals 10^{-4} M ouabain has dehydration effect on tissues compared with sham group (the bar on 10^{-4} M ouabain) and is accompanied by the increase in the number of ouabain binding molecules with membrane. These results can be interpreted by the activation of cGMP-dependent F Na$^+$/Ca^{2+} exchange pushing out Ca^{2+} from the cell and reactivating electrogenic Na$^+$/K$^+$ pump, which leads to the increase of ouabain receptors affinity [20] [39].

In case of 4 Hz EMF and 8 Hz EMF-exposed old animals, the 10^{-4} M ouabain leads to the increase of heart muscle tissue hydration without changes in the number of ouabain binding molecules with membrane (Figure 3(C), Figure 3(D)). It can be explained by high $[Ca^{2+}]_i$ in old animals, which is more increased by applying 10^{-4} M ouabain leading to activation of "Ca^{2+}-calmodulin-NO syntase-cGMP" metabolic chain, which stimulates F Na$^+$/Ca^{2+} exchange having hydration effect on cells.

By our previous experiment performed on snail neurons it has been shown that $<10^{-9}$ M ouabain has activation effect on ^{22}Na$^+$ efflux in exchange to Ca^{2+} uptake (R Na$^+$/Ca^{2+} exchange), which is accompanied by elevation of intracellular cAMP, without changing Na$^+$/K$^+$-pump activity [32].

The fact that the nM ouabain can elevate the intracellular cAMP is demonstrated in different tissues including dog renal cortex, gold fish intestinal mucosa, mouse pancreatic islets, murine epithelioid and fibroblastic cell lines, rat brain, rat renal collecting tubule cells in culture and astrocytes [40].

The obtained data (Figure 4(A)) of the effects of 10^{-9} M ouabain (Na$^+$/K$^+$ pump is in active state) on heart muscle tissue hydration indicate that in sham group of young animals 10^{-9} M ouabain-induced hydration is due to stimulation of R Na$^+$/Ca^{2+} exchange as a result of cAMP-dependent Ca^{2+} pump activation in

the membrane of endoplasmatic reticulum, which brings to activation of mitochondrial function and release of endogenous H_2O.

As in heart muscles of old animals $[Ca^{2+}]_i$ is high, phospholipase activity in membrane is increased and 10^{-9} M ouabain through activation of inositol 1,4,5-trisphosphate receptors brings to activation of $[Ca^{2+}]_i$-Calmodulin-NO-cGMP cascade leading to stimulation of Ca^{2+} efflux and leads to hydration (**Figure 4(C)**).

The data that 4 Hz EMF causes no hydration changes in young and in old rats compared with sham group (the bar on 10^{-9} M ouabain), while 8 Hz EMF exposure (**Figure 4(A)**, **Figure 4(C)**) brings to dehydration effect and both cases are accompanied by the increase of ouabain binding (**Figure 4(B)**, **Figure 4(D)**) clearly indicate that membrane receptors affinity to ouabain is increased. This effect can be explained by the activation of cGMP-dependent F Na^+/Ca^{2+} exchange leading to decrease of $[Ca^{2+}]_i$ [41].

Thus, from the obtained data it can be concluded that heart muscle tissue hydration of sham animals is sensitive to 4 Hz and 8 Hz EMF exposure and this sensitivity has metabolic and age-dependent character. The cGMP/cAMP-dependent Na^+/Ca^{2+} exchange controlling intracellular oxidative phosphorylation processes and endogenous release of water molecules in cytoplasm has a major role in regulation of cell hydration and $[Ca^{2+}]_i$. Thus, on the basis of previous and present data we suggest that 8 Hz EMF has more pronounced effect on heart muscle tissue hydration than 4 Hz EMF and this effect is realized through activation of cGMP-dependent F Na^+/Ca^{2+} exchange.

Conflicts of Interest

The authors declare no conflicts of interest regarding the publication of this paper.

References

[1] Elmas, O. (2016) Effects of Electromagnetic Field Exposure on the Heart: A Systematic Review. *Toxicology and Industrial Health*, **32**, 76-82. https://doi.org/10.1177/0748233713498444

[2] Johansen, C. (2004) Electromagnetic Field and Health Effects—Epidemiologic Studies of Cancer, Diseases of the Central Nervous System, and Arrhythmia-Related Heart Diseases. *Scandinavian Journal of Work, Environment & Health*, **30**, 1-30.

[3] Ayrapetyan, G., Papanyan, A., Hayrapetyan, H. and Ayrapetyan, S. (2005) Metabolic Pathway of Magnetized Fluid-Induced Relaxation Effects on Heart Muscle. *Bioelectromagnetics*, **26**, 624-630. https://doi.org/10.1002/bem.20145

[4] Zhou, L., Wan, B., Liu, X., *et al.* (2016) The Effects of a 50-Hz Magnetic Field on the Cardiovascular System in Rats. *Journal of Radiation Research*, **57**, 627-636. https://doi.org/10.1093/jrr/rrw090

[5] Parsegian, V.A., Rand, R.P. and Rau, D.C. (2000) Osmotic Stress, Crowding, Preferential Hydration, and 3 Binding: A Comparison of Perspectives. *Proceedings of the National Academy of Sciences of the United States of America*, **97**, 3987-3992. https://doi.org/10.1073/pnas.97.8.3987

[6] Ayrapetyan, S.N., Suleymanyan, M.A., Saghyan, A.A. and Dadalyan, S.S. (1984) Autoregulation of the Electrogenic Sodium Pump. *Cellular and Molecular Neurobiology*, **4**, 367-384. https://doi.org/10.1007/BF00733598

[7] Ayrapetyan, S.N., Arvanov, V.L., Maginyan, S.N. and Azatyan, K.V. (1985) Further Study of the Correlation between Na-Pump Activity and Membrane Chemosensitivity. *Cellular and Molecular Neurobiology*, **5**, 231-243. https://doi.org/10.1007/BF00711009

[8] Ayrapetyan, S.N., Rychkov, G.Y. and Suleymanyan, M.A. (1988) Effects of Water Flow on Transmembrane Ionic Currents in Neurons of *Helix pomatia* and in Squid Giant Axon. *Comparative Biochemistry and Physiology Part A: Physiology*, **89**, 179-186. https://doi.org/10.1016/0300-9629(88)91076-6

[9] Klassen, V.I. (1982) Magnetized Water Systems. Chemistry Press, Moscow, 296. (In Russian)

[10] Lednev, V.V. (1991) Possible Mechanism for the Influence of Weak Magnetic Field on Biological Systems. *Bioelectromagnetics*, **12**, 71-75. https://doi.org/10.1002/bem.2250120202

[11] Ayrapetyan, S.N., Grigorian, K.V., Avanesyan, A.S. and Stamboltsian, K.V. (1994) Magnetic Fields alter Electrical Properties of Solutions and Their Physiological Effects. *Bioelectromagnetics*, **15**, 133-142. https://doi.org/10.1002/bem.2250150205

[12] Borgnia, M., Nielsen, S., Engel, A. and Aqre, P. (1999) Cellular and Molecular Biology of the Aquaporin Water Channels. *Annual Review of Biochemistry*, **68**, 425-458. https://doi.org/10.1146/annurev.biochem.68.1.425

[13] Hoffmann, E.K., Sorensen, B.H., Sauter, D.P. and Lambert, I.H. (2015) Role of Volume-Regulated and Calcium-Activated Anion Channels in Cell Volume Homeostasis, Cancer and Drug Resistance. *Channels* (*Austin*), **9**, 380-396. https://doi.org/10.1080/19336950.2015.1089007

[14] Blaustein, M.P. and Lederer, W.J. (1999) Na^+/Ca^{2+} Exchange. Its Physiological Implications. *Physiological Reviews*, **79**, 763-854. https://doi.org/10.1152/physrev.1999.79.3.763

[15] Xie, Z. and Askari, A. (2002) Na^+/K^+-ATPase as a Signal Transducer. *European Journal of Biochemistry*, **269**, 2434-2439. https://doi.org/10.1046/j.1432-1033.2002.02910.x

[16] Ayrapetyan, S.N., Baghdasaryan, N., Mikayelyan, Y., *et al.* (2015) Cell Hydration as a Marker for Non-Ionizing Radiation. In: Markov, M., Ed., *Electromagnetic Fields in Biology and Medicine*, CRC Press, Boca Raton, 193-215.

[17] Ayrapetyan, S.N. (2015) The Role of Cell Hydration in Realization of Biological Effects of Non-Ionizing Radiation (NIR). *Electromagnetic Biology and Medicine*, **34**, 197-210. https://doi.org/10.3109/15368378.2015.1076443

[18] Ayrapetyan, S., Heqimyan, A. and Nikoghosyan, A. (2017) The Comparative Study of 8Hz EMF Effect on Tissue Hydration in Brain Cortex and Subcortex of Rats. *Advances in Life Sciences*, **7**, 31-38.

[19] Narinyan, L., Ayrapetyan, G. and Ayrapetyan, S. (2012) Age-Dependent Magnetosensitivity of Heart Muscle Hydration. *Bioelectromagnetics*, **33**, 452-458. https://doi.org/10.1002/bem.21704

[20] Narinyan, L., Ayrapetyan, G. and Ayrapetyan, S. (2013) Age-Dependent Magnetosensitivity of Heart Muscle Ouabain Receptors. *Bioelectromagnetics*, **34**, 312-322. https://doi.org/10.1002/bem.21769

[21] Martirosyan, V., Baghdasaryan, N. and Ayrapetyan, S. (2013) Bidirectional Fre-

quency-Dependent Effect of Extremely Low-Frequency Electromagnetic Field on *E. coli* K-12. *Electromagnetic Biology and Medicine*, **32**, 291-300. https://doi.org/10.3109/15368378.2012.712587

[22] Baghdasaryan, N., Mikayelyan, Y., Barseghyan, S., Dadasyan, E. and Ayrapetyan, S. (2012) The Modulation Impact of Illumination and Background Radiation on 8 Hz-Induced Infrasound Effect on Physicochemical Properties of Physiological Solution. *Electromagnetic Biology and Medicine*, **31**, 310-319. https://doi.org/10.3109/15368378.2011.638029

[23] Baghdasaryan, N., Mikayelyan, Y., Nikoghosyan, A. and Ayrapetyan, S. (2013) The Impact of Background Radiation, Illumination and Temperature on EMF-Induced Changes of Aqua Medium Properties. *Electromagnetic Biology and Medicine*, **32**, 390-400. https://doi.org/10.3109/15368378.2012.735206

[24] Krnjevic, K. (1992) Cellular and Synaptic Actions of General Anaesthetics. *General Pharmacology*, **23**, 965-975. https://doi.org/10.1016/0306-3623(92)90274-N

[25] Heqimyan, A., Deghoyan, A. and Ayrapetyan, S. (2011) Ketamine-Induced Cell Dehydration as a Mechanism of Its Analgesic and Anesthetic Effects. *Journal of International Dental and Medical Research*, **4**, 42-49.

[26] Adrian, R. (1956) The Effect of Internal and External K Concentration on the Membrane Potential of Frog Muscle. *The Journal of Physiology*, **133**, 631-658. https://doi.org/10.1113/jphysiol.1956.sp005615

[27] Danielyan, A.A. and Ayrapetyan, S.N. (1999) Changes of Hydration of Rats' Tissues after *in Vivo* Exposure to 0.2 Tesla Steady Magnetic Field. *Bioelectromagnetics*, **20**, 123-128. https://doi.org/10.1002/(SICI)1521-186X(1999)20:2<123::AID-BEM7>3.0.CO;2-A

[28] Danielyan, A.A., Mirakyan, M.M., Grigoryan, G.Y. and Ayrapetian, S.N. (1999) The Static Magnetic Field on Ouabain H3 Binding by Cancer Tissue. *Physiological Chemistry and Physics and Medical NMR*, **31**, 139-144.

[29] Ayrapetyan, S.N. (2006) Cell Aqua Medium as a Primary Target for the Effect of Electromagnetic Fields. In: Ayrapetyan, S. and Markov, M., Eds., *Bioelectromagnetics: Current Concepts*, NATO Science Series, Springer Press, Dordrecht, 31-63.

[30] Skou, J. (1957) The Influence of Some Cations on an Adenosine Triphosphatase from Peripheral Nerves. *Comparative Biochemistry and Physiology*, **64**, 571-575.

[31] Deghoyan, A., Nikoghosyan, A., Heqimyan, A. and Ayrapetyan, S.N. (2014) Age-Dependent Effect of Static Magnetic Field on Brain Tissue Hydration. *Electromagnetic Biology and Medicine*, **33**, 58-67.

[32] Saghian, A., Ayrapetyan, S. and Carpenter, D. (1996) Low Concentrations of Ouabain Stimulate Na:Ca Exchange in Neurons. *Cellular and Molecular Neurobiology*, **16**, 180-185. https://doi.org/10.1007/BF02150229

[33] Evans, D. (2009) Osmotic and Ionic Regulation: Cells and Animals. CRC Press, New York.

[34] Kojima, M., Ayrapetyan, S. and Koketsu, K. (1984) On the Membrane Potential Independent Mechanism of Sodium Pump-Induced Inhibition of Spontaneous Electrical Activity of Japanese Land Snail Neurons. *Comparative Biochemistry and Physiology Part A*, **77**, 577-583. https://doi.org/10.1016/0300-9629(84)90232-9

[35] Ayrapetyan, S. and Rychkov, G. (1985) The Presence of Reserve Ion Channels in Membranes of Giant Snail Neurons and Giant Squid Axons. *DAN SSSR*, **285**, 1464-1467. (In Russian)

[36] Suleymanian, M., Ayrapetyan, V., Arakelyan, V. and Ayrapetyan, S. (1993) The Ef-

fect of Osmotic Gradient on the Outward Potassium Current in Dialyzed Neurons of Helix Pomatia. *Cellular and Molecular Neurobiology*, **13**, 183-190. https://doi.org/10.1007/BF00735374

[37] Lehninger, A.L. (1970) Mitochondria and Calcium Ion Transport. *Biochemical Journal*, **119**, 129-138. https://doi.org/10.1042/bj1190129

[38] Baker, P., Blaustein, M., Hodgkin, A. and Steinhardt, S. (1969) The Influence of Ca on Na Efflux in Squid Axons. *The Journal of Physiology*, **200**, 431-458. https://doi.org/10.1113/jphysiol.1969.sp008702

[39] Nikoghosyan, A., Heqimyan, A. and Ayrapetyan, S.N. (2016) Primary Mechanism Responsible for Age-Dependent Neuronal Dehydration. *International Journal of Basic and Applied Sciences*, **5**, 5-14. https://doi.org/10.14419/ijbas.v5i1.5388

[40] Siegel, G., Agranoff, B., Albers, R., Fisher, R. and Uhler, M. (1999) Basic Neurochemistry: Molecular, Cellular and Medical Aspects. 6th Edition, Lippincott-Raven, Philadelphia.

[41] Heqimyan, A., Narinyan, L., Nikoghosyan, A. and Ayrapetyan, S. (2015) Age-Dependent Magnetic Sensitivity of Brain and Heart Muscles. In: Markov, M., Ed., *Electromagnetic Fields in Biology and Medicine*, CRC Press, Boca Raton, 217-230. https://doi.org/10.1201/b18148-15
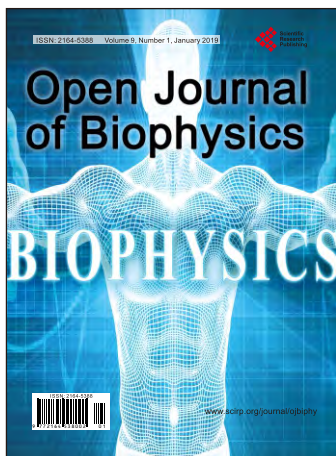
Call for Papers

Open Journal of Biophysics

Open Journal of Biophysics (OJBIPHY) is an international journal dedicated to the latest advancement of biophysics. The goal of this journal is to provide a platform for scientists and academicians all over the world to promote, share, and discuss various new issues and developments in different areas of biophysics.

Subject Coverage

All manuscripts must be prepared in English, and are subject to a rigorous and fair peer-review process. Accepted papers will immediately appear online followed by printed hard copy. The journal publishes original papers including but not limited to the following fields:

- Bioelectromagnetics
- Bioenergetics
- Bioinformatics and Computational Biophysics
- Biological Imaging
- Biomedical Imaging and Bioengineering
- Biophysics of Disease
- Biophysics of Photosynthesis
- Cardiovascular Biophysics
- Cell Biophysics
- Medical Biophysics
- Membrane Biophysics
- Molecular Biophysics and Structural Biology
- Physical Methods
- Physiology and Biophysics of the Inner Ear
- Proteins and Nucleic Acids Biophysics
- Radiobiology
- Receptors and Ionic Channels Biophysics
- Sensory Biophysics and Neurophysiology
- Systems Biophysics
- Theoretical and Mathematical Biophysics

We are also interested in: 1) Short Reports—2-5 page papers where an author can either present an idea with theoretical background but has not yet completed the research needed for a complete paper or preliminary data; 2) Book Reviews—Comments and critiques.

Notes for Intending Authors

Submitted papers should not have been previously published nor be currently under consideration for publication elsewhere. Paper submission will be handled electronically through the website. All papers are refereed through a peer review process. For more details about the submissions, please access the website.

Website and E-Mail

http://www.scirp.org/journal/ojbiphy   E-mail: ojbiphy@scirp.org

What is SCIRP?

Scientific Research Publishing (SCIRP) is one of the largest Open Access journal publishers. It is currently publishing more than 200 open access, online, peer-reviewed journals covering a wide range of academic disciplines. SCIRP serves the worldwide academic communities and contributes to the progress and application of science with its publication.

What is Open Access?

All original research papers published by SCIRP are made freely and permanently accessible online immediately upon publication. To be able to provide open access journals, SCIRP defrays operation costs from authors and subscription charges only for its printed version. Open access publishing allows an immediate, worldwide, barrier-free, open access to the full text of research papers, which is in the best interests of the scientific community.

- High visibility for maximum global exposure with open access publishing model
- Rigorous peer review of research papers
- Prompt faster publication with less cost
- Guaranteed targeted, multidisciplinary audience

Scientific Research Publishing

Website: http://www.scirp.org
Subscription: sub@scirp.org
Advertisement: service@scirp.org